Université de Neuchâtel
Institut de Microtechnique

Study of the coherent coupling of fiber lasers by use of an intracavity phase grating

Thèse

Présentée à la Faculté des sciences
pour obtenir le grade de docteur ès sciences

par

Jacques Morel

Neuchâtel, mai 1994

IMPRIMATUR POUR LA THÈSE

Study of the coherent coupling of fiber lasers by use of an intracavity phase grating

de Monsieur Jacques Morel

UNIVERSITÉ DE NEUCHÂTEL

FACULTÉ DES SCIENCES

La Faculté des sciences de l'Université de Neuchâtel
sur le rapport des membres du jury,

Messieurs R. Dändliker, F. Pellandini,
W. Lüthy (Berne) et R. Salathé (EPF-Lausanne)

autorise l'impression de la présente thèse.

Neuchâtel, le 9 juin 1994

Le doyen :

H.-H. Nägeli

To my Parents

To Mirella

Table of contents

Introduction

Since the first experiments carried out in 1964 [1], fiber lasers and amplifiers have encountered a tremendous success, mainly du to the wide range of potential applications in the domain of telecommunications, with the well known Erbium doped fiber amplifiers, but also in the domain of optical sources for sensors and for medicine. The improvement of the properties of the rare earth doped fibers opened the door to a large number of promising applications, such as the amplification at 1.3 μm for the second telecommunication window, or the fabrication of efficient high power lasers in the infrared, mainly for material processing and for roedical purposes. The main interest of active fibers arises from the high confinement of the optical light field in the waveguide, which results in very high optical intensities. This in turn allows to achieve very high gain even with moderate optical pumping. This property can be used to operate radiative transitions with low emission cross-sections and which cannot be used in bulk materials. This is the case, for example, for the red transition at 650 nm of Sm^{3+}:SiO_2. Another advantage of active fiber devices is the intrinsically "all-fiber" structure which can be easily implemented in any fiber sensor or fiber link by use of standard splicing techniques. In the scope of this thesis, we have focused our interest mainly on two distinct domains. First of all, a detailed study of the basic properties of rare earth doped fibers has been carried out in order to efficiently optimize and use these fibers. Several measurement setups and techniques have been implemented for the characterization of the spectroscopic properties of rare earth doped fibers, such as the absorption and fluorescence spectra (emission cross-sections), the fluorescence lifetime, and finally the gain properties. These topics will be discussed in Chapt. 1. A theoretical model for the gain of active fiber devices will be developed and discussed in Chapt. 2. The interactions between the active medium and the waveguide will be especially emphasized. In Chapt. 3 some of the applications of rare earth doped fibers for broadband superfluorescent sources and for lasers will be discussed. Finally, the coherent addition of fiber lasers will be extensively investigated in Chapt. 4. A new concept for the coherent addition, which involves an intracavity coupling of the individual emitters, will be theoretically analyzed and experimentally demonstrated. The coherent coupling of laser cavities is of interest for high power sources, as it allows to overcome the limit of the maximum optical power which can be supported in the fiber core before destructing the waveguide (thermal lensing). Another domain of interest are distributed sensors, since we have intrinsically a distributed structure of the individual cavities. This structure could be an interesting basis for a new family of distributed active fiber sensors by considering the dependence of the output characteristics (spectrum, power), as a function of the perturbation applied to anyone of the individual cavities.

1. Characterization of the fundamental properties of rare earth doped fibers

In this section, we characterize some of the basic properties of rare earth doped fibers, which are most relevant for the optimization of the fabrication processes, and which are also fundamental for the modeling of the properties of active fiber devices. Most of these characteristics do not rely independently on the specific properties of the passive waveguide which constitutes the fiber and the active medium but depend on how the guiding and the active medium interact. Consequently, these parameters are very difficult to measure separately. For that reason, we are usually interested in the characterization of the overall parameters, which include the effect of both the waveguide and the active medium. A typical example is given by the measurement of the spectral attenuaöon of the dopant at the pump wavelengih. This measurement is performed by using a cut-back technique and gives an attenuation that is not only a function of the spectral attenuation of the rare earth, but which also depends on the overlap between the pump beam and the distribution of the rare earth in the fiber core. The most relevant parameters which have been selected are the spectral attenuation, the fluorescence spectrum, the fluorescence lifetime, the emission cross-section, and finally the spectral unsaturated gain. The implemented measurement techniques are extensively described in the next sections. Our main interest has been focused in the characterization of Nd^{3+} doped fibers, and the measurement setups have been optimized for this purpose. Nevertheless, these techniques can be easily applied to every other kind of dopant.

1.1. Spectral attenuation

The measurement of this parameter is of prime interest to optimize the pump scheme of any active fiber device. This spectral attenuation allows to calculate the absorption cross-section, which is a relevant parameter for the description of the dynamic of the population in a laser transition.

1.1.1. Measurement of the spectral attenuation of fibers with low and medium dopant concentrations

The power loss is described by

$$P(z) = P_0 \exp(-\alpha z), \qquad (1.1)$$

where P_0 is the input power and α is the coefficient of absorption of the waveguide, which can be written as

$$\alpha = \frac{1}{z} \ln\left(\frac{P_0}{P(z)}\right) \tag{1.2}$$

Measuring P_0 and $P(z)$ allows to find the coefficient of absorption α. Nevertheless, measuring P_0 requires an accurate characterization of the coupling efficiency of the probe signal to the fiber core. Measuring of the transmission $P(z)$ for two different fiber lengths L_1 and L_2 (cut-back) allows to overcome this problem. By calculating the ratio of the optical power $P(L_2)$ and $P(L_1)$ one gets by using Eq. (1.2)

$$\alpha = \frac{1}{L_1 - L_2} \ln\frac{P(L_2)}{P(L_1)} = \frac{1}{\Delta L} \ln\frac{P(L_2)}{P(L_1)}. \tag{1.3}$$

The attenuation in dB, A_{dB}, for a fiber of length z is defined as

$$A_{dB}(z) = 10 \log\left(\frac{P_0}{P(z)}\right) = \frac{10}{\ln(10)} \ln\left(\frac{P_0}{P(z)}\right) = \frac{10}{\ln(10)} \alpha z. \tag{1.4}$$

The coefficient of attenuation in dB per unit length, α_{dB} which is commonly used for the representation of the attenuation, is obtained from Eq. (1.4) by

$$\alpha_{dB} = \frac{1}{z} A_{dB}(z) = \alpha \frac{10}{\ln(10)}. \tag{1.5}$$

A standard setup for the measurement of the spectral attenuation is shown in Fig. 1.1.1. It consists of a white light source (Quartz Tungsten Halogen lamp) and of a 1/4 meter monochromator, to produce a tunable optical source at wavelengths between 400 nm and 1.6 µm. The spectral transmission through a short sample of doped fiber is then measured by using a synchronous (lock-in) detection. Measuring the transmission for two different fiber lengths (cut-back) allows to calculate the absolute spectral attenuation of the doped fiber by using Eqs. (1.3) and (1.5). A short wavelength blocking filter is added at the output of the lamp to avoid the overlap between successive diffraction orders of the monochromator. The tunable source is then coupled into a long piece (a few meters) of standard (undoped) fiber to achieve a spatially filtered source and the cladding modes are stripped by using a small diameter fiber loop. The sample of doped fiber is spliced to the standard fiber. Index matching oil is also applied on the fiber extremities to extract the residual cladding modes from the fibers. The transmitted signal is detected with a photomultiplier (S-20 spectral response). This detector has the advantage to be insensitive at the fluorescence wavelengths of Nd^{3+} (930 nm, 1.08 µm,

1.3 μm); no filtering of the pump induced fluorescence is thus required. The spectral resolution for this measurements is typically 0.5 nm.

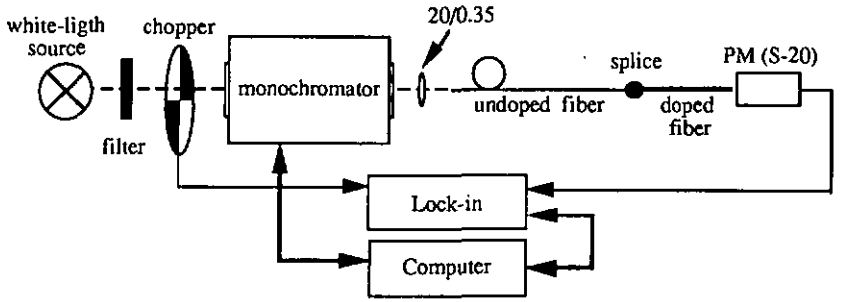

Fig. 1.1.1. Computer controlled white-light spectral attenuation measurement setup.

An example of such measurements is shown in Fig. 1.1.2 for a fiber doped with a low concentration (about 500 ppm) of Nd^{3+}.

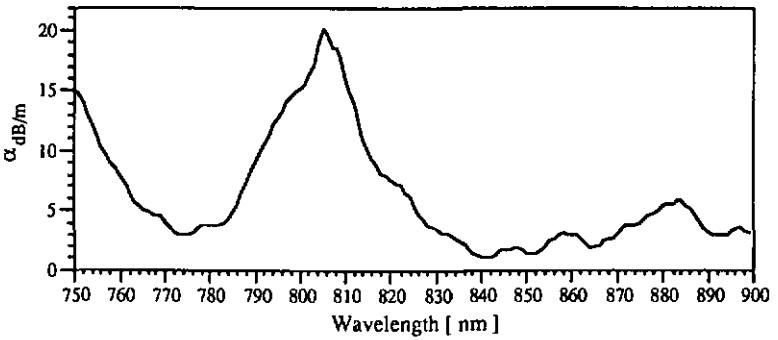

Fig. 1.1.2. Spectral attenuation for a Nd^{3+} lightly doped fiber (fiber CSEM 210192B).

This white-light technique is also well adapted for the measurement of highly doped fibers (with typical peak attenuations up to 500 dB/m), since it is possible to splice very short samples of doped fiber and to perform very short cut-backs. A typical example for the measurement of the spectral attenuation of a highly doped fiber is shown in Fig. 1.1.3. A peak attenuation of 390 dB/m has been measured at 805 nm for the CSEM fiber (180491). For the measurement of extremely high attenuation, for which the optical power provided by the white-light source is not sufficient, a tunable $TiAl_2O_3$ laser is used.

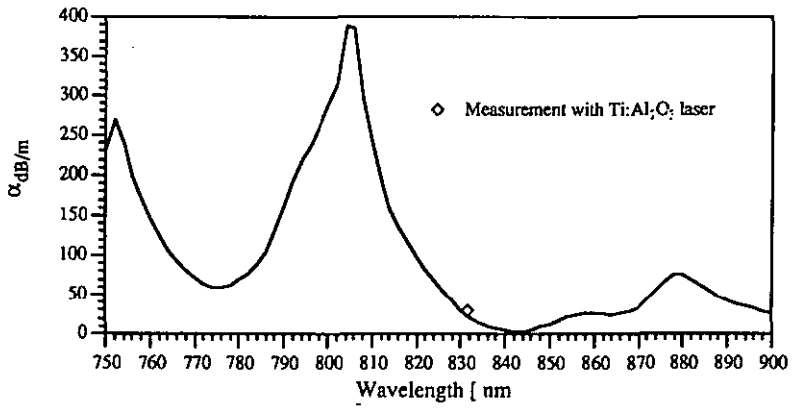

Fig. 1.1.3. Spectral attenuation for an heavily Nd^{3+} doped fiber (CSEM 180491) measured with the white-light technique. A measurement performed with the $TiAl_2O_3$ laser at 832 nm showed a good agreement with the white-light measurement.

The major difficulty for the characterization of high attenuation is the necessity to use very short samples of doped fiber for the measurement (typical length less than 1 cm). In this case, the effect of the residual light which propagates in the cladding modes of the sample strongly disturbs the measurement. We have developed a specific multiple cut-back technique to overcome this problem and to achieve an accurate measurement of very high attenuation. This technique is described in the following section.

1.1.2. Measurement of the spectral attenuation of fibers with very high dopant concentrations

The optical power detected at the output of the fiber is modeled as the superposition of the signal transmitted through the core and the parasitic signal which propagates in the cladding modes. The coefficient of absorption of the core and of the cladding are α_{co} and α_{cl}, respectively. The distribution of the total optical power at a position z along the fiber is then given by

$$P(z) = P_0[k_1 \exp(-\alpha_{co} z) + k_2 \exp(-\alpha_{cl} z)] , \qquad (1.6)$$

where P_0 is the input power, and k_1 and k_2 are the fractions of the power in the core and the cladding modes, respectively. Let us assume that the ratio $\eta = k_1/k_2$ is independent of z, which means that the energy transfer between core and cladding modes is negligible and that therefore the power splitting ratio η is mainly determined by the input coupling. This

assumption is fulfilled for the short samples of fiber which are used for the measurement of the spectral attenuation of highly doped fibers. Let us assume that Δz_c is the length of each cut-back used for the measurement. The ratio of the output power measured at $z - \Delta z_c$ and z is given by

$$\frac{P(z-\Delta z_c)}{P(z)} = \frac{\eta \exp(-\alpha_{co}(z-\Delta z_c)) + \exp(-\alpha_{cl}(z-\Delta z_c))}{\eta \exp(-\alpha_{co} z) + \exp(-\alpha_{cl} z)} \qquad (1.7)$$

The measured spectral coefficient of attenuation α_{dB} depends on the length z of the fiber. This coefficient can be calculated by using Eqs. (1.7) (1.3) and (1.4). This yields

$$\alpha_{dB}(z) = \frac{10}{\ln(10)} \frac{1}{\Delta z_c} \ln\left[\frac{\eta \exp(-\alpha_{co}(z-\Delta z_c)) + \exp(-\alpha_{cl}(z-\Delta z_c))}{\eta \exp(-\alpha_{co} z) + \exp(-\alpha_{cl} z)}\right]. \qquad (1.8)$$

Fig. 1.1.4 shows α_{dB} as a function of the position z of the cut-back along a fiber, calculated from Eq. (1.8), with 175 dB/m of attenuation in the core and 15 dB/m of attenuation in the cladding, and a core/cladding power ratio $\eta = 1 \cdot 10^5$. This characteristic is shown for different values of Δz_c (5 cm, 10 cm, 15 cm).

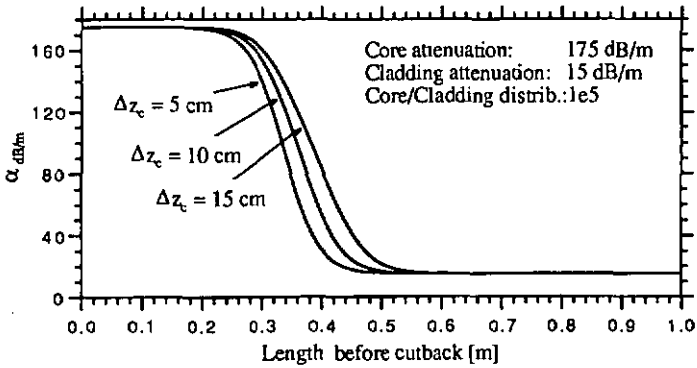

Fig. 1.1.4. Attenuation as a function of the position of the cut-back along the fiber, for different values of Δz_c.

The measurement of this characteristic allows to extrapolate the values of α_{co}, α_{cl}, and η by fitting Eq. (1.8) to the measured α_{dB} as a function of z. The free parameters for the fit are α_{co}, α_{cl} and η. The starting value of α_{cl} necessary for the convergence of the fit can be immediately found from the graph, by considering the asymptotic value $\alpha(z \to \infty)_{dB} = \alpha_{cl}$. The feasibility of this technique has been theoretically verified by considering a simulated measurements, as shown in Fig. 1.1.5. It consists of seven points taken from the curve

Δz_c = 5 cm of Fig. 1.1.4. The results of the fit with Eq. (1.8) are in good agreement with the initial values for the three values of interest, namely α_{co}, α_{cl} and η.

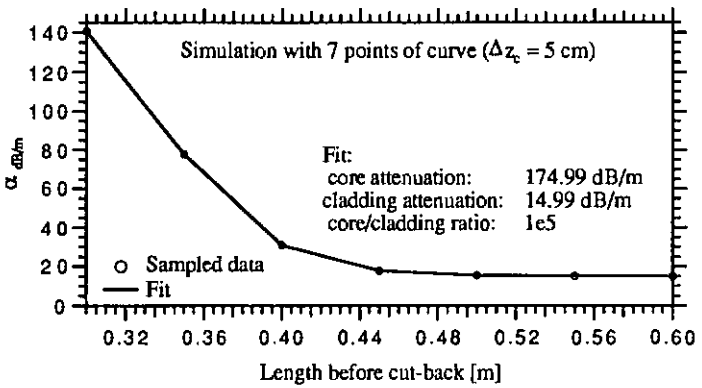

Fig. 1.1.5. Fit calculated with Eq. (1.8) on a simulated set of seven data taken from Fig. 1.1.4.

This technique has been used to measure the attenuation at 810 nm of a heavily Nd^{3+} doped fiber (>10000 ppm mol, CSEM 100192B). The pump was a $TiAl_2O_3$ laser at 810 nm. Fig. 1.1.6 shows the measured values and the fitted curve. An attenuation of 173 dB/m has been measured for the core. The attenuation of the cladding modes was found to be 11 dB/m, and the core/cladding power ratio was $1.2 \cdot 10^5$.

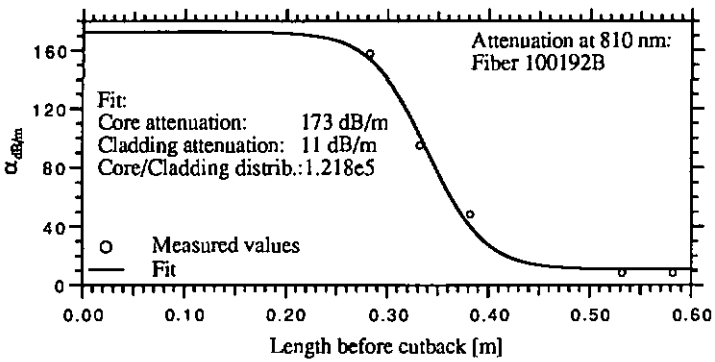

Fig. 1.1.6. Measurement of the attenuation of a Nd^{3+} doped fiber. The circles are the measured values and the line is the fitted curve.

This technique offers a powerful tool to measure very high attenuations (typical attenuations larger than 500 dB/m) when the contributions of the cladding modes are not negligible, but it is also useful for the measurement of the pump coupling efficiency in double clad fibers, which is of interest for high power fiber lasers [1.11].

1.2. Fluorescence spectrum

The measurement of fluorescence spectra is very similar to the measurement of absorption spectra. The light from a Ti:Al_2O_3 laser or a laser diode operating at a wavelength near 820 nm is launched into the doped fiber. The fluorescence is then analyzed using a 1/4 meter monochromator over the range of 880 - 1160 nm. A photomultiplier with a spectral sensitivity adapted for detection in the near infrared (S-1: 0.4 μm – 1.2 μm) and a conventional lock-in amplifier is used to record the spectrum. The fluorescence spectrum of a typical Nd^{3+} doped fiber is shown in Fig. 1.2.1. The fluorescence peaks corresponding to the transitions $^4F_{3/2}$ - $^4I_{9/2}$ at 930 nm and $^4F_{3/2}$ -$^4I_{11/2}$ at 1.06 μm can be observed. If an absolute measurement of the fluorescence spectrum is required, great care must be taken to ensure no reabsorption of the three level transition at 930 nm, and no significant amplification of the four level transition at 1.06 μm. This problem can be overcome by collecting the fluorescence perpendicular to the fiber axis and near the launching end of the fiber, or by using very short samples of doped fiber and very weak pump power.

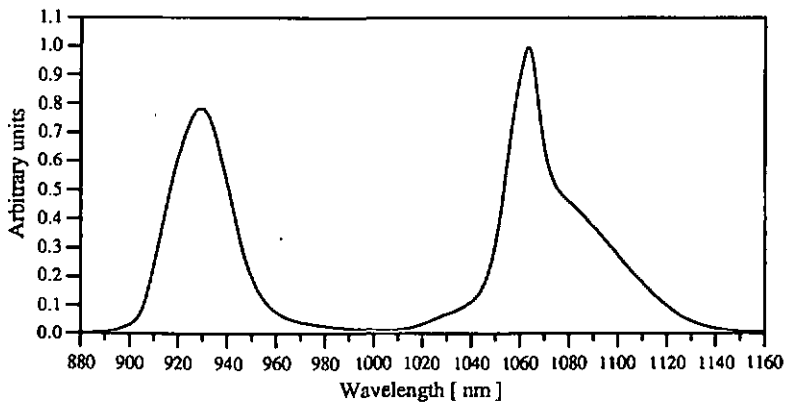

Fig. 1.2.1. Fluorescence spectrum of the Nd^{3+} doped fiber CSEM (180491).

The measurement of the fluorescence spectrum allows to extrapolate the value of the emission cross-section. This parameters is a key element in the evaluation of the gain properties of an active fiber device, as it will be derived in Sect. 2. This value can be calculated by using the

Fuchtbauer Ladenburg formula which was derived from the theoretical work of Judd and Offelt [1.1]. The basic assumptions which has to be fulfilled to use this technique is that the Stark sublevels of each manifold of the laser transition are equally populated. Nevertheless, Krupke [1.2] showed that this assumption is never satisfied at room temperature in a crystalline structure. But, the low symmetry coordination of the amorphous host material has as consequence that this basic assumption on the population of the Stark sublevels is fulfilled for amorphous glasses. The Judd Offelt analysis and consequently the Fuchtbauer Ladenburg technique are applicable for the characterization of the emission cross-section of silica based rare earth doped fibers [1.3], [1.4], in opposition to the statement given in [1.5]. The basic equation of the Fuchtbauer Ladenburg method connects the peak emission cross-section to the fluorescence spectrum by [1.3]

$$\sigma_{peak} = \frac{\lambda_{peak}^4}{\tau_{spont}\, 8\pi c n^2\, \Delta\lambda_{eff}}, \tag{1.9}$$

where λ_{peak} is the peak fluorescence wavelength, $\Delta\lambda_{eff}$ is the effective fluorescence spectral width. The effective width $\Delta\lambda_{eff}$ is obtained from the relation

$$\Delta\lambda_{eff}\ f(\lambda_{peak}) = \int_0^\infty f(\lambda)\, d\lambda, \tag{1.10}$$

where $f(\lambda)$ is the line shape, t_{spont} is the spontaneous lifetime, n is the index of refraction of the host material. The spontaneous lifetime τ_{spont} is connected to the fluorescence lifetime τ_f through the effective branching ratio β_r of the transition of interest by the equation [1.3]

$$\tau_{spont} = \frac{1}{\beta_r}\tau_f. \tag{1.11}$$

This effective branching ratio can be experimentally obtained by measuring the fluorescence power for all the radiative transitions originating from the upper level of interest. The emission cross-section for the transition at 1.06 mm of the fiber CSEM (180491) has been calculated from the graph shown in Fig. 1.2.1. The measured fluorescence lifetime (see Sect. 1.3) was 485 μs, the peak wavelength was 1.063 μm, the branching ratio $\beta_r = 0.4$ was taken from [1.3] for the transition, and $n = 1.46$. This gives for the peak emission cross-section $\sigma_{peak} = (1.8 \pm 0.3) \cdot 10^{-24}\ m^2$. This fiber does not contain any Ge co-doping, but has been co-doped with phosphorus and aluminum; for that reason the emission wavelength is centered around 1.06 μm instead of the 1.08 μm which is obtained for Nd^{3+}:SiO_2 and Nd^{3+}: SiO_2: GeO_2. This fact is also believed to explain the larger measured value for the emission cross-section than reported in SiO_2: GeO_2 fibers {$\sigma_{peak} = (1.3 \pm 0.2) \cdot 10^{-24}\ m^2$}

[1.8]. As a comparison, we have measured the peak emission cross-section of a 500 ppm Nd^{3+}:SiO_2: GeO_2 fiber by using the same technique. The result was $\sigma_{peak} = (1.5 \pm 0.3) \cdot 10^{-24}$ m^2, which is in a good agreement with the value given in [1.3]. Some other techniques for the measurement of σ_{peak}, which involve the measurement of the properties of fiber laser cavities, have been proposed [1.3]. Nevertheless, they suffer from some drawbacks, mainly due to the effect of non radiative decay processes which may affect the measurement, as shown in [1.3] and [1.5].

1.3. Fluorescence decay time

We consider in this section two different techniques for the measurement of the fluorescence lifetime which are based on the measurement of the dynamic of the spontaneous emission. These techniques are discussed in 1.3.1 and 1.3.2. The measurement of the fluorescence decay time provides two important results. First, it gives the measure of the lifetime of the upper level of the radiative transition, but it also provides some important indications on the efficiency of the ion-ion interactions which may occur in the active medium. The measurement of this parameter is particularly of interest to evaluate the effect of the concentration quenching in heavily rare earth doped fibers. This effect strongly reduces the efficiency of any active fiber device. In the case of Nd^{3+} doped fibers, we are interested in the measurement of the lifetime of the upper level $^4F_{3/2}$ of the laser transition, as it is shown in the partial energy level diagram of Fig. 1.2.2. This level is the upper level of the three radiative transitions at 0.93 µm, 1,06 µm and 1.3 µm.

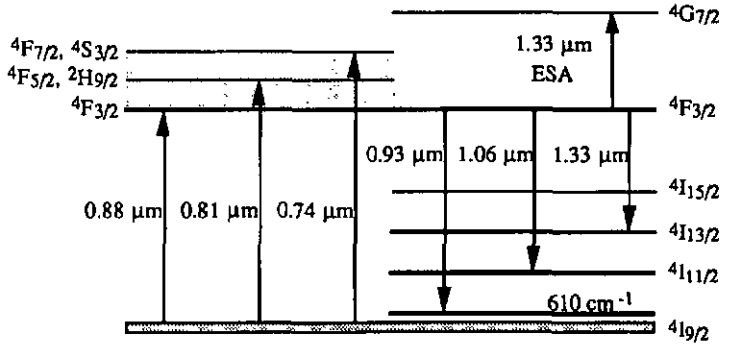

Fig. 1.2.2. Partial energy level diagram of Nd^{3+}: SiO_2, ar Nd^{3+}: SiO_2: GeO_2. The transition at 1.33 µm suffers from severe excited state absorption (ESA), which strongly limits the efficiency of this radiative transition.

1.3.1. Determination of the lifetime by measuring the decay of the fluorescence

The principle of this measurement is to establish an initial inversion N_0 of the population between the ground level $^4I_{9/2}$ and the upper level $^4F_{3/2}$ by applying a weak initial pumping. Then the pump is switched off rapidly and the decay of the fluorescence is measured. The switching time used for the measurements is smaller than 1 µs. If we assume a two level description of the transition (see Sect. 2) and negligible contributions from stimulated emission and from reabsorption, the decay of the inversion N is given by

$$\frac{dN}{dt} = -N\frac{1}{\tau_{21}}, \tag{1.12}$$

where τ_{21} is the fluorescence lifetime. This yields after integration

$$N(t) = N_0 \exp(-\frac{t}{\tau_{21}}). \tag{1.13}$$

Since the fluorescence is proportional to the inversion N, we get an exponential decay of the fluorescence, from which the decay time can be determined.

A standard setup for this measurement is shown in Fig. 1.3.1. A short sample of doped fiber is pumped with a pulse provided by a laser diode at 810 nm. The induced fluorescence is detected with a Si photodiode and processed with a computer, in order to extract the value of τ_{21} from the measured fluorescence decay by fitting the measured curve to Eq. (1.13).

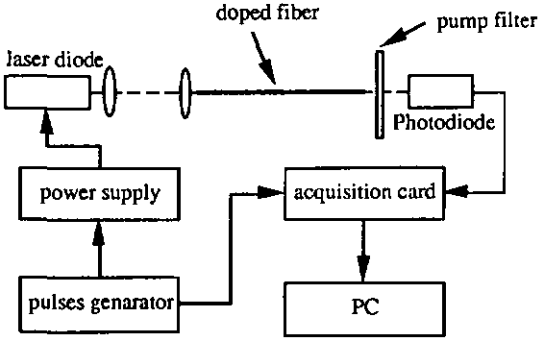

Fig. 1.3.1 Setup for the measurement of the fluorescence lifetime. A filter is added in front of the photodiode to remove any residual pump light.

A critical point is to avoid the effect of amplification of the spontaneous emission and the reabsorption along the fiber, which would alter the measurement. This can be achieved either by using a very short sample of fiber and a detection of the fluorescence at the fiber end, or by a lateral detection of the fluorescence, near the pumping end of the fiber. Fig. 1.3.2 shows a typical measurement on a lightly Nd^{3+} doped fiber. The lifetime obtained by fitting the measured decay to Eq. (1.13) gives $\tau_f = (485 \pm 5)$ µs.

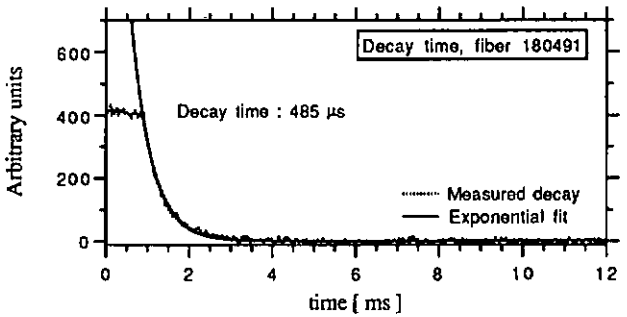

Fig. 1.3.2 Measurement of the fluorescence decay time of fiber CSEM 180491. A typical lifetime $\tau_f = 485$ µs has been obtained from the exponential fit of the decay.

When the dopant concentration is very high (typically larger than 10000 ppm) [1.6], the distance between the ions is strongly reduced and non radiative processes (concentration quenching) due to ion-ion interactions may occur. The fluorescence decay does not remain a pure exponential, as extensively described in [1.7]. This can be seen in Fig. 1.3.3, where the fluorescence of a heavily doped fiber (concentration > 10000 ppm) has been measured.

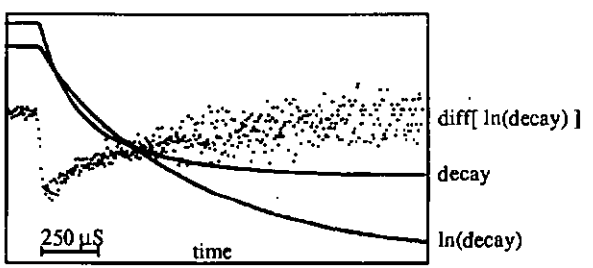

Fig. 1.3.3. Fluorescence decay of a heavily doped fiber (CSEM 160491). Evidence of strong concentration quenching can be observed. The fast initial decay is due to some clustering of the dopant in the fiber core.

The detected signal has been acquired with a Tektronix 7854 digital storage oscilloscope. A real time signal processing allows to calculate the logarithm and the derivative of the logarithm to determine the decay rate and the deviation from the exponential behavior. It is seen that the decay is not a pure exponential. This becomes even more clear by considering the logarithm of the decay, which is no longer a straight line. The derivative of the logarithm shows a fast initial decay, which is believed to be the effect of an important concentration quenching due to some clustering of the dopant in the fiber core.

1.3.2. Determination of the fluorescence lifetime by measuring the transfer function

We propose in this section another method for the measurement of the fluorescence decay time, by measuring the transfer function of the active medium. We have seen in 1.3.2 that the impulse response of an ideal active fiber is a pure exponential. This means that the transfer function in the frequency domain is identical to the frequency response of a first order low-pass filter. This transfer function can be measured by modulating the pump power (input signal) and measuring the resulting modulation of the fluorescence (output signal). The modulated pump power is

$$P(t) = P_0 \{1 + \cos(2\pi \nu_m(t)\, t)\}, \tag{1.14}$$

where P_0 is the mean optical power, $\nu_m(t)$ is the frequency of the modulation. As in standard electronic network analysis, the modulation frequency is swept linearly over a certain frequency range. The fluorescence decay time is obtained directly from the –3 dB cutoff frequency ν_c by

$$\tau_f = \frac{1}{2\pi \nu_c}. \tag{1.15}$$

The measurement of the frequency phase response is commonly used for the analysis of the fluorescence lifetime in the domain of the chemistry [1.10]. On the other hand, this is the first time to our knowledge that the measurement of the cutoff frequency is applied to the measurement of the fluorescence lifetime of doped fibers. The basic principle for the measurement of the MTF is shown in Fig. 1.3.4.

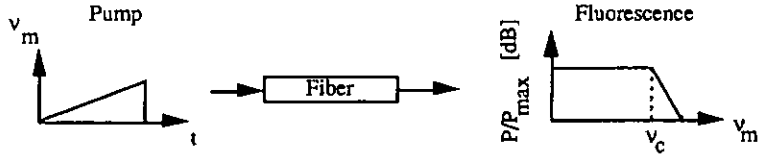

Fig. 1.3.4. Determination of the fluorescence lifetime by measuring the transfer function. The input is the modulated pump power, and the output is the resulting modulation of the fluorescence. The fluorescence lifetime is given by $\tau_f = 1/2\pi\nu_c$, where ν_c is the cutoff frequency.

The experimental setup for the measurement of the transfer function (MTF) is shown in Fig. 1.3.5. The pump beam is provided by a laser diode at 825 nm. An optical isolator (OI) is used to avoid feedback effects, which would distort the linearity of the frequency modulation. The detector is a silicon photodiode. An optical filter (F) is used to remove all residual pump light. The modulation of the laser diode and the synchronous detection of the transfer function are simultaneously provided by a network analyzer (HP 4195). The mean output power of the laser diode was very low, typically 500 µW, in order to avoid any significant amplification inside the fiber; for the same reason, the mean value of the modulation (DC signal) was kept as low as possible to minimize the DC induced inversion. The pump coupling efficiency into the fiber was 30 %, and the Nd^{3+} doped fiber (NdF) had typically a length of a few centimeters.

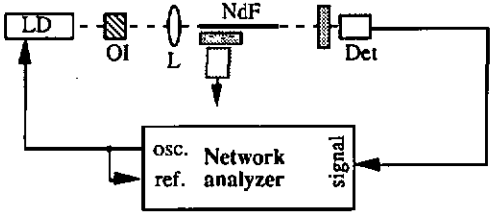

Fig. 1.3.5. Experimental setup for the MTF. LD: moduloted pump laser diode, OI: optical isolator, F: optical filter, NdF: neodymium doped fiber, Det: silicon detector. The fluorescence is detected either at the fiber end or on the fiber side.

The first fiber which was measured was a 500 ppm Nd^{3+} doped fiber. The transfer function measured between 10 Hz and 1 kHz is shown in Fig. 1.3.6.

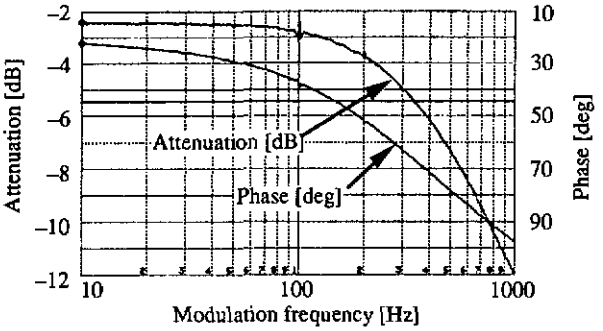

Fig. 1.3.6. Transfer function of a 500 ppm Nd^{3+} doped fiber. The cutoff frequency is 339 Hz, which gives a lifetime of 469 μs.

The typical behavior of a first order low-pass filter has been observed. The value of the –3 dB cutoff frequency was ν_c = 339 Hz, which gives a lifetime of 469 μs. The accuracy of the measurement has been estimated to be 2 %. The value obtained from the fluorescence decay (Sect. 1.3.1) is τ_f = 471 μs, with an accuracy of 1 %. The results for the two methods are in excellent agreement. The main limitations in the resolution are given by the feedback into the pump laser diode, which distorts the input signal, and by the spectral resolution of the network analyzer.

In a second experiment, a highly doped fiber (10000 ppm) has been measured. The fluorescence decay of this fiber has been measured previously (Sect. 1.3.1) and a reduction of the lifetime due to concentration quenching was observed. From a simple exponential fit of the decay we got τ_f = 338 μs, and a double exponential fit showed a fast and a slow component of 120 μs and 402 μs, respectively. The result of the MTF is shown in Fig. 1.3.7. The –3 dB cutoff frequency gives τ_f = 336 μs, which is again in good agreement with the single exponential fit. It must be pointed out that the slow and fast components of τ_f cannot be immediately read from the transfer function. However, these values can be extracted from the transfer function by using appropriate curve fitting using a second order expression for the transfer function. The extraction of the fast component τ_f = 120 μs requires a modulation frequency which is higher than the maximum frequency of 1 kHz available in the present experiment. Consequently the effect of the second cutoff frequency cannot be seen in the transfer function of Fig. 1.3.7.

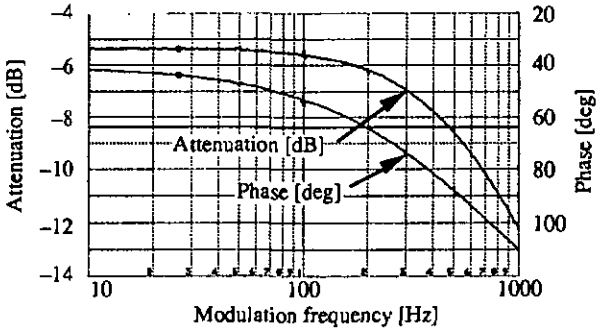

Fig. 1.3.7. Transfer function of a concentration quenched fiber, the –3 dB cutoff frequency is 473 Hz, which gives a lifetime of 338 μs.

The MTF technique is of interest because only low pump power is required for the measurement, which allows to minimize the ASE (Amplification of Spontaneous Emission). This can be more easily achieved with the MTF than with the impulse response method since the MTF is obtained by synchronous detection. A lateral measurement of the weak unguided fluorescence allows to minimize the effects of the amplification and the reabsorption, as discussed in 1.3.1. The MTF technique gives a straightforward measurement of the lifetime of lightly doped fibers, which do not show concentration quenching effects. Nevertheless, this technique can also be applied in other cases, using additional signal processing which involves the fitting of the measured transfer function to an analytical model which describes the departure from the pure exponential decay of the fluorescence [1.9]. As previously discussed, a simpler model which includes two exponential components for the fluorescence decay could also be considered.

1.4. Spectral gain

In this section, we describe the characterization of the gain of a Nd^{3+} doped fiber as a function of the signal wavelength. This measurement gives important indications on the spectral properties of the active medium, such as the effective spectral width of the gain curve and the effects of the excited state absorption (ESA). The basic setup for this measurement is shown in Fig. 1.4.1.

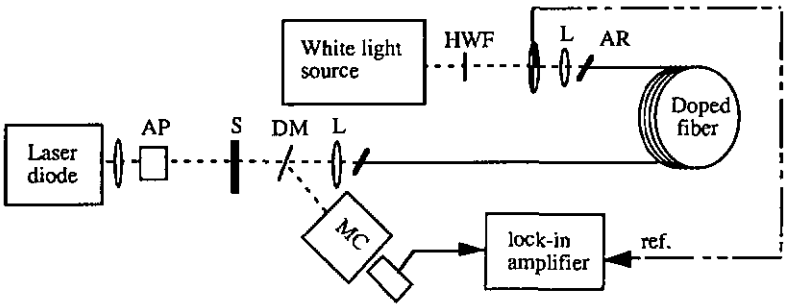

Fig. 1.4.1. Measurement of the spectral gain of a Nd^{3+} doped fiber. The input signal is given by a white-light source (tungsten halogen), passed through a short wavelength blocking filter to get a spectrum between 900 and 1200 nm. The pump is a laser diode at 810 nm.

The sample of doped fiber is pumped with a laser diode at 810 nm. The fiber ends are polished at an angle of 12° to avoid any cavity effect [1.13]. An anamorphic prism pair (AP) is used to correct the ellipticity of the laser diode beam. The input signal is provided by a white light source filtered through a short wavelength blocking filter (HWF, 900-1200 nm). The amplified signal is measured by synchronous detection (lock-in) of the output from a 1/4 meter monochromator (MC). The dichroic mirror (DM) separates the pump beam and the amplified signal. The spectral gain properties of a commercially available Nd^{3+} doped fiber have been studied. The fiber is a 500 ppm Nd^{3+} doped fiber with NA = 0.21 and a core diameter of 3.5 μm. The spectral gain is obtained by measuring the spectral power at the output of the monochromator when the amplifier is pumped (shutter (S) open) and unpumped (shutter (S) closed), and by calculating the ratio of these two measurements. Figure 1.4.2 shows the measured spectral gain of this amplifier.

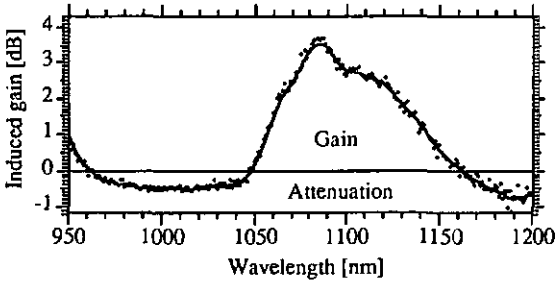

Fig. 1.4.2. Induced spectral gain in a 9.5 m long Nd^{3+} doped fiber amplifier. The pump is a high power laser diode at 810 nm. The input signal was provided by a filtered white light source.

This measurement shows that an attenuation of the probe signal is obtained between 970 and 1050 nm, because of Excited State Absorption (ESA).

1.5. Conclusions

The basic techniques which are necessary for the characterization of the fundamental properties of rare earth doped fibers have been discussed in this chapter. Most of these measurement use well established methods, such as the cut-back for the characterization of the spectral attenuation or the analysis of the fluorescence decay for the measurement of the lifetime of the upper level of a radiative transition. Nevertheless some important improvements and modifications of these techniques have been introduced:

A method for the measurement of the spectral attenuation of highly doped fibers which allows to overcome the problem of the cladding modes has been successively demonstrated (Sect. 1.1.2). Attenuations of more than 500 dB/m can be easily measured with this technique.

The determination of the fluorescence decay time by measuring the transfer function of the active fiber has been demonstrated in Sec. 1.3.2. This technique has the advantage to use a synchronous detection which allows low pump power for the measurement. Consequently, the ASE (amplification of spontaneous emission) which is detrimental to the measurement, can be strongly minimized. A typical accuracy of 2 % on the measurement of the fluorescence decay time has been obtained with this technique.

2. Gain properties of doped fibers

2.1. Rate equations for the steady state in a four level homogeneous active medium

As shown in Fig. 2.1.1, a two level approximation of the transitions is considered by assuming a fast non radiative decay from the metastable level 3 to 2 and a fast depopulation of the lower level of the laser transition from 1 to 0,

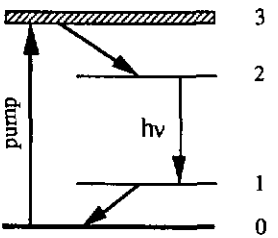

Fig. 2.1.1. Simplified energy level diagram of a four level laser system.

The rate equations for the population of the levels and for the density of the photons at steady state can be written as

$$\frac{dN_2}{dt} = P - (N_2 - N_1)\,\sigma\eta c - \frac{N_2}{\tau_{21}} = 0, \tag{2.1}$$

$$\frac{dN_1}{dt} = (N_2 - N_1)\,\sigma\eta c + \frac{N_2}{\tau_{21}} - \frac{N_1}{\tau_1} = 0, \tag{2.2}$$

$$\frac{d\eta}{dt} = (N_2 - N_1)\,\sigma\eta c + \frac{N_2}{\tau_{21}} - \beta\eta c = 0, \tag{2.3}$$

where P is the pumping rate ($m^{-3}\,s^{-1}$), N_i is the density of population (m^{-3}) of level i, σ is the emission cross-section (m^2), τ_{21} is the fluorescence lifetime (s), η is the signal photon density (m^{-3}), β is the loss coefficient of the material (m^{-1}) and c is the speed of light in vacuum (m/s). If we consider a 4 level system, the population N_1 of the lower level of the transition can be neglected, and the inversion $N = N_2 - N_1 = N_2$ at steady state can be written as

$$\frac{dN}{dt} = P - N\,\sigma\eta c - \frac{N}{\tau_{21}} = 0. \tag{2.4}$$

These equations have to be adapted in the case of a guided structure, which gives a non uniform distribution of the inversion and the pump and signal beams inside the active medium. The densities of population in Eqs. (2.1), (2.2), (2.3) have to be replaced by the local distribution of the densities [4.5], namely $p(r,\phi,z)=P_p(z)P(r,\phi)$, $n(r,\phi,z)$ and $\eta(r,\phi,z) = \eta_0(z)\, S(r,\phi)$ for the pumping rate, the inversion and the photon densities, respectively. $P(r,\phi)$ and $S(r,\phi)$ represent the normalized radial pump and signal distributions inside the fiber core and $P_p(z)$, $S(z)$ the corresponding distributions along z. Equations (2.4) and (2.3) can thus be written as

$$\frac{dn(r,\phi,z)}{dt} = p(r,\phi,z) - n(r,\phi,z)\,\eta(r,\phi,z)\,\sigma c - \frac{n(r,\phi,z)}{\tau_{21}} = 0, \qquad (2.5)$$

$$\frac{d\eta_0(z)}{dt} = \int_0^{2\pi} d\phi \int_0^{r_d} dr\, r \left[n(r,\phi,z)\,\sigma\eta(r,\phi,z)c + \frac{n(r,\phi,z)}{\tau_{21}} \right] - \beta(z)\eta_0(z)c = 0, \qquad (2.6)$$

where r_d is the radius of the active domain (doped part of the fiber core).The rate equation for the population density (2.5) has to be considered locally, because the excited ions are localized and diffusion is negligible. On the other hand, the rate equation for the photons (2.6) has to be satisfied for the integral over the cross section, since the photons are not localized within the waveguide. By introducing (2.5) into (2.6), and by using the definitions of $\eta(r,\phi,z)$ and $p(r,\phi,z)$, one finds

$$\int_0^{2\pi} d\phi \int_0^{r_d} dr\, r \frac{P(r,\phi)\, S(r,\phi)}{c\sigma\tau_{21}\eta_0(z)\, S(r,\phi) + 1} = \frac{\beta(z)}{P_p(z)\sigma\tau_{21}}. \qquad (2.7)$$

By equating $\gamma(z) = \beta(z)$, where $\gamma(z)$ is the gain coefficient, one finds at steady state

$$\gamma(z) = P_p(z)\sigma\tau_{21} \int_0^{2\pi} d\phi \int_0^{r_d} dr\, r \frac{P(r,\phi)\, S(r,\phi)}{c\sigma\tau_{21}\eta_0(z)\, S(r,\phi) + 1} \qquad (2.8)$$

It must be pointed out that the emission cross-section σ and the emitted signal are wavelength dependent: $\sigma = \sigma(\nu)$, and $\eta_0 = \eta_0(\nu)$. In that general case, Eq. (2.8) must be written in the form

$$\gamma(z,\nu) = P_p(z)\sigma(\nu)\tau_{21} \int_0^{2\pi} d\phi \int_0^{r_d} dr\, r \frac{P(r,\phi)\, S(r,\phi)}{\int_{\Delta\nu} c\sigma(\nu)\tau_{21}\, \eta_0(z,\nu)\, S(r,\phi)\, d\nu + 1}. \qquad (2.9)$$

For the remaining part of this study, only the monochromatic case will be considered, since it is relevant for most laser applications. The integral of saturation of Eq. (2.9) can be expressed as a function of the signal power $P_f(z) = \eta_0(z)hvc$ (W) and the saturation intensity, defined as $I_{sat} = h\nu/\sigma\tau_{21}$ (W/m^2). This yields

$$\gamma(z) = P_p(z)\sigma\tau_{21} \int_0^{2\pi} d\phi \int_0^{r_d} dr\, r \frac{P(r,\phi)\, S(r,\phi)}{1 + S(r,\phi)\frac{P_f(z)}{I_{sat}}}. \qquad (2.10)$$

By assuming no saturation of the pump absorption and no ground state depletion, the absorbed pump power between z = 0 and z along the fiber is given by

$$P_{abs}(z) = P_{in}\,[1 - \exp(-\alpha_p \eta_p z)], \qquad (2.11)$$

where η_p is the fraction of the pump power contained in the fiber core, given by Eq. 2.26. The longitudinal distribution of the pumping rate $P_p(z)$ is thus given by

$$P_p(z) = \frac{1}{h\nu_p}\frac{dP_{abs}}{dz}\eta_c, \qquad (2.12)$$

where η_c is the pump efficiency connecting the absorbed pump power to the pumping rate of the upper level of the radiative transition. The gain coefficient integrated over a fiber length L is then given by

$$\Gamma(L) = \int_0^L \gamma(z)\, dz. \qquad (2.13)$$

Equations (2.10), (2.12) and (2.13) are useful to evaluate the gain of single mode amplifiers, lasers or superfluoreseent sources, based on a four level system. This model allows to investigate the effect of the waveguide on the gain properties by considering the exact distribution of the signal and pump modes which are guided in the fiber.

2.2. Modal properties of the fiber

The pump and signal distributions $S(r,\Phi)$ and $P(r,\Phi)$ which are necessary to calculate the gain coefficient $\gamma(z)$ can be obtained from the solutions of the Maxwell' s equations in a cylindrical waveguide. By assuming a weakly guiding fiber (i.e. a small index change between the fiber core and cladding), the normalized power distributions for the fundamental LP01 and first order LP11 modes can be written as [2.1]

$$I_{LP01}(r,\phi) = \frac{1}{\pi\rho^2}\left(\frac{U\ K_0(W)\ J_0(U\ r/\rho)}{V\ K_1(W)\ J_0(U)}\right)^2, \qquad 0 \le r \le \rho \qquad (2.14)$$

$$I_{LP01}(r,\phi) = \frac{1}{\pi\rho^2}\left(\frac{U\ K_0(W)\ K_0(U\ r/\rho)}{V\ K_1(W)\ K_0(U)}\right)^2, \qquad \rho \le r < \infty \qquad (2.15)$$

and

$$I_{LP11}(r,\phi) = \frac{K_1^2(W)}{\pi\rho^2\ K_0(W)\ K_2(W)}\left(\frac{U\ J_1(U\ r/\rho)}{V\ J_1(U)}\right)^2 F^2(\phi), \qquad 0 \le r \le \rho \qquad (2.16)$$

$$I_{LP11}(r,\phi) = \frac{1}{\pi\rho^2\ K_0(W)\ K_2(W)}\left(\frac{U\ K_1(U\ r/\rho)}{V}\right)^2 F^2(\phi), \qquad \rho \le r < \infty \qquad (2.17)$$

where ρ is the fiber core diameter. The angular distribution $F(\phi)$ is given by the function $F(\phi) = \cos^2(\phi)$ and $F(\phi) = \sin^2(\phi)$ for the two configurations of LP11 modes. The U, V, W parameters are related by $V^2 = U^2 + W^2$. The values of U and W are obtained by the resolution of the transcendental equations:

$$U\frac{J_1(U)}{J_0(U)} = W\frac{K_1(W)}{K_0(W)}, \text{ for the LP01 mode,} \qquad (2.18)$$

$$U\frac{J_2(U)}{J_1(U)} = W\frac{K_2(W)}{K_1(W)}, \text{ for the LP11 modes.} \qquad (2.19)$$

The $J_m(z)$ are Bessel functions of the first kind of order m, and $K_n(z)$ are modified Bessel functions of the second kind and of order n. The power distributions $I_{LPn1}(r,\phi)$ $(n = 0, 1)$ are normalized to a unity total power, namely

$$\int_0^{2\pi} d\phi \int_0^{r_d} dr\, r\, I_{LPn1}(r,\phi) = 1. \qquad (2.20)$$

An example of the distribution of the signal and pump modes in a fiber, calculated by using Eqs. (2.14) to (2.17), is shown in Fig. 2.2.1. The fiber parameters are NA = 0.21, core radius a = 1.75 μm, pump wavelength λ_p = 832.7 nm, signal wavelength λ_s = 1088.9 nm. An important spreading of the LP11 mode into the cladding of the fiber can be observed. In this case, only 73.6 % of the total power of the LP11 mode is contained in the fiber core.

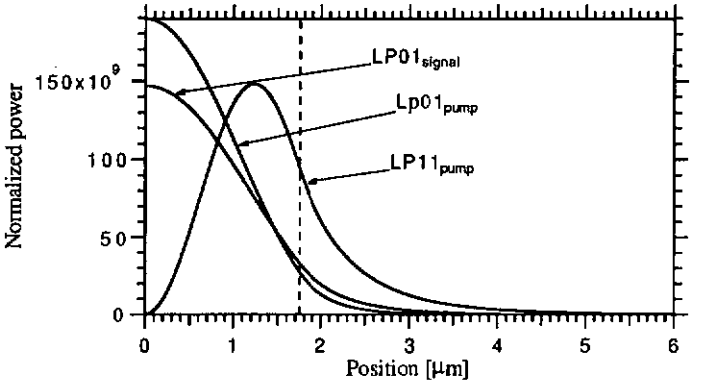

Fig. 2.2.1. Distribution of the signal and pump modes in a fiber. The fiber parameters are NA = 0.21, core radius a = 1.75 μm. The vertical line shows the boundary of the fiber core.

2.3. Unsaturated and small signal gains

The unsaturated gain coefficient $\Gamma_0(L)$ can be easily obtained from Eqs. (2.10) and (2.13) by assuming $\eta_0(z) = 0$. By using Eq. (2.12) this yields,

$$\Gamma_0(L) = \frac{\sigma\tau_{21}}{h\nu_p} P_{abs}\, \eta_c \int_0^{2\pi} d\phi \int_0^{r_d} dr\, r\, P(r,\phi)\, S(r,\phi) = \frac{\sigma\tau_{21}}{h\nu_p} \frac{1}{A_{eff}} P_{abs}\, \eta_c, \qquad (2.21)$$

where the inverse of the overlap integral is interpreted as an effective mode area A_{eff}, namely

$$\frac{1}{A_{eff}} = \int_0^{2\pi} d\phi \int_0^{r_d} dr\, r\, d\phi\, P(r,\phi)\, S(r,\phi). \qquad (2.22)$$

A_{eff} can be related to the fiber core area A_f [2.2] through a parameter F, which is a function of the properties of the pump and signal modes, namely

$$A_{eff} = \frac{1}{F} A_f. \qquad (2.23)$$

The unsaturated gain coefficient is then given by

$$\Gamma_o(L) = \frac{\sigma\tau_{21}}{h\nu_p} \frac{F}{A_f} P_{abs}\, \eta_c. \qquad (2.24)$$

It has been shown [2.2] that Eq. (2.24) gives also a good approximation of the small signal gain coefficient $\Gamma(L)$ of an amplifier where the pump beam is totally confined inside the fiber core. In a more general case of a mode which is not totally confined inside the fiber core and by using the assumption of a uniform distribution of the signal mode $S(r, \Phi)$ in the denominator of Eq. (2.10) [2.3], the approximation for the small signal gain coefficient $\Gamma(L)$ can be written as

$$\Gamma(L) = \frac{\sigma\tau_{21}}{h\nu_p} \frac{1}{A_f} \frac{F}{\eta_p} P_{abs}\, \eta_c, \qquad (2.25)$$

where the coefficient

$$\eta_p = \int_0^{2\pi} d\phi \int_0^{r_d} dr\, r\, P(r,\Phi) \qquad (2.26)$$

takes into account the extension of the pump mode into the fiber cladding. The analysis of Eq. (2.25) shows that the gain coefficient strongly depends on the ratio F/η_p, which describes the mode overlap (F) and the fraction of the pump mode which is contained in the fiber core (η_p). This coefficient has been numerically calculated by integrating the overlap integral of Eq. (2.22) and by using Eqs. (2.23) and (2.26) for a fiber which is pumped at 810 nm and emits at 1.088 µm. The ratio F/η_p is shown in Fig. 2.3.1 for a LP01 and a LP11 pump mode. The signal is assumed to propagate in a LP01 mode. It clearly appears that the coefficient F/η_p is maximum for the LP01 pump mode and that the highest gain will be achieved in a fiber with a cutoff allowing both the signal and pump to be singlemode. But this is not always possible, since the signal wavelength has also to be sufficiently close to the cutoff wavelength to ensure good guiding, and thus to avoid bending losses.

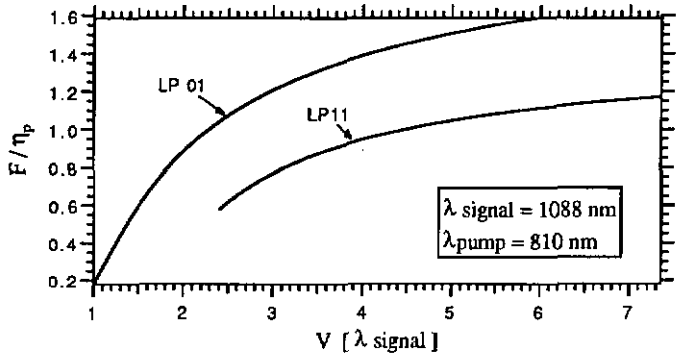

Fig. 2.3.1. $F(\eta_p$ as a function of the V number of the fiber at the signal wavelength. $V = 2\pi a/\lambda NA$, where a is the core radius and NA is the numerical aperture.

The small signal gain of a 500 ppm Nd^{3+} doped fiber has been measured by using the setup which is described in Fig. 2.3.2. The fiber parameters are NA = 0.21, core radius a = 1.75 μm, fluorescence lifetime τ = 470 μs, emission cross-section $\sigma = 1.3 \cdot 10^{-24}$ m^2. A weak probe signal provided by a Nd^{3+} fiber laser (DFL), was coupled into the amplifier. The amplifier was 10 m of Nd^{3+} doped fiber. A piece of glass (AR) was glued onto the fiber end at an angle of 12° to avoid any cavity effect. A monochromator (MC) was used to filter the residual pump beam and the three level transition at 938 nm. The amplified signal was measured by synchronous detection. The amplifier and the DFL were pumped with a $TiAl_2O_3$ laser at 827 nm. The dichroic mirror (DM) was used to couple the amplified signal into the monochromator and to transmit all the pump signal.

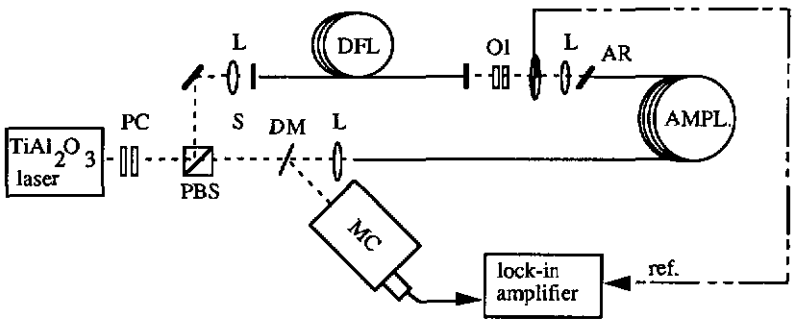

Fig. 2.3.2. Basic setup for the measurement of the small signal gain of the Nd^{3+} doped fiber. DFL: doped fiber laser, OI: optical isolator, L: coupling lenses, AR: angled faces, DM: dichroic mirror, T: tunable attenuator, MC: monochromator, AMPL.: doped fiber amplifier, PC: polarization controller, PBS : polarizing beam splitter.

The gain as a function of the absorbed pump power is shown in Fig. 2.3.3. A gain slope of 0.36 dB/mW of absorbed pump power has been measured.

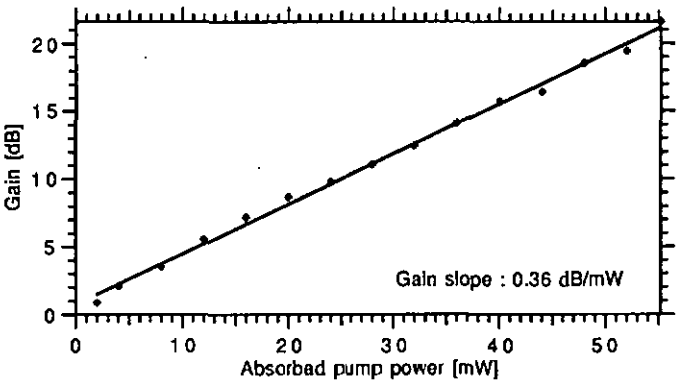

Fig. 2.3.3. Small signal gain of a 500 ppm Nd^{3+} doped fiber. The fiber characteristics are NA = 0.21, core radius a = 1.75 μm, fiber length L = 10 m. The pump wavelength was 832 nm.

The theoretical value for the gain efficiency, obtained from Eq. (2.25), by assuming a typical value of η_c = 66 %, is 0.71 dB/mW for a LP01 pump beam, and 0.41 dB/mW for a LP11 pump beam. This indicates that in this case the pump beam was mainly guided in the LP11 mode. The difference between the theoretical value of 0.41 dB/mW and the measured value of 0.32 dB/mW can be explained by the fact that the dopant distribution is not uniform in the fiber core, as it was assumed for the calculation of the value. Another explanation could be that the approximate solution for the small signal gain given by Eq. (2.25) is less accurate for the LP11 pump mode than for the LP01 mode [2.3]. Nevertheless this model is a powerful tool which gives all the basics information necessary for the optimization of active fiber devices.

2.4. Conclusions

A theoretical model for the gain of an active fiber, based on a four level system, has been derived in this section. This model includes the properties of the active medium, which are mainly determined by the absorption at the pump wavelength, the emission cross-section, and the fluorescence decay time. The interaction of the active medium with the guided wave is

analyzed by considering the overlapping of the signal and pump mode. A simple analytical expression for the unsaturated (small) signal gain has been derived. This model does not address the problem of the pump saturation and of the ground state depletion, which becomes only important for the analysis of the absolute power properties of fiber lasers. Nevertheless this simple model gives all the essential parameters for the optimization of active fiber devices. A software package has been developed to calculate the gain properties of an active fiber based on this model. The fiber is assumed to be single mode at the signal wavelength. The pump propagates in either the LP01 or the LP11 mode.

3. Overview of optical fiber sources and their properties

In this Section, the fundamental characteristics of some basic Nd^{3+} doped fiber sources, which are of interest for sensor applications, are discussed. The broad spectral width of the gain curve (typical FWHM spectral width of more than 40 nm for Nd^{3+}:SiO_2:GeO_2) is very promising either for low-coherence sources (mirrorless superfluorescent fiber lasers (SFL)) or for tunable fiber lasers. The essentially homogeneous broadening of the gain curve allows to achieve efficient laser emission even for very narrow-band (single frequency) lasers. The interaction between the birefringent fiber cavity and the laser field is a very promising domain of research for a large family of new active fiber devices as demonstrated for the first time by Kim [3.1]. Open cavity fiber lasers are also of a great interest for many applications, such as Q-switching or coherently coupled resonators.

3.1. Mirrorless superfluorescent fiber laser

A superfluorescent fiber laser (SFL) consists mainly of a piece of doped fiber which is activated by a pump beam. The induced spontaneous emission is amplified all along the propagation in the fiber. This results in a smooth broadband emission, given by the amplified spontaneous emission (ASE). Such a broadband spectrum is of a great interest for many sensor applications, where the coherent effects play a detrimental role in the efficiency of the device. This is especially the case for the all-fiber gyroscope and the problem of the coherent backscattering, which can be easily avoided by use of a SFL [3.2], [3.3]. The SFL is also of interest for sensors based on the so called white-light interferometry techniques [3.4]. Thermal stability of the emission spectrum of the SFL has been shown to be better than in the case of superluminescent semiconductor sources [3.5]; typical temperature sensitivity of 15 ppm/^{0}C for the emission spectrum have been reported, which is of great interest for many sensor applications. Figure 3.1.1 shows a Nd^{3+} doped SFL in a double pass configuration.

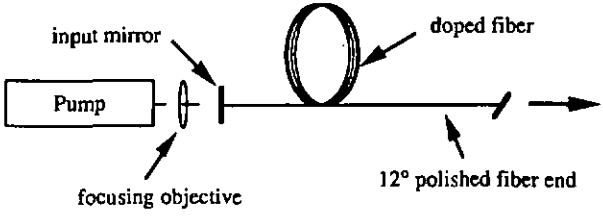

Fig. 3.1.1. Double pass Nd^{3+} doped superfluorescent fiber laser. An input mirror with R = 100 % at the fluorescence wavelength reflects the counter-propagating fluorescence to improve the efficiency of the SFL.

An input reflector (R = 100 % at 1088 nm) is used to reflect the counter-propagating fluorescence in the fiber to improve the efficiency of the device [3.6]. The power properties of a typical SFL are shown in Fig. 3.1.2. In our experiment, the source was 9 m of 500 ppm Nd^{3+} doped fiber with NA = 0.21 and a core radius of 1.75 μm. The pump was a $TiAl_2O_3$ laser at 824 nm. Typically more than 6 mW of superfluorescence were obtained for 140 mW of absorbed pump power. These pumping levels can be easily achieved with commercially available laser diodes, which makes the double pass SFL attractive for practical sensor applications. The efficiency of the SFL can be increased by an optimum design of the waveguide (optimization of the numerical aperture and of the core diameter) [2.3]. The output power spectrum is shown in Fig. 3.1.3 for different output powers.

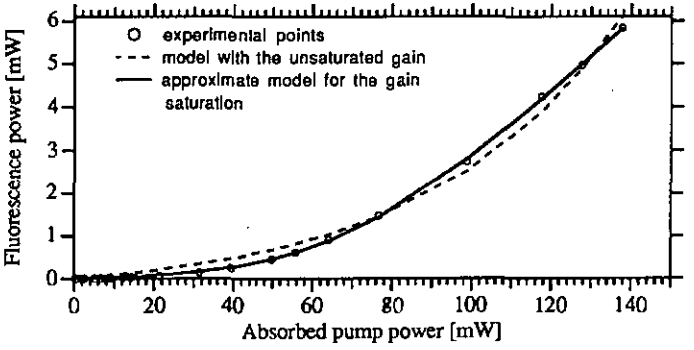

Fig. 3.1.2. Power characteristics of a double pass SFL. The pump wavelength was 824 nm, and the pump coupling efficiency was 60 %.

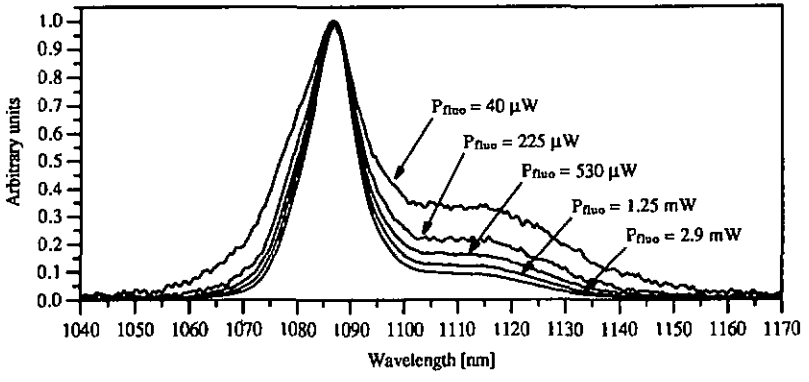

Fig. 3.1.3. Superfluorescence spectrum of a double pass SFL for different output powers, showing the power induced spectrol narrowing.

The spectrum has a smooth structure without any resonance. A narrowing of the spectral width can be observed for increasing output power, since the frequencies at the center of the gain curve are more amplified. Nevertheless, even for high output powers (more than 6 mW), the FWHM spectral width does not decrease below 10 nm, which is always broad enough for most of the common applications of SFLs.

A standard model for the power properties of the SFL [3.6] has been used to analyze the measured values which are shown in Fig. 3.1.2. This model assumes an unsaturated gain in the fiber and a rectangular distribution of the output spectrum. In this case, the output power is given by

$$P_{out} = P_0 \exp[2\,\Gamma_0(Pabs) - 1], \tag{3.1}$$

where P_0 is the energy of one photon which is contained in the emitted mode, namely

$$P_0 = m\, h\nu_s\, \Delta\nu_0, \tag{3.2}$$

where m is the number of polarizations, $h\nu_s$ is the energy of the emitted photon and $\Delta\nu_0$ is the FWHM spectral width of the fluorescence. Γ_0 is the unsaturated (small) gain coefficient, which is given by Eq. (2.25). The dashed line in Fig. 3.1.2 shows the best fit of Eq. (3.1) to the measured values (dots). This yields P_0 = 370 μW, and an unsaturated gain slope $G = \exp(\Gamma_0) = 0.043$ dB/mW. A typical value for P_0, which is obtained from Eq. (3.2) by assuming $\Delta\lambda = \lambda_s^2/c\ \Delta\nu_0$ = 40 nm, m = 2 and $\lambda_s = c/\nu_s$ = 1088 nm, is P_0 = 3.7 μW. Consequently, a large discrepancy appears between the theory and the measurements. This is mainly due to the assumption of the negligible gain saturation, which cannot be used for large NA fibers. This has been highlighted by considering a qualitative model for the output power of the SFL which includes a simple analysis of the gain saturation. This model is given by

$$P_{out} = P_0 \exp(2\,\Gamma_s(Pabs) - 1), \tag{3.3}$$

where Γ_s is now the saturated gain coefficient, approximated by

$$\Gamma_s = \Gamma_0 \frac{1}{1 + \frac{P_{out}}{P_{sat}}}, \tag{3.4}$$

where P_{sat} is the saturation power. The solid line in Fig. 3.1.2 shows the best fit of Eq. (3.3) to the measured values. This yields P_0 = 38 μW, P_{sat} = 12.8 mW, and the unsaturated gain slope $G = \exp(\Gamma_0) = 0.12$ dB/mW. In this case, the fitted curve gives a good description of the measured values, which indicates that the gain saturation is significant in our experiment. Nevertheless, the fitted values for G, P_0 and P_{sat} are still significantly different from the

theoretical values, which are G = 0.41 dB/mW (see p. 26), P_o = 3.7 μW (Eq. (3.2), with λ_s = 1088 nm, $\Delta\lambda$ = 40 nm) and P_{sat} = 2.7 mW (Eqs. (4.3.91) and (4.3.92), with NA = 0.21). This is obviously due to the fact that Eq. (3.3) is only a qualitative description of the power properties of the SFL. The effect of competition between the two transitions at λ_s = 1088 nm and λ_s = 928 nm is also believed to complicate the analysis of the power properties of the SFL.

3.2. Fiber lasers

Efficient coherent sources can be easily obtained by considering the setup as shown in Fig. 3.2.1 for a single-mode fiber laser (FL).The laser cavity is a few meters of Nd^{3+} doped fiber, and the resonator is composed of two mirrors fixed at both fiber ends. The pump beam is coupled into the fiber core through the input mirror. The reflectivity of the cavity mirrors are optimized to maximize the output power for a given cavity loss and pumping level. Since the intrinsic attenuation of the fiber at the signal wavelength is very low (typically 0.1 dB/m), the fabrication of ultra low loss cavities is possible, provided that the butt coupling of the mirrors is well controlled. This results in fiber lasers with very low pump threshold (typically less than 1 mW of absorbed pump power), and with a very high slope efficiency (up to 33 %, [3.7]).

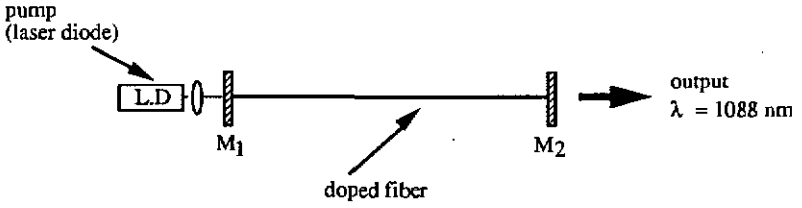

Fig. 3.2.1. Typical configuration of a single-mode fiber laser. The pump beam is provided by a laser diode. The laser cavity is a few meters of doped fiber.

The typical power curve of a fiber laser is shown in Fig. 3.2.2. The fiber in this experiment was 500 ppm Nd^{3+} doped, with a core diameter of 3.5 μm and NA = 0.21. The cavity length was 1.9 m. The reflectivities of the mirrors were M_1 = 100 % and M_2 = 96 % at the fluorescence wavelength (λ_p = 1088 nm). The two mirrors were glued onto the fiber ends. The fiber extremities were cleaved using a commercially available system (York FK10), which produces high quality cuts (typically less than 0.1° of uncertainty on the perpendicularity of the cut). The power spectrum of the laser is shown in Fig. 3.2.3. The structures of resonances in the spectrum are given by the input and output mirrors, which act as a Fabry-Perot etalons [3.8]. The thickness of the input and output mirrors were 170 μm and 1 mm, respectively.

These two Fabry-Perot resonators are responsible for the broad and narrow structure which can be seen in the spectrum. The slope efficiency and the pump threshold do strongly depend on the guiding properties of the fiber at the pump and at the laser wavelength, as extensively described in [2.1] and [2.9]. An optimization of the waveguide properties (numerical aperture and core radius) and of the transmission of the output mirror M_2 allows to improve the power characteristics of this laser [4.3].

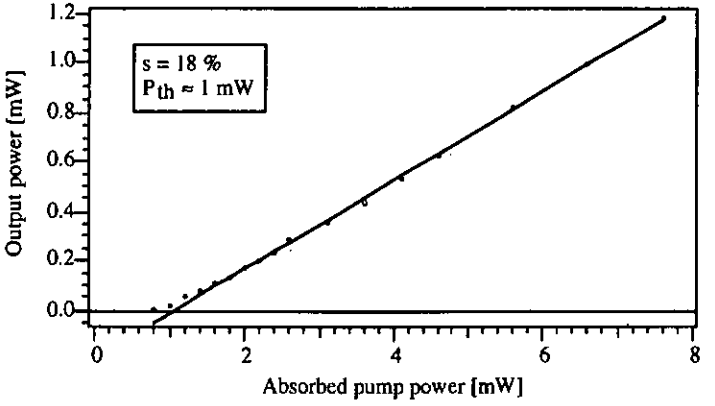

Fig. 3.2.2 Laser output at 1088 nm as a function of the absorbed pump power. The laser was 1.9 m of doped fiber with NA = 0.21 and core radius = 1.75 µm. The pump wavelength was 810 nm. The mirror reflectivities were M_1 = 100 %, M_2 = 96 % at the laser wavelength. A laser threshold of 0.75 mW and a slope efficiency of 18 % were measured.

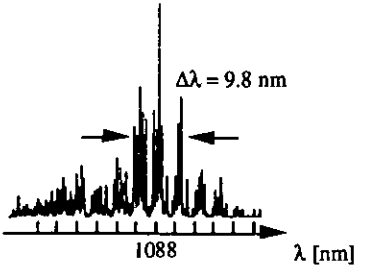

Fig. 3.2.3. Power spectrum of the fiber laser. The envelope of the spectrum has a spectral width of typically 10 nm. The structures are given by the input and output mirrors, which act as a Fabry-Perot etalons. The peak emission wavelength was 1088 nm.

The broad spectral emission of the FL can be easily reduced by intracavity filtering (e.g. with a grating engraved in the fiber core by UV illumination [3.9]), or by using a very narrow-band filter as a mirror. A well known technique [3.10] consists of replacing one of the mirrors by a grating, as shown in Fig. 3.2.4. The emission wavelength can then be easily tuned over a broad spectral range (typically $\Delta\lambda$ = 59 nm) by a small tilt of the grating. The emission spectrum of a tunable Nd^{3+} doped fiber laser is shown in Fig. 3.2.5. For this measurement, the laser was 1.9 m of 500 ppm Nd^{3+} doped fiber (NA = 0.21, 3.5 µm core diameter), pumped with a laser diode at 810 nm. The end mirror was a holographic grating blazed at 1 µm, used in the Littrow configuration. A fraction of the signal power was extracted by use of a pellicle beam-splitter (reflectivity 10 %). A typical spectral width of 0.16 nm has been measured. The laser threshold was at 12 mW of absorbed pump power. The operation of the open-cavity configuration, which results in high cavity losses (typical single pass loss > 25 %), is only possible because of the very high unsaturated gain (typically > 30 dB) available in standard Nd^{3+} doped fibers. The open cavity fiber laser allows to investigate a large number of promising devices such as Q-switched lasers, tunable lasers, or intracavity coupled fiber lasers [3.11]. The coherent coupling of fiber lasers will be discussed in Sect. 4.

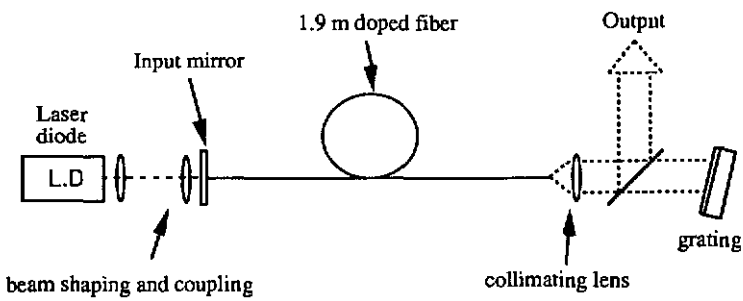

Fig. 3.2.4. Tunable Nd fiber laser. L.D is the pump laser diode at 810 nm. The characteristics of the fiber are NA = 0.21, dopant concentration 500 ppm, core diameter 3.5 µm. The end reflector is a 600 l/mm holographic grating blazed at 1 µm. The diffraction efficiency in the +1 diffraction order is 75 %.

The fiber length was 1.9 m which yields a longitudinal mode separation of $\delta\nu_F = c/(2nL) = 53$ MHz. The measured spectral width of 0.16 nm (Fig. 3.2.5) corresponds to $\delta\nu = c/\lambda^2\,\delta\lambda = 40.5$ GHz and to a coherence length of about 7.5 mm.

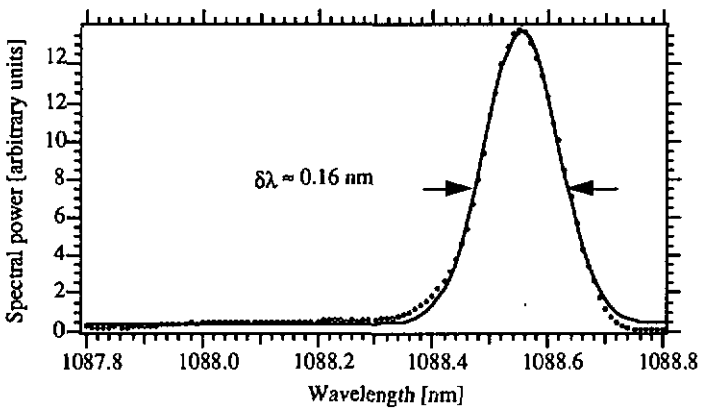

Fig. 3.2.5. Power spectrum of the tunable fiber laser. A spectral width of 0.16 nm was measured. The typical tuning range was 59 nm. The solid line is a Gaussian fit of the lineshape.

3.3. Conclusions

Two most important and well known applications of rare earth doped fibers have been experimented in this section. The principle of the amplification of the spontaneous emission (ASE) has been investigated for the fabrication of low coherence superfluorescent sources, which are of interest for a certain class of sensors, such as the all fiber gyroscope, where coherent back-scattering can be minimized by using sources having a low temporal coherence. Another domain of applications of the SFL is white-light interferometry. The power characteristics of a double pass SFL have been analyzed by use of a standard theoretical model which assumes an unsaturated gain in the SFL. A large discrepancy between the measured output powers and the model have been observed. The main reason lies in the approximation of unsaturated gains, which cannot be used with large NA fibers (NA = 0.21 in our case). Another explanation is that the competition between the two main transition at $\lambda_S = 938$ nm and $\lambda_S = 1088$ nm in Nd^{3+} complicates the modeling of the SFL. Two fiber lasers have been studied. For the first time to our knowledge the Fabry Perot effect of the cavity mirrors on the power spectrum of a fiber laser has been observed and explained [3.8], [1.3]. The narrowing of the power spectrum of a fiber laser by use of a selective mirror (diffraction grating) has been experimented. The open-cavity which is used for the fabrication of the tunable fiber laser is of a strong interest since it is the basic element for the fabrication of the coupled cavity fiber lasers, as discussed in Sect. 4.

4. Coherent coupling of single-mode fiber lasers

4.1. Motivation

The coherent coupling of lasers is of a strong interest for high power sources since this technique allows to increase the total emitted output power beyond the physical limitation of the individual emitters, achieving a high quality (diffraction limited) output beam. These coupled sources are very attractive for the realization of cheap and compact high power sources for telecommunications, for pumping of solid-state and fiber lasers, for material processing, for medical applications or for sensors. The most important requirement for the coherent addition is to achieve stable in-phase coupling between the individual emitters. Depending on the basic properties of these sources, different coupling techniques can be considered. A first category is concerned with inherently coupled laser arrays. In this case, the emitters are so close to each other that an intrinsic coupling through the evanescent waves is established, which fixes stable mutual phases between the elements of the array. This is the case for semiconductor laser diode arrays. For these sources an efficient coherent addition can be achieved by beam-shaping of the emitted supermode [4.1]. This coupling is schematically shown in Fig. 4.1.1.

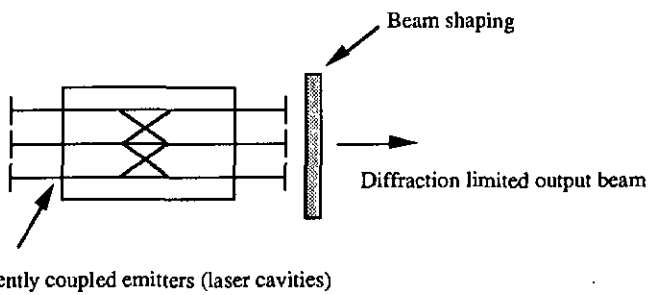

Fig. 4.1.1. Beam shaping for the coherent addition of inherently coupled emitters. The crossed lines symbolize the inherent coupling between the sources. The resulting supermode is converted into a single lobed diffraction limited output beam by use of a diffractive optical element.

The second category of sources is concerned with strictly independent emitters. In this situation, no stable mutual phases exist and a strong coupling between the cavities must be established to fix these mutual phases. This can be achieved by use of a coupling (fan-in) element added to a compound laser cavity, as shown in Fig. 4.1.2. The most important advantage of the intra-cavity coupling technique lies in the self adjustment of the mutual phases and amplitudes for the most efficient concentration of the output power into the diffraction

limited output beam. This coupling technique will be extensively discussed in the next section for the coherent addition of Nd^{3+} doped fiber lasers.

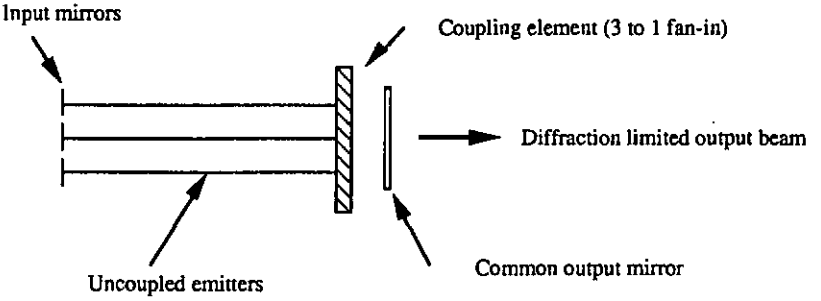

Fig. 4.1.2. Coherent addition of inherently uncoupled emitters. The fan-in element provides the coupling of the output beams into a single diffraction limited beam. The output mirror is common to all the emitters.

4.2. Basic principle

The basic scheme of an intracavity coupled fiber laser array is shown in Fig. 4.2.1 for three cavities. It consists of three fiber lasers which are longitudinally pumped through their individual input mirrors M.

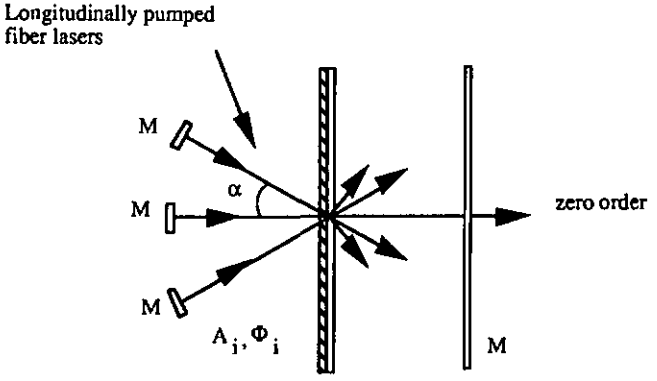

Fig. 4.2.1. Basic configuration for the coherent coupling of three single-mode fiber lasers. M are cavity mirrors, A_i, Φ_i are the amplitudes and phases of each laser, respectively.

The fan-in element is a phase grating whose purpose is to simultaneously provide the coupling between the laser cavities (beam splitting) and the beam shaping. This element combines the beams of each laser into a single beam with an efficiency which depends on the relative amplitudes and phases of these beams. The output of each fiber with amplitude A_i and phase Φ_i passes through the 3 to 1 fan-in element which combines the beams into a single diffraction order when the correct amplitudes and phases are established. The output mirror is thus common to all three lasers and provides optimum cavity feedback. For unmatched A_i and Φ_i, the output of the system consists of 5 diffraction orders, resulting in high cavity losses. The relative amplitudes and phases of the coupled lasers will be automatically adjusted in order to get minimum threshold for the system. The key element which defines the characteristics of the coupled laser is the fan-in plate. This element is essentially a phase grating (continuous surface relief grating) which is designed to give three diffraction orders of equal amplitudes $A_i = A_0$ when illuminated with a collimated beam (fan-out), as shown in Fig. 4.2.2.

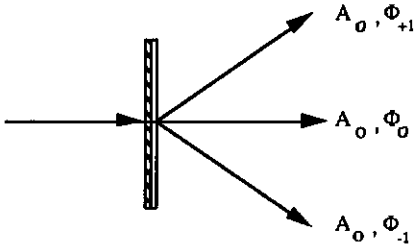

Fig. 4.2.2. The coupling element is designed to produce three output beams of equal amplitudes A_0 and with fixed mutual phases when illuminated with a collimated beam. The fixed mutual phases depend on the optimization process used for the fabrication of the phase grating.

The mutual phases between the three diffraction orders is fixed by the optimization process of the fan-in; this yields for example $\Phi_1 = 0$, $\Phi_2 = 0$, $\Phi_3 = \pi$, or $\Phi_1 = 0$, $\Phi_2 = \pi/2$, $\Phi_3 = 0$. In the coupled cavity laser, this fan-out is then played as a fan-in by illuminating it with the three beams of amplitudes A_i and phases Φ_i produced by the three fiber lasers. The efficiency (power in the zero order divided by the total output power) of the fan-in can be theoretically calculated for different A_i and Φ_i, by using the models described in [4.2]. In the ideal case ($A_i = A_0$, $\Phi_1 = 0$, $\phi_2 = 0$, $\phi_3 = \pi$), a maximum efficiency of 93.8 % is achieved for a losseless element. This is the best coherent coupling efficiency one can expect to get in the three coupled cavity lasers (Fig. 4.2.3 (left)).

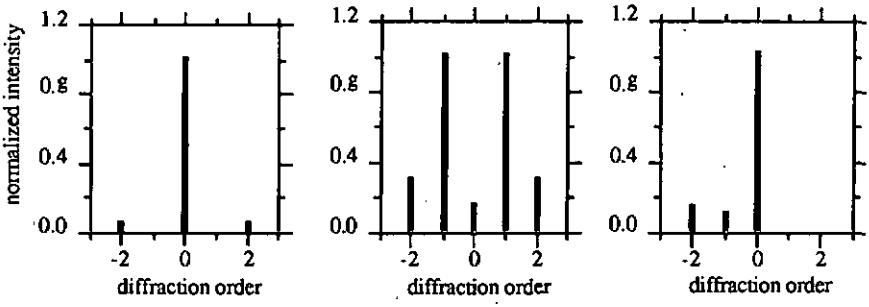

Fig. 4.2.3. Calculated distribution of the output power in the 5 diffraction orders of the fan-in element for different relative amplitudes and phases of the three laser beams. Left: optimal situation, with $A_i = A_0$ and $\Phi_1 = 0$, $\Phi_2 = 0$, $\Phi_3 = \pi$ the efficiency is 93.8 %. Center: for $A_i = A_0$ and $\Phi_1 = \pi$, $\Phi_2 = 0$, $\Phi_3 = 0$ the efficiency is 5.13 %. Right: for $\Phi_1 = 0$, $\Phi_2 = 0$, $\Phi_3 = \pi$ (ideal) and $A_1 = 2$, $A_2 = 1$, $A_3 = 1$ the efficiency is 80.3 %.

The efficiency decreases rapidly if the phases Φ_i or the amplitudes A_i do not match the ideal A_i and Φ_i. For example, a uniform illumination with the non-ideal phases $\phi_1 = \pi$, $\phi_2 = 0$, $\phi_3 = 0$ reduces the efficiency to 5.13 % (Fig. 4.2.3. (center)). A non-uniform illumination ($A_1 = 2$, $A_2 = 1$, $A_3 = 1$) with the ideal phases ($\Phi_1 = 0$, $\Phi_2 = 0$, $\Phi_3 = \pi$) gives an efficiency of only 80.3 % (Fig. 4.2.3 (right)). The main advantage of this coupling technique is the self adjustment of the mutual amplitudes and phases of all the individual emitters for the condition of minimum losses, which results in a very simple and efficient way to achieve a coherent addition of laser beams. We have demonstrated this intra-cavity coupling technique by considering the experimental setup which is described in Fig. 4.2.4 for three Nd^{3+} doped fiber lasers using the four level system at 1088 nm. Each emitter was a 2.91 m long fiber with NA = 0.21, fiber core radius = 1.75 µm and 500 ppm of Nd^{3+} concentration. Each laser had its own input mirror (R =100 % at λ = 1088 nm) and was longitudinally pumped with a high power laser diode (150 mW CW) at a wavelength around 810 nm. The bare fiber ends of the three cavities were fixed onto a triple V-groove anisotropically etched on a silicon wafer. The period between the fibers was (315.5 ±0.1) µm. This high accuracy on the periodicity is necessary to optimize the coupling efficiency of the fan-in element. The output beams coming out from the three fibers were collimated by use of a high quality (low aberrations) collimating triplet (Melles Griot 06 GLC 003) with f = 14.5 mm. The fan-in plate was placed at the Fourier plane of the lens. An output mirror (Reflectivity 96 % at λ = 1088 nm) was used for the optical feedback in the three cavities. Fiber loop polarization controllers (PC) were added on each laser

cavity to adjust the output polarization state in order to optimize the interference of the diffracted beams from the fan-in.

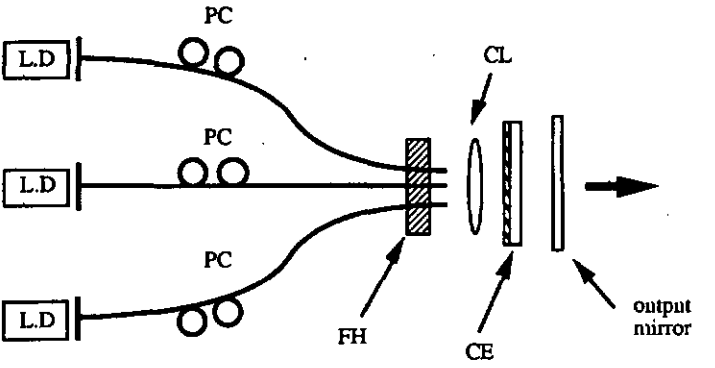

Fig. 4.2.4. Coupled cavity Nd^{3+} doped fiber lasers. A: input mirrors, M: output mirror, PC: polarization controllers, FH: fiber holder, CL: collimating lens, CE: fan-in plate. Each laser has its own input mirror and is longitudinally pumped with a high power laser diode at 810 nm. The output mirror provides the feedback in the three cavities.

A typical distribution of the laser output power measured in the five diffraction orders is shown in Fig. 4.2.5. A coupling efficiency of the total emitted power into the zero diffraction order of 77 % has been achieved.

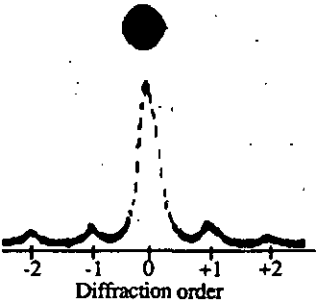

Fig. 4.2.5. Distribution of the power at the output of the coupled cavity fiber laser. 77 % of the total emitted power is concentrated in the zero diffraction order.

This coupling efficiency of 77 % compares favorably with the maximum efficiency of 93.8 % fixed by the best theoretical efficiency of the fan-in plate. The discrepancy between the theoretical and measured values depends on the cavity design, as will be discussed in Sect. 4.3.8.

4.3. Theoretical and experimental investigation of the intracavity coupled fiber laser

In this section the fundamental properties of the coupled cavity lasers are investigated by considering a linear description of the system. This yields a simple model allowing to explain the coupling between the individual emitters and to demonstrate the self adjustment of the mutual amplitudes and phases between the emitters which are necessary for an efficient coupling. The conditions for the laser threshold and for the steady state will be established by use of this model.

4.3.1. Linear analysis

A system of three coupled emitters will be considered as shown in Fig. 4.2.4. The basic concept consists of a linear modeling of each element of the coupled cavity laser. This can only be achieved by making some basic assumptions. First, the distribution of the optical power in each cavity is homogeneous, which is a good approximation if the spatial hole burning of the standing waves in the cavity is negligible. This is especially true if the emission spectrum of the lasers is broad enough to produce an averaging of a large number of longitudinal modes.

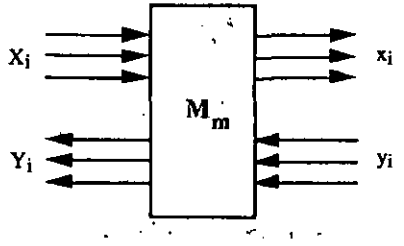

Fig. 4.3.1. Lineor description of the coupled cavity fiber lasers. Each constituting element is modeled by a 6 by 6 ports module which describes the transformations of the electrical fields propagating in both directions through the element. Each module is described by a 6 x 6 matrix M_m.

Second, the gain and the gain saturation in each fiber laser are assumed to be homogeneous. This is valid if a uniform longitudinal distribution of the pump and signal beams is assumed in each fiber.

Each component of the coupled lasers is now described by a 6 x 6 port element, as shown in Fig. 4.3.1. Each element is fully represented by a 6 x 6 matrix $\mathbf{M_m}$. The three channels propagating from left to right ($x_i \rightarrow X_i$) describe the electrical field of the individual i-th emitter and its transformation through the element. The three channels ($Y_i \rightarrow yi$) describe the same electrical field transformation for the beams propagating from right to left. The overall matrix of the coupled cavity lasers is then given by

$$S = \prod_m \mathbf{M_m}, \qquad (4.3.1)$$

where m is the number of the elements in the coupled cavity laser. The linear modules which constitute the coupled cavity laser are shown in Fig. 4.3.2. The matrix $\mathbf{M_{in}}$ describes the propagation through the input mirrors of the three cavities. The saturated gains in the three active fibers are represented by a matrix $\mathbf{M_G}$, the coupling element is modeled by a matrix $\mathbf{M_{FI}}$, and the output mirror by $\mathbf{M_{out}}$.

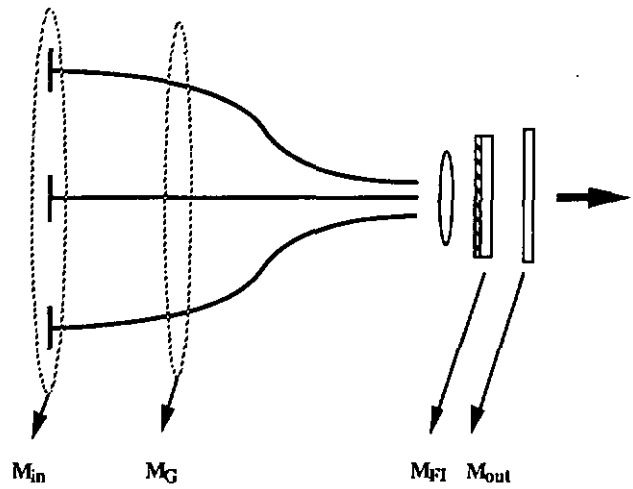

Fig. 4.3.2. Modeling of the elements constituting the coupled cavity fiber lasers. The matrices M_m describe the properties of each cavity element.

4.3.2. Matrices of the resonator elements

4.3.2.1 Input mirror

The matrix M_{in} describes the reflection and transmission of the laser beams on the input mirror for the three individual cavities. The propagation in both directions of the three beams through the input mirror is governed by Eqs. (4.3.2) and (4.3.3), which can be written by using the formalism stated in Fig. 4.3.1, namely

$$x_k = i\, t_1\, X_k + r_1\, y_k \tag{4.3.2}$$

$$Y_k = i\, t_1\, y_k + r_1\, X_k, \tag{4.3.3}$$

where $i = \sqrt{-1}$, r_1 and t_1 are the amplitude reflectivity and transmission of the mirror, respectively. The factor i has to be added in Eqs. (4.3.2) and (4.3.3) for energy conservation. No extra phase shift is considered for the reflection, since this can be included in the external optical path length. From Eqs. (4.3.3) and (4.3.2) one gets

$$x_k = \left(i\, t_1 - \frac{r_1^2}{t_1}\right) X_k + \frac{r_1}{i\, t_1}\, Y_k, \tag{4.3.4}$$

$$y_k = -\frac{r_1}{i\, t_1}\, X_k + \frac{1}{i\, t_1}\, Y_k. \tag{4.3.5}$$

The matrix M_{in} becomes then

$$M_{in} = \begin{pmatrix} i(t_1 + \frac{r_1^2}{t_1}) & 0 & 0 & -\frac{ir_1}{t_1} & 0 & 0 \\ 0 & i(t_1 + \frac{r_1^2}{t_1}) & 0 & 0 & -\frac{ir_1}{t_1} & 0 \\ 0 & 0 & i(t_1 + \frac{r_1^2}{t_1}) & 0 & 0 & -\frac{ir_1}{t_1} \\ \frac{ir_1}{t_1} & 0 & 0 & -\frac{i}{t_1} & 0 & 0 \\ 0 & \frac{ir_1}{t_1} & 0 & 0 & -\frac{i}{t_1} & 0 \\ 0 & 0 & \frac{ir_1}{t_1} & 0 & 0 & -\frac{i}{t_1} \end{pmatrix} \tag{4.3.6}$$

This matrix is not diagonal, since the mirrors produce a coupling between the input and output components for each cavity.

4.3.2.2 Gain medium

The gain is modeled by considering a saturated homogeneous amplitude gain g_i in each fiber. The propagation through a fiber of length L gives an accumulated phase $\phi_k = k\, n\, L$ in each cavity, where k is the wave number and n is the effective index of refraction of the signal mode. The amplification and the phase shift of the optical field which propagates in both directions is given by

$$x_k = g_k \exp(i\,\phi_k)\, X_k \tag{4.3.7}$$

$$y_k = \frac{1}{g_k} \exp(-i\,\phi_k)\, Y_k. \tag{4.3.8}$$

The diagonal matrix M_G for the gain becomes then

$$M_G = \begin{pmatrix} g_1 e^{i\phi_1} & 0 & 0 & 0 & 0 & 0 \\ 0 & g_2 e^{i\phi_2} & 0 & 0 & 0 & 0 \\ 0 & 0 & g_3 e^{i\phi_3} & 0 & 0 & 0 \\ 0 & 0 & 0 & \frac{1}{g_1} e^{-i\phi_1} & 0 & 0 \\ 0 & 0 & 0 & 0 & \frac{1}{g_2} e^{-i\phi_2} & 0 \\ 0 & 0 & 0 & 0 & 0 & \frac{1}{g_3} e^{-i\phi_3} \end{pmatrix}. \tag{4.3.9}$$

As mentioned in Sect. 4.3.1, this description of the gain medium is only valid if the assumptions of uniform distribution of the signal and pump wave in each fiber are fulfilled. Nevertheless, this model allows a complete modeling of the coupling principle between the emitters without any loss of generality even if these requirements are not perfectly satisfied. The only drawback will be a less accurate description of the absolute power characteristics of the coupled lasers, especially in the case of single frequency lasers where spatial hole burning becomes important.

4.3.2.3 Coupling element (fan-in)

The coupling element which combines the signals provided by the three individual emitters into the single output beam is a continuous surface relief grating (fan-in). This fan-in is essentially a phase grating whose phase profile is shown in Fig. 4.3.3. The optimization and fabrication processes of these elements are extensively described in [4.2].

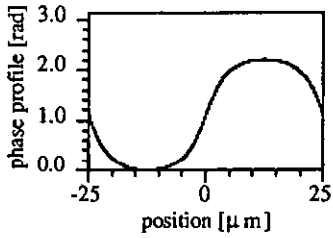

Fig. 4.3.3. Typical phase profile of a 3 to 1 fan-in cantinuous surface relief phase grating. In this case, the period of the profile is 50 μm.

The linear matrix modeling of the 3 to 1 fan-in element is obtained by using the technique which is shown in Fig. 4.3.4. The fan-in is considered as a fan-out which is successively illuminated by an individual collimated beam launched in one of the three diffraction orders (–1, 0, +1). For each illumination the fan-out produces three diffraction orders with amplitude distribution ratios A_{sp} and with mutual phases Φ_{sp} given by the properties of the phase grating. The coupling (fan-in) is then obtained by considering the superposition of the three diffraction orders produced by the three individual illuminations; this results in five output diffraction orders as shown in Fig. 4.2.1. For perfectly matched amplitudes and mutual phases of the three illuminating beams, all the power will be concentrated in the zero diffraction order. The phase Φ_k are a function of the optimization process which was used for the design of the continuous surface relief grating. For a 3 to 1 fan-in, the typical values for Φ_k are $\Phi_1 = 0$, $\Phi_2 = \pi/2$, $\Phi_3 = 0$), or $\Phi_1 = 0$, $\Phi_2 = 0$, $\Phi_3 = \pi$.

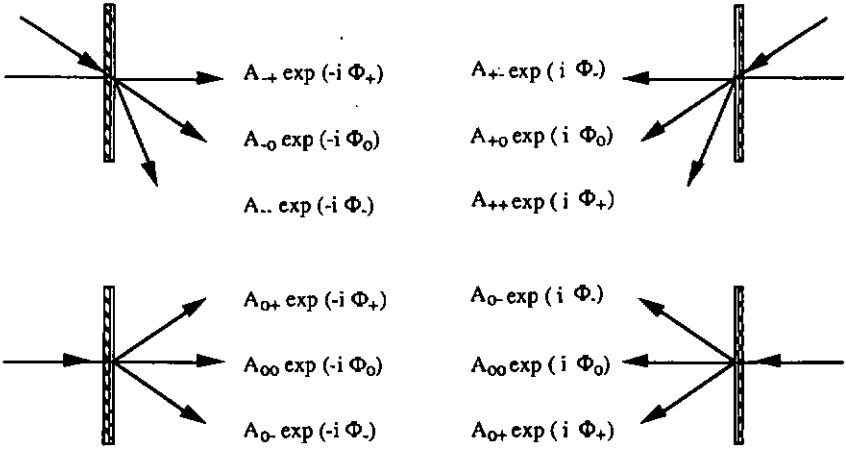

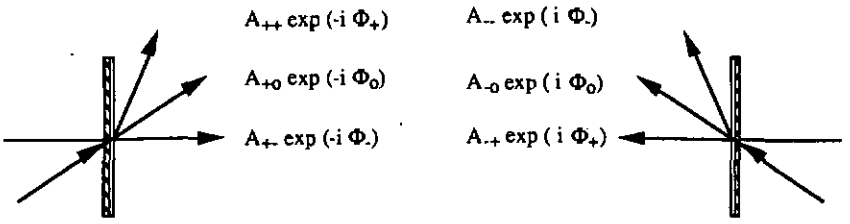

Fig. 4.3.4. Amplitudes and mutual phases of the diffracted beams when the fan-in is illuminated with a single collimated beam in one of the diffraction orders. The fan-in is obtained by the superposition of the diffraction orders obtained from the individual illuminations in the three diffraction orders (+1), (0) and (–1).

The matrix $\mathbf{M_{FI}}$ is obtained by considering the structure as shown in Fig. 4.3.5. The inputs and outputs on the left side of the module correspond to the inputs and outputs of the three emitters. The channels on the right side are the first three diffraction orders of the fan-in element, considered in both directions.

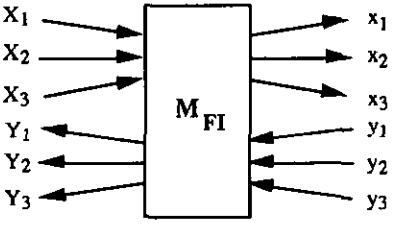

Fig. 4.3.5. Modeling of the fan-in element. The channels on the left side correspond to the inputs and the outputs of the fiber lasers. The channels on the right side are the first three diffraction orders of the fan-in, in both directions.

The three diffraction orders x_i are calculated by considering the superposition of the sets of three diffraction orders given by each incident amplitude X_i, which yields

$$x_1 = A_{0+} \exp(-i\,\Phi_+)\, X_2 + A_{+0} \exp(-i\,\Phi_0)\, X_3 \qquad (4.3.10)$$

$$x_2 = A_{00} \exp(-i\,\Phi_0)\, X_2 + A_{-+} \exp(-i\,\Phi_+)\, X_1 + A_{+-} \exp(-i\,\Phi_-)\, X_3 \qquad (4.3.11)$$

$$x_3 = A_{0-} \exp(-i\,\Phi_-)\, X_2 + A_{-0} \exp(-i\,\Phi_0)\, X_1. \qquad (4.3.12)$$

The same operation is performed for the three diffraction orders Y_i obtained from the superposition of the y_i, namely

$$Y_1 = A_{0-} \exp(i\,\Phi_-)\, y_2 + A_{-0} \exp(i\,\Phi_0)\, y_3 \qquad (4.3.13)$$

$$Y_2 = A_{00} \exp(i\,\Phi_0)\, y_2 + A_{+-} \exp(i\,\Phi_-)\, y_1 + A_{-+} \exp(i\,\Phi_+)\, y_3 \qquad (4.3.14)$$

$$Y_3 = A_{0+} \exp(i\,\Phi_+)\, y_2 + A_{+0} \exp(i\,\Phi_0)\, y_1 \qquad (4.3.15)$$

Equations (4.3.13) to (4.3.15) can be rearranged to express the y_i as a function of the Y_i, which give

$$y_1 = \frac{A_{-+}\, A_{0+}}{A_{-0}\, A_{+0}\, D} \exp(2i\,(\Phi_+ - \Phi_0))\, Y_1$$

$$- \frac{A_{0+}}{A_{+0}\, D} \exp(i\,(\Phi_+ - \Phi_0))\, Y_2$$

$$+ \left(\frac{\exp(-i\,\Phi_0)}{A_{+0}} + \frac{A_{+-}\, A_{0+}}{A_{+0}^2\, D} \exp(i(\Phi_+ + \Phi_- - 2\,\Phi_0)) \right) Y_3, \qquad (4.3.16)$$

$$y_2 = \frac{1}{D} \left(- \frac{A_{-+}}{A_{-0}} \exp(i(\Phi_+ - \Phi_0))\, Y_1 + Y_2 - \frac{A_{+-}}{A_{+0}} \exp(i(\Phi_- - \Phi_0))\, Y_3 \right) \qquad (4.3.17)$$

$$y_3 = \left(\frac{\exp(-i\,\Phi_0)}{A_{-0}} + \frac{A_{-+}\, A_{0-}}{A_{-0}^2\, D} \exp(i(\Phi_+ + \Phi_- - 2\,\Phi_0)) \right) Y_1$$

$$- \frac{A_{0-}}{A_{-0}\, D} \exp(i(\Phi_- - \Phi_0))\, Y_2$$

$$+ \frac{A_{0-}\, A_{+-}}{A_{-0}\, A_{+0}\, D} \exp(2i\,(\Phi_- - \Phi_0))\, Y_3\,, \qquad (4.3.18)$$

with

$$D = A_{00} \exp(i\,\Phi_0) - \frac{A_{+-}\, A_{0+}}{A_{+0}} \exp i(\Phi_- - \Phi_0 + \Phi_+) - \frac{A_{-+}\, A_{0-}}{A_{-0}} \exp i(\Phi_+ - \Phi_0 + \Phi_-).$$

The matrix M_{FI} becomes then

$$\mathbf{M_{FI}} = \begin{pmatrix} 0 & m_{12} & m_{13} & 0 & 0 & 0 \\ m_{21} & m_{22} & m_{23} & 0 & 0 & 0 \\ m_{31} & m_{32} & 0 & 0 & 0 & 0 \\ 0 & 0 & 0 & m_{44} & m_{45} & m_{46} \\ 0 & 0 & 0 & m_{54} & m_{55} & m_{56} \\ 0 & 0 & 0 & m_{64} & m_{65} & m_{66} \end{pmatrix}, \qquad (4.3.19)$$

with the non zero m_{jk} listed in Tab. 1.

$$m_{12} = A_{0+} \exp(-i\,\Phi_+), \qquad m_{13} = A_{+0} \exp(-i\,\Phi_0), \qquad m_{21} = A_{-+} \exp(-i\,\Phi_+),$$

$$m_{22} = A_{00} \exp(-i\,\Phi_0), \qquad m_{23} = A_{+-} \exp(-i\,\Phi_-), \qquad m_{31} = A_{-0} \exp(-i\,\Phi_0),$$

$$m_{32} = A_{0-} \exp(-i\,\Phi_-),$$

$$m_{44} = \frac{A_{-+}\,A_{0+}}{A_{-0}\,A_{+0}\,D} \exp(2i\,(\Phi_+ - \Phi_0)), \qquad m_{45} = -\frac{A_{0+}}{A_{+0}\,D} \exp(i\,(\Phi_+ - \Phi_0)),$$

$$m_{46} = \frac{\exp(-i\,\Phi_0)}{A_{+0}} + \frac{A_{+-}\,A_{0+}}{A_{+0}^2\,D} \exp(i(\Phi_+ + \Phi_- - 2\,\Phi_0)),$$

$$m_{54} = -\frac{A_{-+}}{D\,A_{-0}} \exp(i(\Phi_+ - \Phi_0)), \qquad m_{55} = \frac{1}{D},$$

$$m_{56} = -\frac{A_{+-}}{D\,A_{+0}} \exp(i(\Phi_- - \Phi_0))$$

$$m_{64} = \frac{\exp(-i\,\Phi_0)}{A_{-0}} + \frac{A_{-+}\,A_{0-}}{A_{-0}^2\,D} \exp(i(\Phi_+ + \Phi_- - 2\,\Phi_0)),$$

$$m_{65} = -\frac{A_{0-}}{A_{-0}\,D} \exp(i(\Phi_- - \Phi_0)), \qquad m_{66} = \frac{A_{0-}\,A_{+-}}{A_{-0}\,A_{+0}\,D} \exp(2i\,(\Phi_- - \Phi_0)).$$

Tab. 1. Non zero m_{jk} of the matrix M_{FI}.

This model considers that only three diffraction orders are generated by each illuminaring beam, and that the resulting output beams are given by the superposition of the three sets of diffraction orders. This is only an approximation since many higher diffraction orders are involved in a real case. This can be easily understood by considering the diffraction orders +2 and –2 at the output of the fan-in which cannot be minimized by considering this model, since they are only produced by a single contribution of the two lateral emitters and that no interferences can be used to cancel these diffraction orders. Nevertheless this limitation of the model is not critical, since only the first three diffraction orders (+1, 0, –1) are of interest in our application. A careful adjustment of the amplitude distribution ratios A_{ij} in the diffraction orders allows to consider any power distribution and any intrinsic absorption in the material which constitutes the fan-in. As an example $A_{ij} = 1/\sqrt{3}$ gives a losseless element with a uniform power distribution in the three diffraction orders when illuminated with a collimated beam. Under these conditions, 100 % of the total incident power which is launched in the three input beams of the fan-in is diffracted in the three output diffraction orders. The power distribution ratios are then a function of the distribution of the incident mutual amplitudes and phases.

4.3.2.4 Output mirror

The only beam which is transmitted and reflected is the zero diffraction order, which is then responsible for the cavity feedback. The higher diffraction orders +1 and –1 provided by the fan-in element yield cavity losses, as shown in Fig. 4.2.1. The propagation of the beams in both directions is given by

$$x_1 = i\,t_2\,X_1, \tag{4.3.20}$$
$$x_2 = i\,t_2\,X_2 + r_2\,y_2, \tag{4.3.21}$$
$$x_3 = i\,t_2\,X_3, \tag{4.3.22}$$

$$Y_1 = i\,t_2\,y_1, \tag{4.3.23}$$
$$Y_2 = i\,t_2\,y_2 + r_2\,X_2, \tag{4.3.24}$$
$$Y_3 = i\,t_2\,y_3, \tag{4.3.25}$$

where r_2 and t_2 are the amplitude reflectivity and transmission of the mirror respectively. Equations (4.3.20) and (4.3.23) to (4.3.25) can be rearranged in the form

$$x_2 = i\,X_2\,(t_2 + \frac{r_2^2}{t_2}) - \frac{i\,r_2}{t_2}\,Y_2 \tag{4.3.26}$$

$$y_1 = -\frac{i}{t_2}\,Y_1 \tag{4.3.27}$$

$$y_2 = -\frac{i}{t_2}\,(Y_2 - r_2\,X_2) \tag{4.3.28}$$

$$y_3 = -\frac{i}{t_2}\,Y_3 \tag{4.3.29}$$

The matrix M_{out} of the output mirror becomes then

$$M_{out} = \begin{pmatrix} it_2 & 0 & 0 & 0 & 0 & 0 \\ 0 & i(t_2 + \frac{r_2^2}{t_2}) & 0 & 0 & -\frac{ir_2}{t_2} & 0 \\ 0 & 0 & it_2 & 0 & 0 & 0 \\ 0 & 0 & 0 & -\frac{i}{t_2} & 0 & 0 \\ 0 & \frac{ir_2}{t_2} & 0 & 0 & -\frac{i}{t_2} & 0 \\ 0 & 0 & 0 & 0 & 0 & -\frac{i}{t_2} \end{pmatrix}. \tag{4.3.30}$$

4.3.2.5 Matrix of the coupled cavity fiber lasers

The resultant matrix S of the coupled lasers is given by Eq. 4.3.1, namely

$$S = M_{out} \cdot M_{FI} \cdot M_G \cdot M_{in}. \tag{4.3.31}$$

The 36 components S_{ik} of the matrix S are lengthy expressions. For the sake of clarity, only the most important components which are necessary for the modeling of the coupled lasers are shown in the table below. The detailed expression of S is given in Annex A.1.

$$S_{15} = \frac{m_{12}\, t_2\, r_1\, g_2}{t_1} \exp\, i\,\phi_2, \qquad S_{16} = \frac{m_{13}\, t_2\, r_1\, g_3}{t_1} \exp\, i\,\phi_3,$$

$$S_{24} = \frac{m_{21}\, r_1\, g_1}{t_1\, t_2}(t_2^2 + r_2^2) \exp\, i\,\phi_1 - \frac{m_{54}\, r_2}{g_1\, t_1\, t_2} \exp\, -i\,\phi_1,$$

$$S_{25} = \frac{m_{22}\, r_1\, g_2}{t_1\, t_2}(t_2^2 + r_2^2) \exp\, i\,\phi_2 - \frac{m_{55}\, r_2}{g_2\, t_1\, t_2} \exp\, -i\,\phi_2,$$

$$S_{26} = \frac{m_{23}\, r_1\, g_3}{t_1\, t_2}(t_2^2 + r_2^2) \exp\, i\,\phi_3 - \frac{m_{56}\, r_2}{g_3\, t_1\, t_2} \exp\, -i\,\phi_3,$$

$$S_{34} = \frac{m_{31}\, t_2\, r_1\, g_1}{t_1} \exp\, i\,\phi_1, \qquad S_{35} = \frac{m_{32}\, t_2\, r_1\, g_2}{t_1} \exp\, i\,\phi_2$$

$$S_{44} = -\frac{m_{44}}{g_1\, t_1\, t_2} \exp\, -i\,\phi_1, \qquad S_{45} = -\frac{m_{45}}{g_2\, t_1\, t_2} \exp\, -i\,\phi_2,$$

$$S_{46} = -\frac{m_{46}}{g_3\, t_1\, t_2} \exp\, -i\,\phi_3,$$

$$S_{54} = \frac{m_{21}\, r_1\, r_2\, g_1}{t_1\, t_2} \exp\, i\,\phi_1 - \frac{m_{54}}{g_1\, t_1\, t_2} \exp\, -i\,\phi_1,$$

$$S_{55} = \frac{m_{22}\, r_1\, r_2\, g_2}{t_1\, t_2} \exp\, i\,\phi_2 - \frac{m_{55}}{g_2\, t_1\, t_2} \exp\, -i\,\phi_2,$$

$$S_{56} = \frac{m_{23}\, r_1\, r_2\, g_3}{t_1\, t_2} \exp\, i\,\phi_3 - \frac{m_{56}}{g_3\, t_1\, t_2} \exp\, -i\,\phi_3,$$

$$S_{64} = -\frac{m_{64}}{g_1\, t_1\, t_2} \exp\, -i\,\phi_1, \qquad S_{65} = -\frac{m_{65}}{g_2\, t_1\, t_2} \exp\, -i\,\phi_2,$$

$$S_{66} = -\frac{m_{66}}{g_3\, t_1\, t_2} \exp\, -i\,\phi_3.$$

Tab. 2. Components S_{ik} of the matrix S of the coupled lasers.

4.3.3. Conditions for the laser threshold

The condition for the laser threshold is established by assuming a non zero output power of the system for zero input signals. This situation is depicted in Fig. 4.3.6.

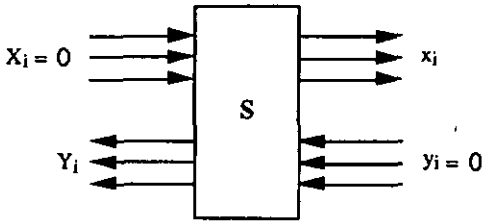

Fig. 4.3.6. The conditions for the laser threshold is given by $x_i \neq 0$ and $Y_i \neq 0$ for $X_i = 0$ and $y_i = 0$.

This condition can be expressed as a function of the matrix S of the couple lasers, namely

$$\begin{pmatrix} x_1 \\ x_2 \\ x_3 \\ 0 \\ 0 \\ 0 \end{pmatrix} = S \cdot \begin{pmatrix} 0 \\ 0 \\ 0 \\ Y_1 \\ Y_2 \\ Y_3 \end{pmatrix} \qquad (4.3.32)$$

The first three equations

$$x_k = S_{ki}\, Y_i, \quad k = 1, 2, 3 \text{ and } i = 4, 5, 6, \qquad (4.3.33)$$

connect the output signals on both laser extremities. The other set of three equations, given by

$$S_{ki}\, Y_i = 0, \quad k = 4, 5, 6 \text{ and } i = 4, 5, 6, \qquad (4.3.34)$$

gives the conditions for the laser threshold. Equation (4.3.34) can be written in a more convenient way by defining a new 3 by 3 matrix A with components $a_{nm} = S_{ik}$, for i = 4, 5, 6 and k = 4, 5, 6. This yields

$$A \cdot \begin{pmatrix} Y_1 \\ Y_2 \\ Y_3 \end{pmatrix} = \vec{0} \qquad (4.3.35)$$

Equation (4.3.35) has a non trivial solution (other than $Y_i = 0$, $\forall i$) only if the determinant of A, det(A), is equal to zero. This condition can be written as a function of the matrix components S_{ik}, namely

$$\det(A) = C_1 \exp -i(\phi_1 + \phi_2 + \Phi_3) + C_2 \exp i(-\phi_1 - \phi_2 + \Phi_3) + C_3 \exp i(\phi_1 - \phi_2 - \Phi_3) + C_4 \exp -i(\phi_1 - \phi_2 + \Phi_3) = 0. \qquad (4.3.36)$$

The C_i are complex constants for a given fan-in element, namely

$$C_1 = - m_{64}\, m_{45}\, m_{56} - m_{44}\, m_{55}\, m_{66} + m_{45}\, m_{54}\, m_{66} + m_{44}\, m_{56}\, m_{65} + m_{46}\, m_{55}\, m_{64} - m_{46}\, m_{54}\, m_{65},$$

$$C_2 = - r_1\, r_2\, m_{23}\, g_3^2\, (m_{44}\, m_{65} - m_{45}\, m_{64}),$$

$$C_3 = - r_1\, r_2\, m_{21}\, g_1^2\, (m_{45}\, m_{66} - m_{46}\, m_{65}),$$

$$C_4 = - r_1\, r_2\, m_{22}\, g_2^2\, (m_{44}\, m_{66} - m_{64}\, m_{46}).$$

Figure 4.3.7 shows the evolution of det(A) when the two lateral cavities have fixed gains $g_1 = 1$, $g_3 = 1$ and phases $\phi_1 = 0$, $\phi_3 = 0$. The gain g_2 and the phase ϕ_2 of the center cavity are variables. The fan-in is assumed to be losseless and symmetrical ($A_{sp} = 1/\sqrt{3}$).

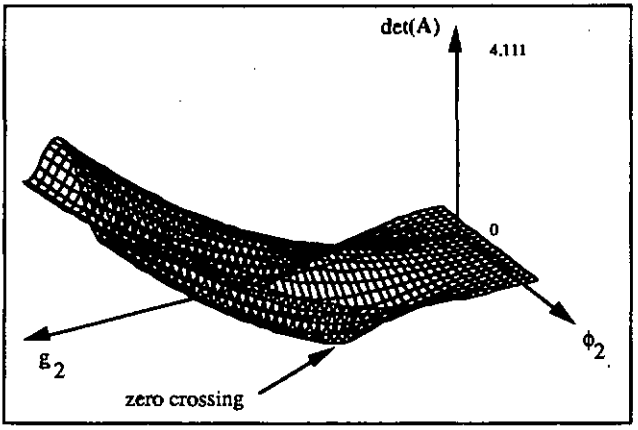

Fig. 4.3.7. Determinant of the matrix A as a function of the saturated gain g_2 and phase ϕ_2 in the central cavity for $g_1 = g_3 = 1$ and $\phi_1 = \Phi_3 = 0$. The saturated gain g_2 varies between 0 and 2.5, and the phase ϕ_2 varies between 0 and 4 rad. We find det (A) = 0 for $g_2 = 1.046$ and $\Phi_2 = m\,\pi$ ($m = 0, 1, \ldots$).

A zero crossing of det(A) is obtained for $g_2 = 1.046$ and $\phi_2 = \pi$. This gain compensates the cavity losses and allows to reach the laser threshold. An analysis of Eq. (4.3.36) shows that a solution can be found only when the accumulated phases in each cavity satisfy the conditions

$$\phi_i = m_i \pi, \qquad (4.3.37)$$

where m_i is an integer ($m_i = 0, 1, ...$). This unique set of mutual phases ϕ_i for the laser threshold corresponds also to the phases which are required for minimum cavity losses, as will be shown later by considering the eigen-solutions of the open-cavity coupled lasers. Under the assumption of matched mutual phases, as requested by Eq. (4.3.37), and by considering a typical symmetrical fan-in element with $A_{sp} = A$, $\Phi_+ = 0$, $\Phi_0 = \pi/2$, $\Phi_- = 0$, the condition for the laser threshold given by Eq. (4.3.36) can be written in a simpler way by replacing the m_{ik} given in Tab. 1. This yields

$$\sum_i g_i 2 = \frac{1}{A^2 r_1 r_2} . \qquad (4.3.38)$$

The laser threshold is reached when the sum of the saturated power gains g_i^2 compensates the losses introduced by the laser mirrors and by the power splitting ratio A^2 of the fan-in. Consequently, an infinite number of combinations for the saturated gains exist to satisfy the threshold condition. It is important to emphasize that Eqs (4.3.37) and (4.3.38) determine only the conditions for the threshold, but do not give any information on the steady state of the coupled lasers. The steady state is only one particular solution of Eq. (4.3.38), selected automatically by the coupled cavity laser to achieve minimum cavity losses. The parameters which are required for minimum intracavity losses can be calculated by considering the eigen-solutions of the open cavity coupled fiber lasers, as shown in Fig. 4.3.8.

4.3.4. Eigenstates of the coupled cavity lasers

4.3.4.1 Principle

The eigenstates of the coupled cavity lasers are studied by considering an open configuration as shown in Fig. 4.3.8. We assume a system where the input mirrors are removed and the backward signal Y_i is calculated as a function of the forward signal X_i for zero external signals, namely $y_i = 0$. The family of all the eigenstates $Y_i = \lambda X_i$ which can be calculated includes the more restrictive sets of eigen-solutions for the laser threshold and for the steady state

oscillation. This analysis allows to show that the phases for the laser threshold, which are given by Eq. (4.3.37), correspond to a configuration with the lowest intracavity losses and are the phases which are required for the steady state. The optimum set of saturated gains and optical power for the lowest losses will also be derived.

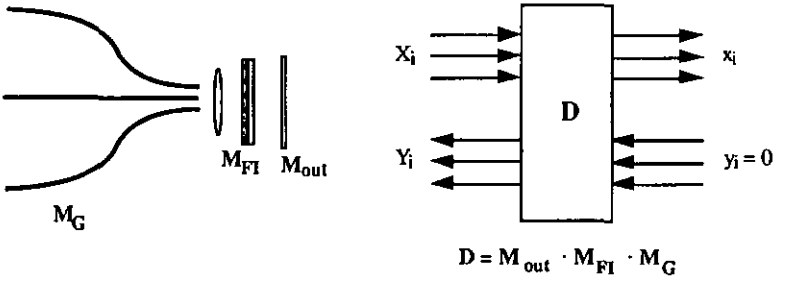

Fig. 4.3.8. Basic system for the analysis of the eigen-solutions $Y_i = \lambda X_i$ of the open cavity coupled fiber laser.

The matrix of the system is given by $D = d_{ik} = M_{out} \cdot M_{FI} \cdot M_G$ and it is of the form

$$D = \begin{pmatrix} 0 & d_{12} & d_{13} & 0 & 0 & 0 \\ d_{21} & d_{22} & d_{25} & d_{24} & d_{25} & d_{26} \\ d_{31} & d_{32} & 0 & 0 & 0 & 0 \\ 0 & 0 & 0 & d_{44} & d_{45} & d_{46} \\ d_{51} & d_{52} & d_{53} & d_{54} & d_{55} & d_{56} \\ 0 & 0 & 0 & d_{64} & d_{65} & d_{66} \end{pmatrix} \qquad (4.3.39)$$

The entire list of the elements d_{ik} is given in details in Annex A.2. Only the elements which are relevant for our study are reported in the table below.

$d_{44} = -i\frac{m_{44}}{g_1 t_2}\exp -i\phi_1$,	$d_{45} = -i\frac{m_{45}}{g_2 t_2}\exp -i\phi_2$,	$d_{46} = -i\frac{m_{46}}{g_3 t_2}\exp -i\phi_3$,
$d_{51} = i\frac{m_{21} r_2 g_1}{t_2}\exp i\phi_1$,	$d_{52} = i\frac{m_{22} r_2 g_2}{t_2}\exp i\phi_2$,	$d_{53} = i\frac{m_{23} r_2 g_3}{t_2}\exp i\phi_3$,
$d_{54} = -i\frac{m_{54}}{g_1 t_2}\exp -i\phi_1$,	$d_{55} = -i\frac{m_{55}}{g_2 t_2}\exp -i\phi_2$,	$d_{56} = -i\frac{m_{56}}{g_3 t_2}\exp -i\phi_3$,
$d_{64} = -i\frac{m_{64}}{g_1 t_2}\exp -i\phi_1$,	$d_{65} = -i\frac{m_{65}}{g_2 t_2}\exp -i\phi_2$,	$d_{66} = -i\frac{m_{66}}{g_3 t_2}\exp -i\phi_3$.

Tab. 3. Components d_{ik} of the matrix D of the open-cavity coupled fiber laser.

The x_i and y_i can be expressed as a function of the X_i and Y_i, namely

$$\begin{pmatrix} x_1 \\ x_2 \\ x_3 \\ 0 \\ 0 \\ 0 \end{pmatrix} = \mathbf{D} \cdot \begin{pmatrix} X_1 \\ X_2 \\ X_3 \\ Y_1 \\ Y_2 \\ Y_3 \end{pmatrix}. \tag{4.3.40}$$

By solving this system of linear equations and by rearranging the resulting expressions, one gets for the outputs Y_i as a function of the inputs X_i

$$Y_1 = - Y_3 \; C, \tag{4.3.41}$$

$$Y_2 = H \; Y_3, \tag{4.3.42}$$

$$Y_3 = -\frac{1}{F} \; (d_{51} \; X_1 + d_{52} \; X_2 + d_{53} \; X_3), \tag{4.3.43}$$

where

$$H = \frac{\left(\frac{d_{66}}{d_{64}} - \frac{d_{46}}{d_{44}}\right)}{\left(\frac{d_{45}}{d_{44}} - \frac{d_{65}}{d_{64}}\right)}, \tag{4.3.44}$$

$$F = H\left(d_{55} - \frac{d_{54} \; d_{45}}{d_{44}}\right) + d_{56} - \frac{d_{54} \; d_{46}}{d_{44}}, \tag{4.3.45}$$

and

$$C = \frac{1}{d_{44}} \; (H \; d_{45} + d_{46}). \tag{4.3.46}$$

Equations (4.3.41) to (4.3.45) can be written in a matrix form, namely

$$\vec{Y} = \mathbf{E} \cdot \vec{X} = \frac{1}{F} \begin{pmatrix} d_{51}C & d_{52}C & d_{53}C \\ -d_{51}H & d_{52}H & d_{53}H \\ -d_{51} & -d_{52} & -d_{52} \end{pmatrix} \cdot \vec{X}. \tag{4.3.47}$$

The eigenvalues and eigenvectors are obtained by solving the equation

$$\det(\mathbf{E} - \lambda \mathbf{I}) = 0, \tag{4.3.48}$$

where $\mathbf{I}$ is the identity matrix. This yields

$$\frac{-\lambda^2}{F}\left(-d_{51}\,C + d_{52}\,H + d_{53} + \lambda F\right) = 0. \qquad (4.3.49)$$

Equation (4.3.49) has only one non trivial solution which is given by

$$\lambda = \frac{1}{F}\left(d_{51}\,C - d_{52}\,H - d_{53}\right). \qquad (4.3.50)$$

For each λ the corresponding eigenvector can be easily calculated by using Eqs. (4.3.47) and (4.3.48). The steady state for the coupled cavity fiber lasers is only achieved for one specific eigenvalue and eigenvector, which gives maximum coupling efficiency of the power produced by the individual emitters in the zero diffraction order. This coupling efficiency can be calculated for each eigen-solution by considering the model shown in Fig. 4.3.9. The three beams of amplitudes X_i and phases ϕ_i which correspond to a given eigenvector are launched into the three open cavities.

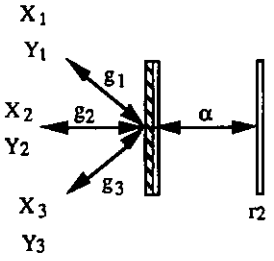

Fig. 4.3.9 Model for the calculation of the coupling efficiency of the fan-in for a given eigenstate characterized by an eigenvalue λ and an eigenvector with the components X_i.

The total amplitude coupled into the zero diffraction order for the most important case of matched phases $\phi_i = m_i\,\pi$ is given by (see Fig. (4.3.4)

$$E_c = A_{-+}\,X_1\,g_1 + A_{oo}\,X_2\,g_2 + A_{+-}\,X_3\,g_3, \qquad (4.3.51)$$

where g_i is the amplitude saturated gain in each cavity for the considered eigenstate. The effective coupling efficiency E_{eff} of the incident amplitudes in the zero diffraction order for any X_i is characterized by a coefficient α which is a function of X_i, namely $E_{eff} = \alpha\,E_c$. The reflected amplitude is given by $E_{refl} = r_2\,E_{eff}$, where r_2 is the amplitude reflectivity of the output mirror. The signal Y_1 which is coupled back into the first fiber is calculated as

$$Y_1 = g_1\,A_{o-}\,E_{refl} = \alpha\,r_2\,g_1\,A_{o-}\,(A_{-+}\,X_1\,g_1 + A_{oo}\,X_2\,g_2 + A_{+-}\,X_3\,g_3). \qquad (4.3.52)$$

The amplitude of the first component of the output vector Y_i is also given by

$$Y_1 = \lambda X_1 \tag{4.3.53}$$

The amplitude coupling efficiency α is obtained by introducing Eq. (4.3.53) in Eq. (4.3.52). This yields

$$\alpha = \frac{\lambda X_1}{r_2 g_1 A_{0-} (A_{-+} X_1 g_1 + A_{00} X_2 g_2 + A_{+-} X_3 g_3)}. \tag{4.3.54}$$

4.3.4.2 Analysis of the eigen-solutions for the condition of minimum losses

In order to investigate the conditions which are necessary for the most efficient coupling of the beams into the zero diffraction order, we will first consider an ideal case with transparent (losseless) fibers by assuming $g_i = 1$, $\forall i$. Under this condition the eigenvalue λ gives a straightforward information of the cavity losses. The effect of the accumulated phases ϕ_i on the eigenvalue λ is shown in Fig. 4.3.10 for transparent fibers.

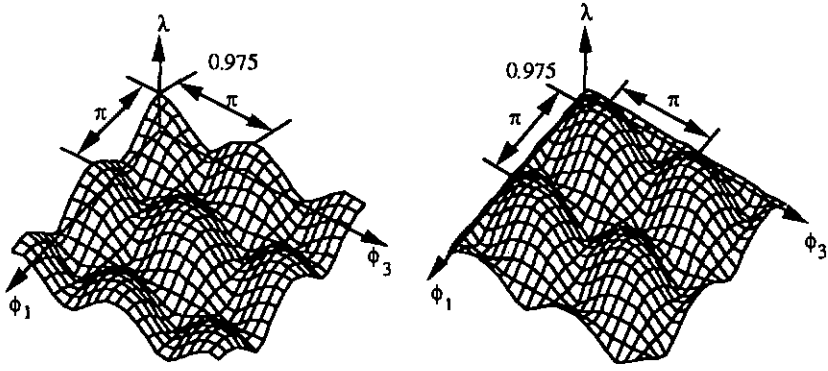

Fig. 4.3.10 Eigenvalue λ as a function of the accumulated phases ϕ_1 and ϕ_3 of the lateral cavities in the case of losseless fibers ($g_i = 1$). The graph on the left side is calculated with $\phi_2 = 0$, and the graph on the right side is calculated with $\phi_2 = \pi/2$.

The graph on the left side shows the eigenvalue λ as a function of ϕ_1 and ϕ_3; the phase of the central cavity is fixed at $\phi_2 = 0$. The phases ϕ_1 and ϕ_3 of the lateral cavities vary over approximately two periods. The maximum value ($\lambda = 0.975$) is obtained whenever the phase difference is given by

$$\phi_i - \phi_j = m\pi, \ (\forall i,j), \tag{4.3.55}$$

where m is an integer (m = 0, 1, ...). The same behavior is observed when the initial phase ϕ_2 is set to any other value, as shown in the graph on the right for $\phi_2 = \pi/2$. This result confirms that the only possible set of phases ϕ_i for maximum coupling efficiency is given by Eq. (4.3.55). Consequently, the more restrictive set of phases $\phi_i = m_i \pi$ given by Eq. (4.3.37) for the laser threshold represents the only possible solution for the steady state oscillation. The eigenvector associated with the optimum eigenvalue $\lambda = 0.975$ is easily calculated using the matrix $\mathbf{E} - \lambda \mathbf{I}$ as defined by Eqs. (4.3.47) and (4.3.48). This yields

$$\vec{X}_\lambda = \begin{pmatrix} 1 \\ i \\ 1 \end{pmatrix}. \tag{4.3.56}$$

The coupling efficiency α calculated by using Eq. (4.3.54) gives $\alpha = 1$ for the eigen-solution ($\lambda = 0.975$, $\vec{X}_\lambda$).Therefore the eigenvector (1, i, 1) describes the ideal illuminations X_i (amplitudes) of the fan-in for an optimum coupling of the power of the individual emitters in the zero diffraction order. If a fan-in with $A_{ij} = A$ is considered, the solution given by Eq. (4.3.56) assumes that any uniform illumination in the three diffraction orders gives the most efficient coupling in the zero diffraction order. The conditions for the steady state can then be summarized in term of accumulated phases ϕ_i and optical power $P_i = X_i^2$ at the input of the fan-in, namely

1. $\phi_i = m_i \pi$, (4.3.57)
2. $P_i = P, \ \forall i$. (4.3.58)

This set of two equations fully characterizes the steady state of the coupled cavity fiber laser. These two conditions will be self established by the coupled lasers since they correspond to a situation of minimum intracavity losses. The adjustment of the mutual phases is achieved by a self adaptation of the optical frequency of the coupled lasers. The optimum distribution of the optical power P_i is given by the power splitting ratio of the fan-in and by the gain saturation, as will be shown in the next section. These equations can be generalized for a system with non uniform fan-in element. In this case the A_{ij} are different for each i and j. It is straightforward to show that condition 1 remains valid, and that condition 2 can be expressed as follows:

The power distribution in the three input laser beams must be identical to the power distribution fixed by the power splitting ratio of the fan-in.

4.3.5. Modeling and effect of the gain saturation

The exact modeling of the gain saturation involves the calculation of the longitudinal distribution of the laser fields which propagate in the forward and backward directions in the active medium, since the local gain saturation is a function of the total local (forward and backward) propagating optical power. The integration of these longitudinal distributions gives a set of non-linear coupled differential equations for the gain and the optical powers, as will be shown in Sect. 4.3.7. The effect of the gain saturation on the self adjustment of the mutual optical powers in the emitters will be more easily understood by considering a simple approximation. The active medium of each cavity is modeled as a two ports device which amplifies an input signal power P_{1i} by a factor G_{si}, which yields $P_{2i} = G_{si} P_{1i}$ at the output of each amplifier. G_{si} is the saturated gain in the i-th emitter which can be calculated by considering the amplification through a gain medium of length L and by assuming an homogenous line broadening [4.8]. The differential equation for the single pass gain in the i-th cavity can be written as

$$\frac{dP_i(z)}{dz} = \gamma_i(z)\, P_i(z), \tag{4.3.59}$$

where the gain coefficient $\gamma_i(z)$ for a homogeneously broadened gain curve is given by

$$\gamma_i(z) = \gamma_{oi} \frac{1}{1 + \frac{P_i}{P_{sat}}}. \tag{4.3.60}$$

P_{sat} is the saturation power and γ_{oi} is the unsaturated gain coefficient in the i^{th} cavity. By introducing Eq. (4.3.60) into Eq. (4.3.59), one gets

$$\gamma_{oi}\, dz = dP_i(z) \left(\frac{1}{P_i(z)} + \frac{1}{P_{sat}} \right). \tag{4.3.60}$$

By integrating the left side of Eq. (4.3.60) between 0 and L and the right part between P_{1i} and P_{2i}, the unsaturated power gain $G_{oi} = \exp(\gamma_{oi} L)$ can be written as

$$G_{oi} = G_{si} \exp\left(\frac{P_{2i} - P_{1i}}{P_{sat}} \right). \tag{4.3.61}$$

By using the relation $G_{si} = P_{2i} / P_{1i}$, one gets

$$G_{oi} = G_{si} \exp\left(\frac{-(G_{si} - 1)}{G_{si}} \frac{P_{2i}}{P_{sat}} \right). \tag{4.3.62}$$

This implicit equation allows to calculate the saturated gain G_{si} as a function of the output power P_{2i} for a given unsaturated gain G_{oi}. An example of the signal induced gain saturation is shown in Fig. 4.3.11 for a typical Nd^{3+} doped fiber amplifier with G_{oi} = 30 dB and with P_{sat} = 2.5 mW.

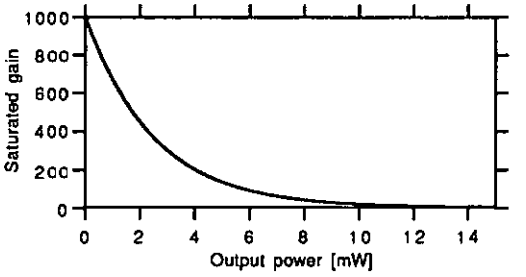

Fig. 4.3.11. Saturated gain as a function of the output power of a typical a Nd^{3+} doped fiber amplifier with an unsaturated gain G_{oi} = 30 dB and P_{sat} = 2.5 mW.

The onset of the gain saturation in the i-th laser cavity is approximated by using Eq. (4.3.62). In this condition P_{2i} has to be replaced by P_i, where P_i is the optical power at steady state in the i-th cavity. The condition for the laser threshold connects the power saturated gains $g_i^2 = G_{si}$ in the three cavities as shown in Eq. (4.3.38) for matched cavity phases and symmetrical fan-in, namely

$$\sum_i G_{si} = \frac{1}{A^2 r_1 r_2} . \qquad (4.3.63)$$

The unsaturated gains G_{oi} are function of the absorbed pump powers and can be written by using Eq. (2.25), namely $G_{oi} = \exp(\Gamma_o(L))$. Therefore, for a given set of G_{oi}, Eq. (4.3.63) gives a relationship between the individual optical powers P_i in the cavities. The self-distribution of the mutual powers P_i for the steady state given by Eq. (4.3.57) will be established by means of the gain saturation. This can be understood by considering the onset of the saturation when the lasers are switched on. Let us assume a symmetrical fan-in and different unsaturated gains G_{oi} in each cavity. This yields a non uniform initial illumination of the fan-in which gives intracavity losses in the higher diffraction orders. Nevertheless, the zero order which is reflected by the output mirror is coupled back with a uniform power distribution in each cavity. Depending on the unsaturated gain, the power in each cavity reaches the value at steady state more or less rapidly. As an example, the fastest initial increase of the optical power will be observed in the cavity with the highest unsaturated gain G_{oi}, to reach the steady state

fixed by the saturation and Eq. (4.3.63). The splitting ratio of the optical power in the three emitters at steady state is then fixed by the power splitting ratio of the fan-in. The self adjustment of the mutual cavity optical powers P_i results in a distribution of the output power in the diffraction orders at steady state which is independent of the distribution of the unsaturated gains in each cavity. Any distribution of the pump power in the individual emitters can be applied without a change in the coupling efficiency. The coupling efficiency is defined as the ratio of the power in the zero diffraction order and the total power in all five diffraction orders, as shown in Fig. 4.2.1. The gain saturation in the three fiber lasers and the steady state condition are shown in Fig. 4.3.12.

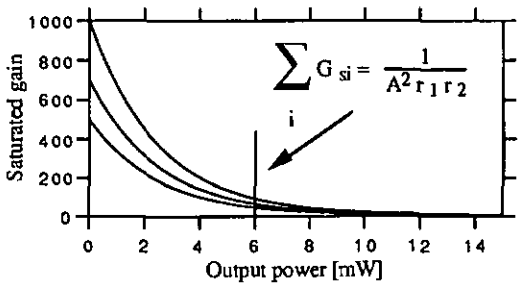

Fig. 4.3.12. Saturated gains as a function of the output power in the three cavities. Since the fan-in is assumed to be symmetrical, the output power P_i of each cavity must be the same ($P_i = P_o$). The steady state condition is fulfilled when the sum of the saturated gains G_{si} meets the threshold condition.

The stability of the coupling efficiency has been experimentally verified by considering the setup of three coupled fiber lasers as shown in Fig. 4.2.4. The coupling efficiency η_c of the output power in the zero diffraction order has been measured for several distributions of the pump power absorbed in each cavity. This efficiency η_c is calculated as the ratio of the power which is measured in the zero order with the total output power measured in the five diffraction orders ($\pm 1, 0, \pm 2$). The measurements were performed by using a large area silicon detector and by measuring successively the power in the five diffraction orders for each set of pump levels. These measurements gave a mean coupling efficiency of $\eta_c = (67.7 \pm 1.4)$ %, which proves the stability of the coupling in the zero order considering the accuracy of the measurement of η_c. The results of these measurements are shown in Fig. 4.3.13. The unsaturated gains in each cavity are shown in the table below for these measurements. These gains have been calculated by assuming a typical gain of 0.37 dB/mW and a pump coupling efficiency of 30 %.

Graph N_o	1	2	3	4	5	6	7
G_{o1} [dB]	10.5	10.5	10.5	10.5	7.3	6.6	7.3
G_{o2} [dB]	11.8	10.7	8.3	6.1	6.1	10	10
G_{o3} [dB]	10.3	9	10.3	10.3	10.3	8	0

The unsaturated gain G_{o2} of the center cavity is changed from 11.8 dB (15 x) in graph 1 to 6.1 dB (4 x) in graph 4 without any change in the coupling efficiency. The same behavior has been obtained for an extreme case where the pump of one of the lateral cavities was switched off.

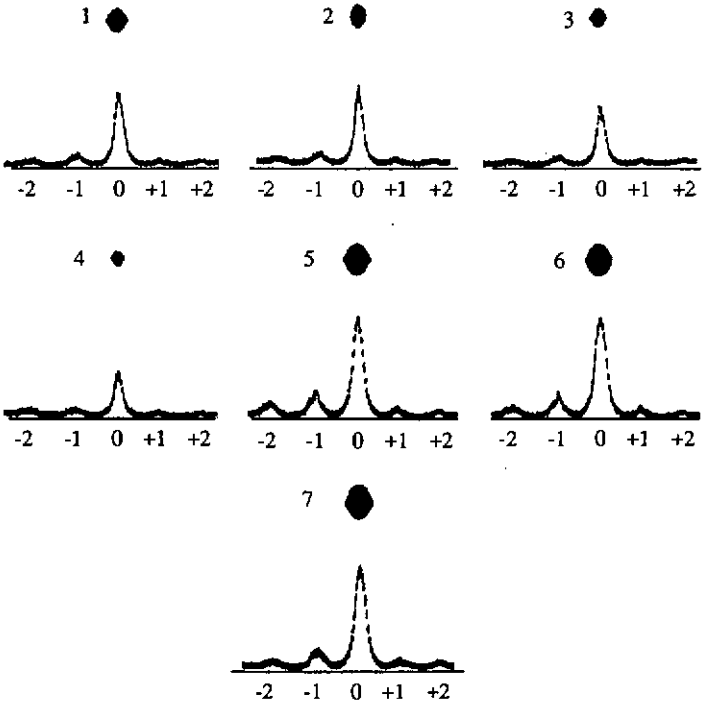

Fig. 4.3.13. Distribution of the output power in the five diffraction orders for several sets of pump levels in the three fiber lasers. Graphs 1, 2, 3, 4 show the power distribution when the unsaturated gain of the center cavity is changed, while the two lateral cavities have fixed unsaturated gains. Graphs 5 and 6 show the same distribution when the gains of the lateral cavities are changed. A coupling efficiency of $\eta_c = (67.7 \pm 1.5)$ % was obtained. Graph 7 shows the power distribution when only two of the three emitters are pumped ($G_{o1} = 7.3$ dB, $G_{o2} = 10$ dB, $G_{o3} = 0$ dB). The same coupling efficiency was obtained.

4.3.6. Measurement of the cavity losses by considering the dynamic of the coupled cavity laser

The characterization of the intracavity losses is important for the optimization of the power properties of a laser, since the pump laser threshold and the slope efficiency strongly depend on this parameter. In this section, the losses of the coupled cavity system are analyzed by considering the dynamic properties of the slightly perturbed laser cavity. A small perturbation of the pump beam is used to produce oscillations of relaxation. The dependence of the frequency of the oscillations on the pumping level allows to extract information on the cavity losses.

4.3.6.1 Basic principle

If we consider a four level system, and by assuming no ground state depletion due to the CW pump beam, it can be shown with perturbation calculation [4.3] that the fluctuation of the photon number $\Phi(t)$ around the steady state is given by

$$\Phi(t) = \Phi_0 \exp(-rt/2\tau) \cos(\omega t) = \Phi_0 \exp(-\alpha t) \cos(\omega t), \tag{4.3.64}$$

where $\alpha = r/2\tau$ gives the exponential decay of the induced oscillations, τ is the fluorescence lifetime, and r is the relative pumping rate which is given by

$$r = \frac{P}{P_{th}}, \tag{4.3.65}$$

where P_{th} is the pump power at threshold. The circular frequency ω of the oscillations of relaxation is given by

$$\omega = \sqrt{(r-1)/t_c\,\tau}, \tag{4.3.66}$$

where t_c is the cavity lifetime, which can be written as a function of the cavity losses, namely

$$t_c = -\frac{2nL}{c\,\ln(A)}, \tag{4.3.67}$$

where L is the cavity length, c is the speed of light in vacuum, n is the index of refraction of the material, and A is given by

$$A = R_1 R_2 (1-\rho)^2, \tag{4.3.68}$$

where R_1 and R_2 are the reflectivities of the input and output mirrors, respectively, and ρ is the single pass cavity loss. By introducing Eq. (4.3.65) in Eq. (4.3.66), one gets

$$\omega^2 = \frac{1}{\tau\, t_c}\left(\frac{P}{P_{th}} - 1\right). \tag{4.3.69}$$

This expression is only valid for a plane wave laser. In the more general case of a waveguide structure, Eq. (4.3.69) must be slightly modified [4.4], in order to take into account the overlap of signal and pump modes. This results in an additional factor β, which is an overlap integral as described in [4.5]. Equation (4.3.69) reads now

$$\omega^2 = \beta \frac{1}{\tau t_c}\left(\frac{P}{P_{th}} - 1\right), \tag{4.3.70}$$

where β for small signal power (i.e. negligible saturation) is defined as

$$\beta = \frac{I_1^2}{I_{11}}, \tag{4.3.71}$$

with

$$I_1 = \int_0^{2\pi} d\phi \int_0^{\infty} dr\, r \int_0^{L} dz\, P(r,\Phi,z)\, S(r,\Phi,z), \tag{4.3.72}$$

and

$$I_{11} = \int_0^{2\pi} d\phi \int_0^{\infty} dr\, r \int_0^{L} dz\, S^2(r,\Phi,z)\, P(r,\Phi,z), \tag{4.3.73}$$

where L is the length of the fiber, $P(r,\Phi,z)$ is the pump and $S(r,\Phi, z)$ is the signal power distribution. Equations (4.3.72) and (4.3.73) can be rewritten by separating the radial and longitudinal terms, namely $P(r,\Phi,z) = P(r,\Phi)P(z)$, and $S(r,\Phi,z) = S(r,\Phi)S(z)$. $S(z)$ and $P(z)$ are normalized in such a way that their integration over the fiber length L gives 1. For uniform longitudinal distribution of the laser and pump modes, $S(z)$ and $P(z)$ are thus given by $S(z) = 1/L$ and $P(z) = 1/L$. This yields

$$I_1 = \frac{1}{L} \int_0^{2\pi} d\phi \int_0^{\infty} dr\, r\, P(r,\Phi)\, S(r,\Phi) \qquad (4.3.72_b)$$

$$I_{11} = \frac{1}{L^2} \int_0^{2\pi} d\phi \int_0^{\infty} dr\, r\, S^2(r,\Phi)\, P(r,\Phi). \qquad (4.3.73_b)$$

This approximation has shown to be in very good agreement with the exact solutions calculated in [4.6] for a typical Nd^{3+} doped fiber. The graph of ω^2 as a function of P is a straight line which is given by

$$\omega^2(P) = \omega_0^2 + \frac{d\omega^2}{dP} P. \qquad (4.3.74)$$

This yield, by using Eq. (4.3.70),

$$\omega^2(P) = -\frac{\beta}{t_c \tau} + \frac{\beta}{t_c\, \tau\, P_{1h}} P. \qquad (4.3.75)$$

By introducing Eq. (4.3.75) into Eqs. (4.3.67) and (4.3.68), one gets for the single-pass cavity losses

$$\rho = 1 - \frac{1}{\sqrt{R_1 R_2}} \exp\left(\frac{-nL\tau}{\beta c} | \omega_o^2 |\right) \qquad (4.3.76)$$

The ratio of Eq. (4.4.12) and Eq. (4.4.11) gives for the pump power at laser threshold

$$P_{th} = \frac{| \omega_o^2 |}{(d\omega^2/dP)}. \qquad (4.3.77)$$

Measuring ω^2 as a function of the absorbed pump power P gives immediately the value of ω_o^2. This parameter does not depend on the absolute scaling of the absorbed pump power, which is of a great practical interest since the pump coupling efficiency is not easily measured with high accuracy.

4.3.6.2 Measurements on the coupled cavity lasers

The frequency of the oscillations has been measured as a function of the absorbed pump power by using the experimental setup which is shown in Fig. 4.2.4. For each measurement, the relaxation has been produced by a small mechanical perturbation (single shock) applied to the output mirror. The graph of the square of the circular frequency of the relaxation oscillations as a function of the absorbed pump power is shown in Fig. 4.3.14. The absorbed pump power is calculated as the sum of the power which is absorbed in each cavity. The pump coupling efficiency was estimated to be 30 %.

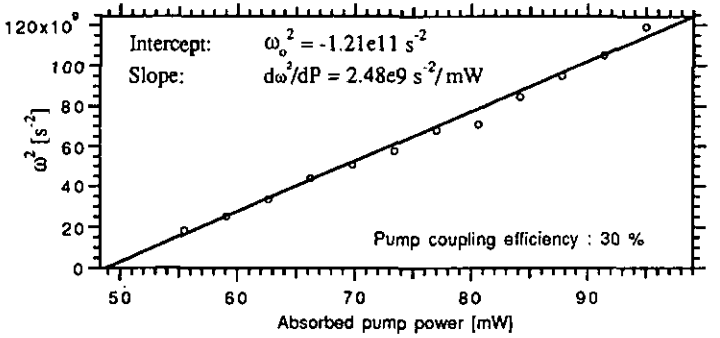

Fig. 4.3.14. ω_0^2 as a function of the absorbed pump power for the three coupled cavity lasers. The pump coupling efficiency was 30 %.

The characteristics of the doped fiber were NA = 0.21 and core diameter = 3.5 μm. This yields a cutoff wavelength of 960 nm. The mean pump wavelength was 817 nm. The fiber supports two modes at this wavelength. Nevertheless, by carefully adjusting the pump coupling efficiency, almost all the pump power was coupled into the fundamental mode. By introducing these parameters in Eq. (4.3.71) and (4.3.76), the overlap integral calculated for fundamental signal and pump modes gives $\beta = 0.8$. The effective length of the coupled cavity lasers was determined by measuring the beat frequency between the successive longitudinal modes of the lasers, as shown in Fig. 4.3.15. An effective optical length $L_{eff} = 4.31$ m was obtained. By assuming an index of refraction $n = 1.46$ for the fiber core, this yields a cavity length of $L_c = L_{eff}/n = 2.95$ m. This length corresponds to the length of the individual fibers. The single pas losses, calculated form the measured value of $\omega_0^2 = -1.20891 \cdot 10^{11}\ s^{-2}$, and by using Eq. (4.3.76), is then $\rho = 63$ %. The parameters which are necessary for the determination of ρ with Eq. (4.3.76) are $R_1 = 100$ %, $R_2 = 96$ %, and $\tau = 470\ \mu s$.

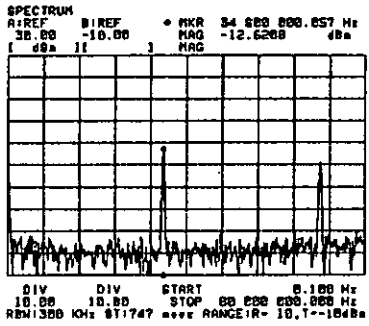

Fig. 4.3.15. measured beat frequency signal between successive longitudinal modes of the coupled cavity lasers. The signal was detected by a high speed photodetector (bandwidth 250 MHz). The fundamental beat frequency was 34.8 MHz, which yields an effective cavity length of Lc = Leff/n = 2.95 m for an index of refraction n = 1.46 in the fiber core.

The pump laser threshold obtained from Eq. 4.3.77 gives a value of P_{th} = 49 mW, which is in a good agreement with the threshold of P_{th} = 51 mW extrapolated from the power characteristics of the coupled lasers shown in Fig. 4.3.21 (Sect. 4.3.7). The high single-pass cavity losses of 63 % are in good agreement with the theoretical estimation, which will be more extensively described in the next section.

4.3.6.3 Theoretical estimation of the intra-cavity losses

The schematic structure of the coupled cavity lasers is shown again in Fig. 4.3.16. The main contributions to the intracavity losses are the back-coupling efficiency η_f of the laser beam into the three fibers, the transmission efficiency η_{cl} through the collimation lens, the transmission efficiency η_m through the photoresist of the fan-in element, the coupling efficiency η_{ce} of the fan-in, and all the transmission efficiencies η_{Fr} reduced by Fresnel reflection on the interfaces. Considering the transmission from the left to the right in Fig. 4.3.16, the total transmission η_{tot} becomes

$$\eta_{tot} = \eta_f \cdot \eta_{cl} \cdot \eta_{Fr} \cdot \eta_m \cdot \eta_{ce} \cdot \eta_{Fr} \,. \qquad (4.3.78)$$

The typical values were η_f = 60 %, η_{cl} = 92 %, η_m = 98 %, η_{ce} = 77 %, η_{Fr} = 96 %, which gives a transmission of η_{tot} = 38 %. The single-pass losses are then given by $\rho_{th} = 1-\eta_{tot}$ = 62 %. This value is in very good agreement with the measured single-pass losses ρ_{mes} = 63 %.

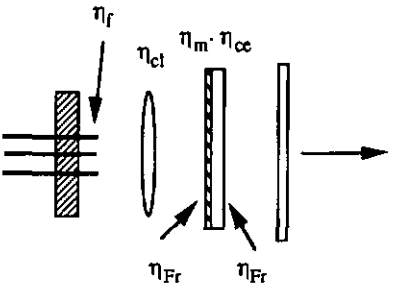

$$\eta_{tot} = \eta_f \eta_{cl} \eta_{Fr} \eta_m \eta_{ce} \eta_{Fr}$$

Fig. 4.3.16. Schematic structure of the coupled cavity lasers and the distribution of the intracavity losses. η_f is the fiber coupling efficiency, η_{cl} is the transmission through the collimating lens, η_{Fr} is the transmission through an air/glass interface (Fresnel), η_m is the transmission through the photoresist, and η_{ce} is the coupling efficiency of the fan-in element.

4.3.7. Power properties of the coupled cavity fiber lasers

The output power of the coupled lasers can be modeled for the steady state by considering that the total output power is given by the coherent addition of the contribution provided by the individual emitters. If we assume a symmetrical coupling element and matched mutual phases ϕ_i, the total output power can be written as

$$P_{out} = N^2 A^2 T P_i, \qquad (4.3.79)$$

where N is the number of emitters, A^2 is the power splitting ratio of the symmetrical fan-in, and $P_i = P_o$ is the output power of each laser. This well known equation states that the total output power increases with the square of the number of coherently coupled emitters. Nevertheless, for energy conservation, the maximum value for the power coupling efficiency of a losseless symmetrical fan-in is $A^2 = 1/N$. Consequently, P_{out} increases linearly with the number N of emitters. If we assume identical pumping of the individual emitters, which yields identical gain saturation, the analysis of the coupled lasers can be simplified by considering the modeling of three individual lasers with identical gain saturation and output power. The total output power of the coherently added emitters is then given by Eq. (4.3.79).

4.3.7.1 Modeling of the individual emitters

Each source is a fiber laser of length L with and input and output mirror of power reflectivities R_1 and R_2, respectively. The single pass cavity loss L_o, which is mainly due to the coupling efficiency of the fan-in and to the fiber back-coupling efficiency, is modeled by considering an effective reflectivity R_{2eff} of the mirror [4.8] which is given by

$$R_{2eff} = (1-\rho)^2 R_2, \tag{4.3.80}$$

where the term $(1-\rho)^2$ stems for the round trip cavity loss. The effective transmission is given by

$$T_{eff} = (1-R_2) \tag{4.3.81}$$

This in turn allows to simplify the propagation equations for the forward and backward optical power in the resonator by considering a losseless resonator and by including the effect of the cavity losses in the effective reflectivity R_{eff}. This assumption has also the advantage to preserve the correct power distribution in the laser cavity, since the lossy element is modeled at the output of the laser cavity as it is in the coupled cavity lasers. The forward and backward optical powers $P^+(z)$ and $P^-(z)$ in the laser cavity are given by

$$\frac{dP^+(z)}{dz} = \gamma(z)\, P^+(z), \tag{4.3.82}$$

$$\frac{dP^-(z)}{dz} = -\gamma(z)\, P^-(z), \tag{4.3.83}$$

where $\gamma(z)$ is the gain coefficient for homogeneously broadened gain curve which is given by

$$\gamma(z) = \frac{\gamma_0}{1 + \dfrac{P^+(z) + P^-(z)}{P_{sat}}}, \tag{4.3.84}$$

where P_{sat} is the saturation power, namely $P_{sat} = h\nu / \sigma\tau_{21} A_{seff}$ [3.6]. A_{seff} is the effective area of the signal mode which is given by Eq. (4.3.92). The differential equations (4.3.82) and (4.3.83) are coupled through the saturation term of $\gamma(z)$, which depends on the total forward and backward propagating power. Nevertheless, these equations can be decoupled by considering that

$$\frac{d}{dz}\left(P^{+}(z)\,P^{-}(z)\right)=0, \tag{4.3.85}$$

which yields

$$P^{+}(z)\,P^{-}(z))=C, \tag{4.3.86}$$

where C is a constant. The differential equations are decoupled by introducing Eq. (4.3.86) in Eq. (4.3.84). By using this technique Eqs. (4.3.82) and (4.3.83) can be solved by considering the boundary conditions fixed by the cavity mirrors, as shown in Fig. 4.3.17.

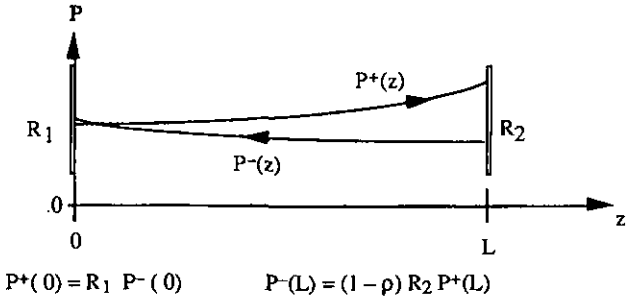

Fig. 4.3.17. Distribution of the forward and backward propagating power in the laser cavity and the boundary conditions on the two mirrors.

Equation (4.3.85) can be written as

$$dP^{+}\left(\frac{1}{P^{+}(z)}+\frac{1}{P_{sat}}+\frac{C}{P_{sat}\,P^{+}(z)^{2}}\right)=\gamma_{o}\,dz. \tag{4.3.87}$$

The same expression can be found for $P^{-}(z)$, namely

$$dP^{-}\left(\frac{1}{P^{-}(z)}+\frac{1}{Psat}+\frac{C}{P_{sat}\,P^{-}(z)^{2}}\right)=-\gamma_{o}\,dz. \tag{4.3.88}$$

The left side parts of Eqs. (4.3.87) and (4.3.88) are integrated between $P^{+}(0)$ and $P^{+}(L)$ and between $P^{-}(L)$ and $P^{-}(0)$, respectively, and the right side parts are integrated between 0 and L. By using the boundary conditions, as defined in Fig. 4.3.15, and by using Eq. (4.3.85), the forward power $P^{+}(L)$ can be written as

$$P^{+}(L) = \frac{P_{sat}}{(1 + r_{2eff}/r_1)(1 - r_{2eff}\, r_1)} \left[\Gamma_0 + \ln (r_1\, r_{2eff})\right], \qquad (4.3.89)$$

where Γ_0 is the unsaturated (small) gain coefficient, as defined in Eq. (2.25), and $r_1 = \sqrt{R_1}$, $r_{2eff} = \sqrt{R_{2eff}}$ are the amplitude reflectivities of the input and output cavity mirrors, respectively. P_{sat} is the saturation power which is given by $P_{sat} = I_{sat}\, A_{eff}$, where I_{sat} is the saturation intensity as defined in Chapt. 2, and A_{eff} is the effective mode area. The laser output power is given by

$$P_{out} = T_{eff}\, P^{+}(L) = (1 - R_2)\, P^{+}(L). \qquad (4.3.90)$$

4.3.7.2 Output power of the coupled emitters

The output power of the coupled cavity lasers is obtained by using Eqs. (4.3.79) and (4.3.90). A typical result is shown in Fig. 4.3.18 for three coupled lasers. The unsaturated gain coefficient is 0.52 dB/mW and the pump efficiency is $\eta_q = 0.66$ %, as defined in Chapt. 2. The saturation power is $P_{sat} = 2.5$ mW. The output power is shown for different single pass intracavity losses p, namely $\rho = 0$ %, $\rho = 16$ %, $\rho = 72$ %. The fan-in is assumed to be symmetrical and losseless (Aij = A = 1 / $\sqrt{3}$). The absorbed pump power is the total pump power which is absorbed in the three cavities. The pump power is assumed to be identical in the three lasers.

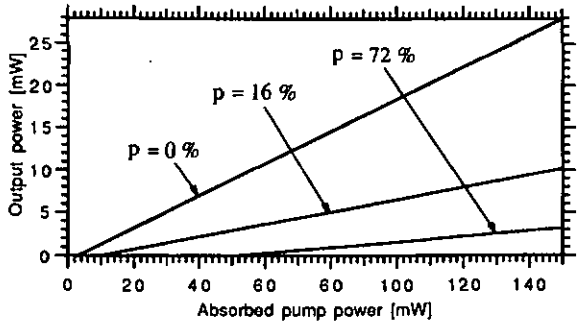

Fig. 4.3.18. Output power as a function of the absorbed pump power of the coupled cavity fiber lasers for different single pass intracavity losses ρ. The mirror reflectivities are $R_1 = 99$ % and $R_2 = 85$ %. The gain coefficient is $\Gamma_0 = 0.52$ dB/mW.

The laser thresholds are P_{th} = 3.2 mW for ρ = 0 %, P_{th} = 10 mW for ρ = 16 %, and P_{th} = 51.2 mW for ρ = 72 %. The maximum output power which can be obtained for a given set of ρ, P_{sat} and pump levels P_{abs} can be optimized by a careful adjusting of the transmission T_{eff} of the output mirror. This can be calculated by solving Eq. (4.3.90) as a function of $T_{eff} = 1 - R_2$ for a given set of gain coefficient Γ_0 and intracavity single pass loss ρ. This optimization is shown in Fig. 4.3.19. For this example the absorbed pump power is P_{abs} = 50 mW in each cavity.

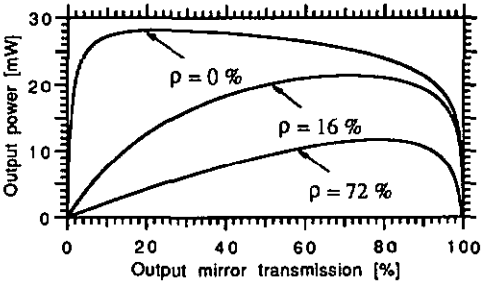

Fig. 4.3.19 Output power as a function of the transmission T_{eff} of the output mirror for different single pass intracavity losses ρ. The pump power is P_{abs} = 50 mW in each laser.

For small intracavity losses, the maximum output power is achieved for low output coupling, namely T ≈ 20 %, which yields a laser output power of 28 mW.

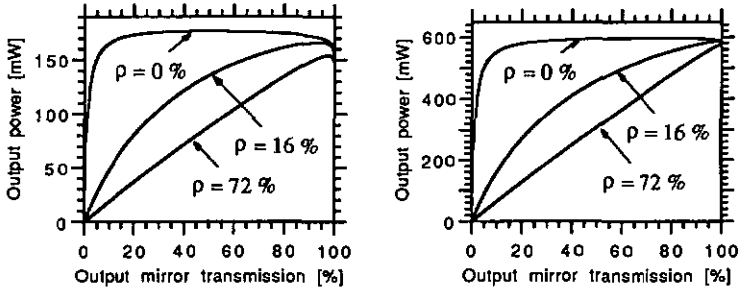

Fig. 4.3.20 Output power as a function of the transmission T_{eff} of the output mirror for high pump levels. The absorbed pump power in each cavity is P_{abs} = 300 mW (left) and P_{abs} = 1 W (right).

The adjustment of the transmission is not critical, since the slope of the curve is very small. For $\rho = 72$ % the optimum output coupling is obtained for $T_{eff} \approx 78$ %, with an output power of 13 mW. In this case, the adjustment of T_{eff} becomes more critical, since the slope of the curve increases near the optimum value. This behavior becomes more evident for higher pumping levels, as shown in Fig. (4.3.20). For large values of ρ the maximum output power is achieved for a very large T_{eff}, namely $T_{eff} \approx 98$ %, which yields obviously a very high laser threshold. Nevertheless, the maximum output power becomes almost as large as the output power of the losseless cavity ($\rho = 0$ %). This is due to the very high unsaturated gains which can be achieved, since this model assumes that all the pump power remains absorbed and that ground state depletion is negligible. A second limitation of the maximum output power is fixed by the properties of the waveguide, through the saturation power P_{sat} and the gain coefficient Γ_0. P_{sat} is given by [3.6]

$$P_{sat} = I_{sat} A_{seff} = \frac{h\nu_s}{\sigma\tau_{21}} A_{seff}, \tag{4.3.91}$$

where $h\nu_s$ is the signal photon energy, σ is the emission cross-section, τ_{21} is the fluorescence lifetime, and A_{seff} is the effective signal mode area, which depends on the numerical aperture NA of the fiber, namely

$$A_{seff} = \pi \cdot \left(\frac{\lambda_s}{\pi \cdot NA} \right)^2. \tag{4.3.92}$$

Consequently the saturation power P_{sat} decreases for increasing numerical aperture. The gain coefficient Γ_0, as defined by Eqs. (2.25), depends mainly on the parameter F/η_p, which describes the signal and pump modes overlap, and on the fiber core area A_f. For a given core diameter, the coefficient F/η_p increases when the numerical aperture is increased, as shown in Fig. 2.3. The output power of the coupled lasers, as given by Eq. (4.3.90), is proportional to the saturation power P_{sat} and to the gain coefficient Γ_0. Therefore, for a given core diameter the maximum output power will be achieved only for a specific value of NA, as shown in Fig. 4.3.21 (dashed line) for a core diameter $\Phi_c = 3.5$ µm, a signal wavelength $\lambda_s = 1088$ nm and a pump wavelength $\lambda_p = 817$ nm. The single pass loss is $\rho = 70$ %, the gain coefficient is given by Eq. (2.25), with the typical values for the cross section, pump efficiency and fluorescence lifetime measured in Chapt. 2. The absorbed pump power in each cavity is $P_{abs} = 50$ mW. The maximum output power is achieved with NA = 0.14 for this core diameter. In the same way, the output power can be considered as a function of the core diameter, for a given NA. In this case the saturation power remains constant when the core diameter is changed, since it does only depend on the mode confinement, which is fixed by the numerical aperture NA. The gain coefficient Γ_0 shows a fast initial increase when Φ_c increases

from small starting values, since the overlap coefficient F/η_p increases more rapidly than the core area A_f. For larger Φ_c, A_f increases more rapidly than F/η_p, which yields a reduction of Γ_o, as seen in Fig. 4.3.22. Consequently, for a given NA the maximum output power is again achieved only for one specific core diameter, as shown in Fig. 4.3.21 (solid line) for the same set of parameters as described in Fig. 4.3.21.

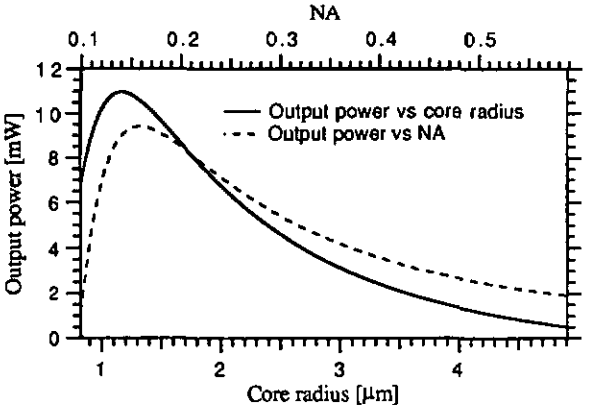

Fig. 4.3.21. Output power as a function of the core radius (solid line) and as a function of the numerical aperture NA (dashed line). For the solid line the NA is fixed at NA = 0.21, and for the dashed line, the core radius is fixed at $\Phi_c / 2 = 1.75$ μm. The absorbed pump power in each cavity is $P_{abs} = 50$ mW. The reflectivities of the input and output mirrors are $R_1 = 100$ % and $R_2 = 85$ %, respectively. The gain coefficient is given by Eq. (2.25), with the typical values for the cross section, pump efficiency and fluorescence lifetime measured in Chapt. 2.

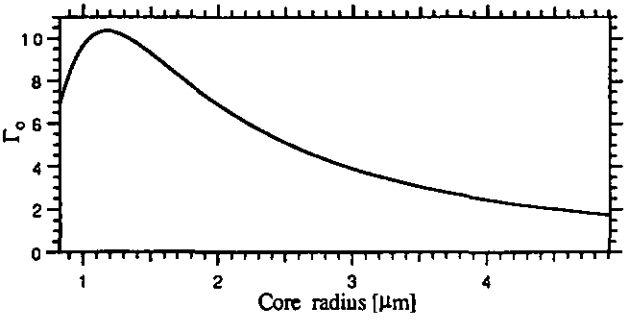

Fig. 4.3.22. Gain coefficient as a function of the core radius for NA = 0.21. The other parameters of the coupled lasers are described in Fig. 4.3.21.

Consequently, the fiber core diameter Φ_c and the numerical aperture NA have to be carefully adjusted to optimize the power properties of the coupled lasers. Nevertheless, three other important parameters have to be considered. First of all, the V number of the fiber has to be kept within a range allowing both the signal and pump light to be single mode for maximum unsaturated gain, which yields for the case of a Nd^{3+} doped fiber pumped at 817 nm a $V_{max} = 1.8$ at $\lambda_s = 1088$ nm. The second limit is fixed by the efficiency of the guiding in the fiber. A typical minimum value for reasonably good guiding is V = 1.3. Consequently, the optimum V will be chosen in the range $1.3 < V < 1.8$. The trade-off between the core diameter Φ_c and the numerical aperture NA has to be chosen as a function of the specific interest. As an example, a low core diameter and a large NA results in a high gain but with the draw back of a low saturation power.

4.3.7.3 Measurement of the power properties of the coupled lasers

The output power of the coupled lasers has been measured by using the experimental setup shown in Fig. 4.2.4. The pump wavelength in the three cavities was 810 nm, 818 nm and 824 nm, respectively. The pump coupling efficiency was 30 %. The reflectivities of the input and output mirrors were $R_1 = 99$ % and $R_2 = 96$ % at $\lambda_s = 1088$ nm. The graph in Fig. 4.3.23 shows the output power in the zero diffraction order as a function of the total pump power absorbed in the three fibers. The three fibers are 500 ppm Nd^{3+} doped and have an attenuation of typically 14 dB/m at $\lambda_p = 810$ nm. Each cavity is 2.95 m long, which allows that all the pump power in the fibers is absorbed. A typical slope efficiency of 3 % and a laser threshold of $P_{th} = 51$ mW have been measured.

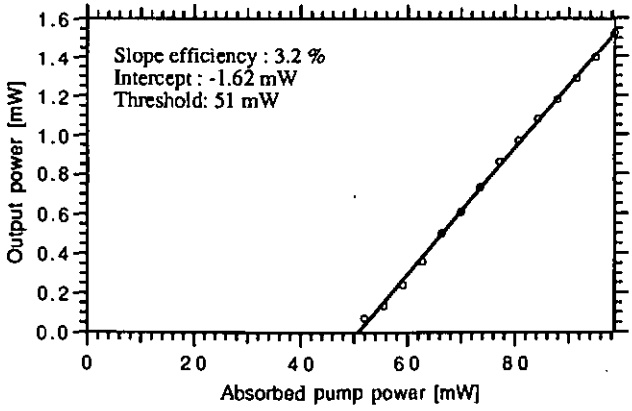

Fig. 4.3.23. Output power as a function of the total absorbed pump power in the three lasers.

The circles are the experimental data and the solid line shows a best fit, calculated with Eq. (4.3.90) and assuming a typical pump efficiency η_p of 0.66. The free parameters for the fit were the reflectivity R_2 of the output mirror, the cavity losses ρ and the unsaturated gain coefficient Γ_0. This yields Γ_0 = 0.52 dB/mW, ρ = 71 % and R_2 = 85 %. The theoretical values for Γ_0 can be calculated by using Eq. (2.25) for a fiber with NA = 0.21 and core radius = 1.75 µm. The pump and the signal wavelengths are λ_p = 817 nm (mean value) and λ_s = 1088 nm, respectively. This yields Γ_0 = 1.06 dB/mW for a LP01 pump mode and Γ_0 = 0.55 dB/mW for a LP11 pump mode. The measured value Γ_0 = 0.52 dB/mW is in good agreement with these theoretical values, if we admit that the pump light was in the LP11 mode. The reflectivity of the output mirror R_2 = 85 %, which has been obtained from the best fit, is somewhat lower than the real value of R_2 = 95 %. This difference is attributed to the changes of the reflectivity of the mirror due to the Fabry-Perot effect in the thickness of the output mirror. This effect is particularly important in the coupled lasers because of the frequency changes which are necessary for the steady state. Finally, the single-pass losses ρ obtained from the fit is ρ = 71%. This value is in good agreement with the single pass loss ρ = 63 % measured in Sect. 4.3.6. Consequently, this simplified model for the output power of the coupled lasers gives an accurate description, which allows to describe all the basic optimizations for an improved output power, considering the properties of the waveguide and the intracavity and output coupling losses. It must be pointed out that this model does not take into account the saturation of the pump beam and the ground state depletion. Therefore, the exact characterization of the output power of very high power lasers would require an improvement of this model to address these two effects. Nevertheless, even in this case, this simple model allows to investigate most of the relevant parameters for the optimization of the coupled lasers.

4.3.7.4 *Output power stability*

The power stability of the coupled cavity fiber lasers does mainly depend on the stability of the amplitude and phase matching between the individual emitters, which is self established in the coupled cavities. This stability has been measured by using the experimental setup as described in Fig. 4.2.4. The output power in the zero diffraction order was measured as a function of time, during a period of typically 500 seconds. The fiber laser cavities were left unperturbed during the measurements. A maximum peak to peak fluctuation of the output power of 5 % has been measured, as shown in Fig. 4.3.24. The principal sources of power fluctuations are given by the mechanical instabilities of the laser resonators, which may produce oscillations of relaxation, and also by the Fresnel back-reflections, which result in the build up of parasitic coupled Fabry-Perot cavities. These cavities act as Fabry Perot etalons with a transmission which depends on the optical frequency. This results in a power modulation when the optical frequency adjusts itself in the coupled cavity laser to fulfill the condition of minimum losses.

Nevertheless, these power instabilities can be minimized by using antireflection coatings and by a careful design of a compact and stable structure for the coupled lasers.

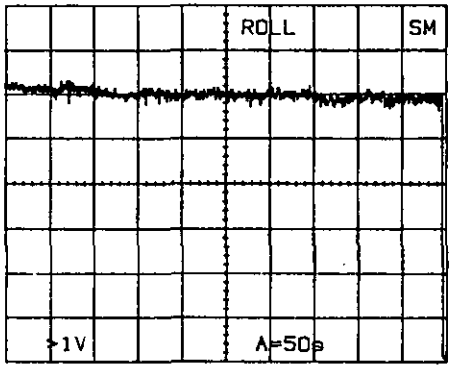

Fig. 4.3.24. Output power stability of the coupled lasers. The mean output power was P_{out} = 0.32 mW. A maximum peak to peak power fluctuation of 5 % has been measured during 500 sec.

Another source of power fluctuations is given by the changes of the polarization states of the beam incident to the fiber grating, since the contrast of the interferences, and thus the coupling efficiency, depends on the mutual polarization states. When the geometry of the fiber laser cavities is left fixed, the fluctuations of the output polarization states can be attributed to thermal effects. Nevertheless, these effects have been shown to be negligible, as can be seen in Fig. 4.3.25.

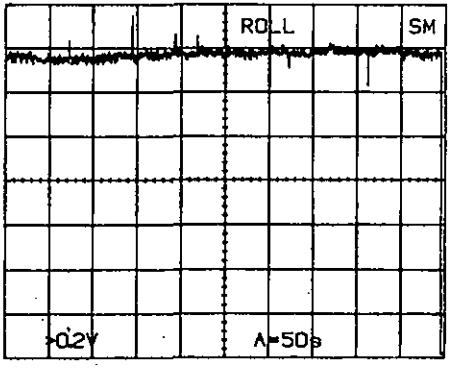

Fig. 4.3.25. Output power when the temperature of one of the fiber is changed between 27 °C and 70 °C. No significant effects have been measured.

In this figure the output power of the coupled lasers is shown when the temperature of one of the cavities is locally changed between 27 °C and 70 °C. No significant changes have been measured and the typical peak to peak power fluctuations remain within the range of 5%.

4.3.8. Discussion of the coupling efficiency and evidence of the coherent addition

4.3.8.1 Coupling efficiency

The coupling efficiency of the three laser beams in the zero diffraction orders is fixed by the self adjustment of the mutual amplitudes and phases of the individual emitters as shown in Eqs. (4.3.57) and (4.3.58) and by the efficiency of the fan-in element. The maximum efficiency of the fan-in depends on the optimization process which is used for the design [4.2]. As an example, a 3 to 1 continuous surface relief grating fan-in (phase grating) with a power splitting ratio of 1:1:1 yields a coupling efficiency of 93.8 % when illuminated with the optimum amplitudes and mutual phases. This maximum coupling efficiency depends on the number of input beams and on the power splitting ratios A_{ij}^2 of the fan-in. Consequently, a trade-off can be found for a given configuration of coupled lasers which allows to achieve the best coupling efficiency and the maximum output power. As an example, a 3 to 1 fan-in element with a power splitting ratio of 1: 4: 1 and mutual phases 0, $\pi/2$, 0 gives a coupling efficiency of 98.6 %. In this case the coupling efficiency is slightly improved, but the power distribution is non uniform and the maximum output power of the coupled lasers is lower. In our experiment, we have achieved a maximum coupling efficiency of 77 %, as shown in Fig. 4.2.5. The setup which was used for this measurement is shown in Fig. 4.2.4. For this experiment the power splitting ratio of the fan-in was 0.55: 1: 0.55, which results in a maximum theoretical coupling efficiency of 96.3 %. The discrepancy between the measured value and the theoretical coupling efficiency is explained mainly by two considerations. First of all, the quality of the wavefronts which interfere in the fan-in plate must be carefully controlled to achieve a uniform interference pattern in each diffraction order. Any distortion of the wavefront results in structures of fringes in the output diffraction orders which reduce the coupling efficiency. This problem can be solved by using low aberration collimating lenses and output couplers and by minimizing the Fresnel reflections on each interface which may give Fabry-Perot systems and may change the phase profile of the beams which propagate in the open cavity. The second limit in the coupling efficiency is given by the polarization properties of the beams which interfere in the fan-in plate. The maximum coupling efficiency will be only achieved for identical incident polarization states. In our experiment the adjustment of the polarization states is achieved by using all fiber polarization controllers (fiber loops). The polarization state and the degree of polarization at the output of each laser depends on the

polarization of the pump beam and on the birefringence of the active fiber [4.7]. Consequently, an adjustment of the output polarization state can also be achieved by adjusting the polarization state of the pump beam. As an example, a linear polarization state of the pump beam which is aligned parallel to one of the eigenpolarizations of the fiber results in a nearly linear output polarization of the fiber laser. This dependence of the coupling efficiency on the mutual polarization yields power fluctuations when the birefringence of the fiber changes. Therefore, single polarization or polarizing fibers should be used for the realization of coupled lasers, if the fibers will be subjected to movement, as it is the case for a laser which would be embedded into an endoscope for surgical purposes. The mechanical adjustment of the fan-in plate in the laser is not so critical, since it is placed in the Fourier plane of the lens, where the divergence of the beams is low. Consequently, a mismatch in the position of the fan-in does only slightly change the coupling efficiency. The main effect will be a lower back-coupling efficiency into each fiber, which results in a lower output power of the coupled lasers because of the larger intracavity losses.

4.3.8.2 Evidence of the coherent addition

The principle of the coherent addition can be easily demonstrated by considering the experimental setup shown in Fig. 4.3.26. The three laser cavities are simultaneously pumped, but the output of one of the fiber lasers is blocked with a small mask placed at the output of the fiber.

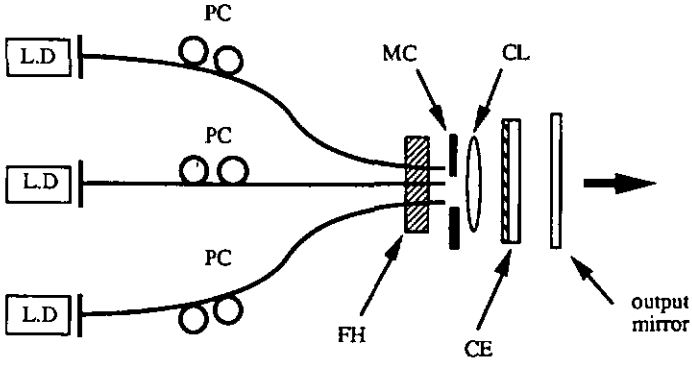

Fig. 4.3. 26. Setup for the demonstration of the coherent addition. MC is a mask which can be displaced to block one of the lateral cavities. The other elements are the same as explained in Fig. 4.2.4.

The distribution of the output power in the diffraction orders is shown in Fig. 4.3.27 under different coupling conditions. The graph on the left side shows the output power distribution when the left cavity is blocked. In this case the –1st diffraction order cannot be minimized, since it receives only light by diffraction from the central laser. The graph in the center shows the output power distribution when the right cavity is blocked. In this cases the +1st diffraction order cannot be minimized. The graph on the right side of the figure shows the distribution of the output power when all the three cavities are coupled, allowing the diffracoon orders +1st and –1st to be minimized for the maximum coupling efficiency in the zero diffraction order.

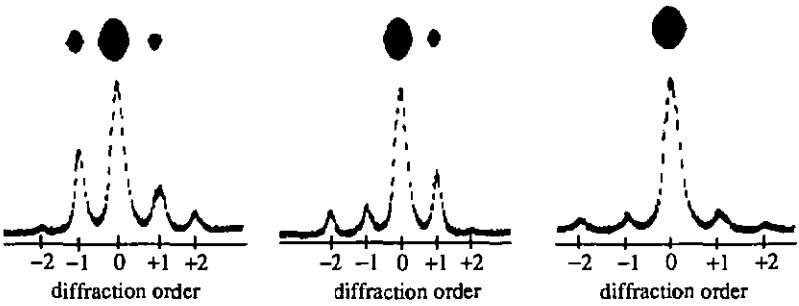

Fig. 4.3.27. Distribution of the output power in the diffraction orders: The left cavity is blocked (left), the right cavity is blocked (center), all three cavities are coupled (right).

4.3.9. Spectral properties of the coupled cavity fiber laser

The resonances of the coupled cavity laser are fixed by considering the conditions on the mutual phases which are necessary for the steady state, as given by Eq. (4.3.37), namely $\Phi_i = m_i \pi$. If we assume that the accumulated phases Φ_i are the propagation phases, namely

$$\Phi_i = \frac{2\pi}{\lambda} n L_i, \tag{4.3.93}$$

where n is the index of refraction of the fiber core and L_i is the fiber length of the i-th cavity. Eq. (4.3.37) can be written as

$$\frac{m_i}{L_i} = \frac{m_j}{L_j}, \forall\, i \neq j. \tag{4.3.94}$$

This equation fixes the resonances as a function of the mutual lengths L_i of the laser cavities. Nevertheless, this model cannot reasonably describe the full spectral properties of the coupled lasers. The main reason lies in the very large spectral width of the gain curve (FWHM typically larger than 50 nm) which allows a very large number of resonances to oscillate (typically more than 10^5 resonances). Complicated competition occurs between these resonances, mainly due to the mixed homogeneous and inhomogeneous broadening of the gain curve. The dynamic behavior of the laser spectrum which is necessary for the steady state makes a detailed analysis of the spectrum extremely difficult. For these reasons, the power spectrum has been analyzed by considering only the envelope of the resonances. Figure 4.3.28 shows the emission spectrum of a typical Nd^{3+}: SiO_2: GeO_2 doped fiber laser, which was obtained by blocking the two lateral cavities of the coupled lasers. The peak wavelength is $\lambda_s = 1088$ nm and the spectral width is about 5 nm. The spiky structure of the observed spectrum shown in Fig. 3.2.3 is given by the cavity mirrors, which act as Fabry Perot etalons. The power spectrum remains stable since no phase adjustments are required for the steady state of the central cavity alone.

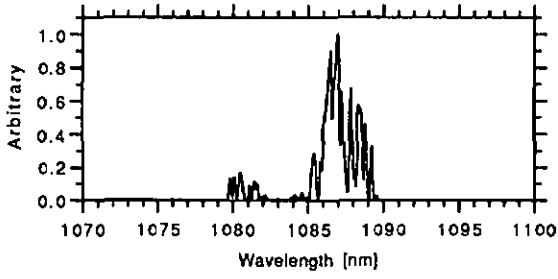

Fig. 4.3.28. Power spectrum when the two lateral cavities are blocked. The spectrum of a typical fiber laser can be observed. The peak wavelength is $\lambda_s = 1088$ nm.

The effect of the coherent coupling between the three individual emitters yields a shift of the emission spectrum towards shorter wavelengths, as seen in Fig. 4.3.29, where the peak wavelength is measured at $\lambda_s = 1078$ nm. This wavelength shift is explained by the dispersion of the fan-in. This can be understood by considering the coupling of the reflected beam in the three fibers, as shown in Fig. 4.3.30. The separation d between the collimated beams is fixed by the diffraction through the fan-in, namely

$$d = \alpha f = \frac{\lambda_s f}{\Lambda}, \qquad (4.3.95)$$

where α is the angle of diffraction, f is the focal length of the collimating lens and Λ is the period of the grating.

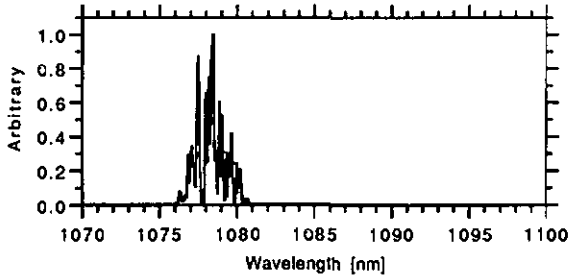

Fig. 4.3.29. Power spectrum of the couple cavity fiber lasers. The peak wavelength is shifted to λ_s = 1078 nm.

The dispersion of the grating yields a change of the diffraction angle α as a function of the wavelength λ_s. Consequently, the coupling efficiency in the lateral fibers strongly depends on the wavelength.

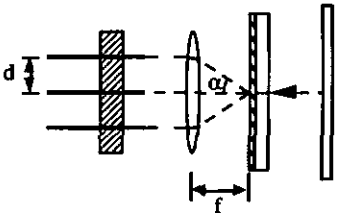

Fig. 4.3.30. Diffraction of the reflected beam on the fan-in and coupling in the three fibers.

The coupling in the central fiber does not depend on the wavelength, since it is achieved by the zero diffraction order of the fan-in. The fiber spacing d has been adapted for a wavelength of λ_s = 1088 nm, and for a period of the grating Λ = 50 µm. The focal length was f = 14.5 mm. This gives, by using Eq. (4.3.95), a separation d = 315.51 µm. In this case, the maximum coupling efficiency is achieved in the three fibers. Nevertheless, a small error $\Delta\Lambda$ in the period Λ of the grating results in a reduction of the coupling efficiency in the lateral fibers, due to the change of the spacing d. This forces the coupled lasers to oscillate at another wavelength which

allows to optimize the coupling. This effect explains the shift of the emission wavelength between the central cavity alone which oscillates at $\lambda_s = 1088$ nm (center of the gain curve) and the coupled cavity laser which emit at $\lambda_s = 1078$ nm. The error $\Delta\Lambda$ which is necessary to achieve a wavelength change of $\Delta\lambda_s$ is calculated by deriving Eq. (4.3.95). This yields

$$\Delta\lambda_s = \frac{d}{f}\Delta\Lambda. \tag{4.3.96}$$

A typical mean value for the error on the period of the grating is $\Delta\Lambda = 0.4$ μm. This gives, by using Eq. (4.3.96), a wavelength shift of $\Delta\lambda_s \approx 9$ nm. This value is in excellent agreement with the wavelength shift of $\Delta\lambda_s = 10$ nm which has been measured between the peak wavelengths in Figs. 4.3.28 and 4.3.29. The spectrum shows a dynamic behavior when one of the cavities is slightly perturbed, for example by heating the fiber. This is due to the adjustment of the emission frequency, which is necessary for the steady state of the coupled lasers, as required by Eq. (4.3.57). The frequency change has been demonstrated by analyzing the power spectrum of the coupled lasers with a plate of glass (shearing plate) placed in the output beam. The interferences between the beams which are reflected by the two interfaces of the plate yield fringes. The displacements of the fringes due to the frequency change are analyzed with a small aperture detector (diameter of 0.2 mm), as shown in Fig. 4.3.31. The thickness of the plate was of $l_p = 1$ mm, which gives a wavelength separation of $\Delta\lambda = 0.28$ nm between successive fringes.

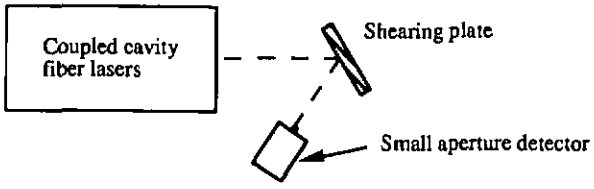

Fig. 4.3.31. Setup for the demonstration of the frequency changes in the coupled lasers. The displacement of the fringes is measured with a low aperture detector.

The intensity which was measured on the detector is shown in Fig. 4.3.32 when one of the laser cavity was slightly heated. The large modulation depth which can be seen in Fig. 4.3.32 indicates that the coherence length of the coupled lasers is larger than twice the optical thickness of the plate, namely $2nl_p \approx 3$ mm. This yields a maximum spectral width of $\Delta\lambda = 0.4$ nm, which is smaller than the FWHM spectral width of $\Delta\lambda = 2$ nm which can be seen in Fig. 4.3.30. This is explained by the fact that the spectrum of Fig. 4.3.29 has been integrated

with a long time constant (typically 10 minutes). Therefore, it represents a distribution of the output spectrum of the coupled lasers. Consequently, the instantaneous spectral width of the coupled lasers is much narrower (typical spectral width $\Delta\lambda < 0.4$ nm).

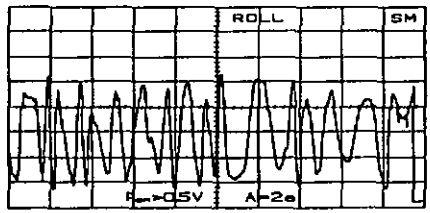

Fig. 4.3.32. Intensity detected on the small aperture detector. The modulation is given by the displacement of the fringes in front of the detector which is produced by the frequency change which is necessary for maintaining the steady state phase condition.

4.3.10. Transfer function of the coupled lasers

The formalism which has been developed for the modeling of the coupled cavity lasers allows to calculate the transfer function of this system. The transfer function gives an interesting description of the basic properties of the coupled resonators, such as the influence of the phase matching on the cavity losses.

4.3.10.1 Basic principle

The transfer function is analyzed by considering a probe signal which enters the coupled lasers through the output mirror. The reflected signal is calculated as a function of a common phase shift ψ applied on all laser cavities. This principle is schematically shown in Fig. 4.3.33.

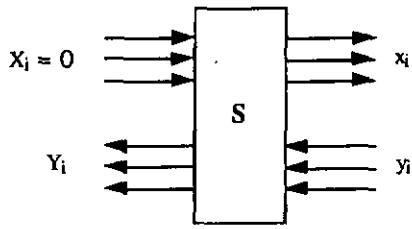

Fig. 4.3.33. Block diagram for the modeling of the transfer function of the coupled lasers.

The output vector $\vec{x}$ is calculated as a function of the input vector $\vec{y}$ for $X_i = 0$. The input and output vectors are connected through the matrix S of the coupled lasers given in Eq. (4.3.31). The system which is shown in Fig. 4.3.33 can be written as

$$\begin{pmatrix} x_1 \\ x_2 \\ x_3 \\ y_1 \\ y_2 \\ y_3 \end{pmatrix} = S \cdot \begin{pmatrix} 0 \\ 0 \\ 0 \\ Y_1 \\ Y_2 \\ Y_3 \end{pmatrix}. \qquad (4.3.97)$$

The output vector $\vec{x}$ can be easily written as a function of the vector $\vec{y}$ by considering the two 3 x 3 sub-matrices S_1 and S_2 of S, namely

$$S_1 = \begin{pmatrix} S_{14} & S_{15} & S_{16} \\ S_{24} & S_{25} & S_{26} \\ S_{34} & S_{35} & S_{36} \end{pmatrix} \qquad (4.3.98)$$

$$S_2 = \begin{pmatrix} S_{44} & S_{45} & S_{46} \\ S_{54} & S_{55} & S_{56} \\ S_{64} & S_{65} & S_{66} \end{pmatrix}. \qquad (4.3.99)$$

The vectors $\vec{y}$ and $\vec{x}$ can then be written as a function of the vector $\vec{Y}$

$$\vec{y} = S_2 \vec{Y} \qquad (4.3.100)$$

$$\vec{x} = S_1 \vec{Y}. \qquad (4.3.101)$$

Equations (4.3.100) and (4.3.101) ca be combined to give $\vec{x}$ as a function of $\vec{y}$, namely

$$\vec{x} = S_1 S_2^{-1} \vec{y} = K \vec{y}. \qquad (4.3.102)$$

The elements of matrix K are listed in Annex A.3. We are mainly interested in the transfer function of the zero diffraction order. This means that only the x_2 and y_2 components have to be considered. Consequently, Eq. (4.3.102) can be reduced to

$$x_2 = K_{22} y_2, \qquad (4.3.103)$$

where K_{22} is the corresponding matrix component of K. This element can be written as a function of the elements S_{ij} of the matrix S of the coupled lasers given in Sect. 4.3.2, namely

$$K_{22} = -\frac{1}{N}\,(S_{24}\,S_{45}\,S_{66} - S_{24}\,S_{46}\,S_{65} - S_{25}\,S_{44}\,S_{66} + S_{25}\,S_{46}\,S_{64} + S_{26}\,S_{44}\,S_{65} - S_{26}\,S_{45}\,S_{64}), \qquad (4.3.104)$$

where

$$N = S_{44}\,S_{55}\,S_{66} - S_{44}\,S_{56}\,S_{65} - S_{54}\,S_{45}\,S_{66} + S_{54}\,S_{46}\,S_{65} + S_{64}\,S_{45}\,S_{56} - S_{64}\,S_{46}\,S_{55}. \qquad (4.3.105)$$

4.3.10.2 Transfer function of the coupled lasers with transparent fibers

The analysis of the transfer function of the coupled lasers by considering transparent (losseless and gainless) fibers gives interesting information on the cavity losses which are produced by a phase mismatch between the individual emitters. Figure 4.3.34 shows the power transfer function and the phase of the reflection of the coupled lasers with $g_i = 1$, $R_1 = 99$ %, $R_2 = 95$ % and $\Phi_i = 0$. In this case the coupled lasers are identical to a single losseless Fabry-Perot resonator with two mirrors of reflectivities R_1 and R_2, respectively. This equivalence can be verified by comparing the minimum value of the reflected signal with the minimum reflection

$$R_{min} = 1 - \frac{T_1\,T_2}{(1 - \sqrt{R_1\,R_2})^2} \qquad (4.3.106)$$

of a single Fabry-Perot. The same value $R_{min} = 0.452$ is obtained with the two models.

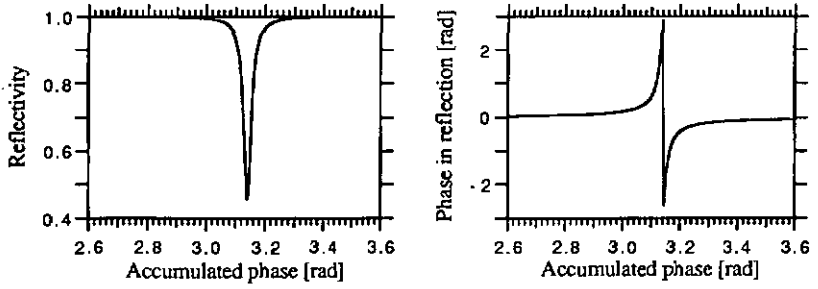

Fig. 4.3.34. Power and phase transfer function of the coupled fiber lasers with losseless fibers ($g_i = 1$). A minimum reflectivity of 0.452 is obtained at resonance which is exactly the minimum reflectivity of a single equivalent resonator with reflectivities R_1 and R_2.

The finesse of the coupled resonators decreases when the mutual phases between the emitters are not matched. Figure 4.3.35 shows the power transfer function for unmatched phases, namely $\Phi_1 = \pi/4$, $\Phi_2 = 0$, $\Phi_3 = \pi/4$.

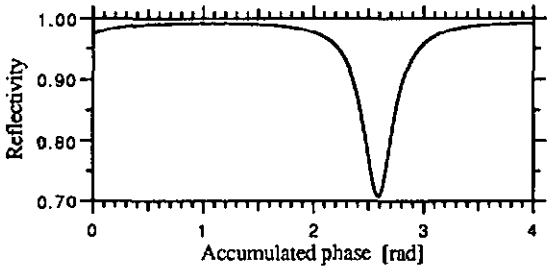

Fig. 4.3.35. Power tronsfer function of the coupled cavity fiber lasers for unmatched mutual phases, namely $\Phi_1 = \pi/4$, $\Phi_2 = 0$, $\Phi_3 = \pi/4$. The other parameters are the same than for Fig. 4.3.32.

This analysis of the transfer function allows to characterize the cavity losses due to a phase mismatch, but can also be extended to the analysis of the losses produced by an unmatched distribution of the incident optical power on the fan-in element. The effect of the intracavity losses can also be analyzed by considering an effective reflectivity R_{2eff} of the output mirror as defined in Eq. (4.3.80). This model is also the basis for an analysis of the detailed spectral properties of the coupled lasers, since it gives the information of the finesse of the resonances. This kind of analysis becomes of interest if the spectral properties of the coupled lasers are perfectly well controlled as it is the case for a single frequency fiber laser.

4.4. Conclusions

In this Chapter, the coherent addition of independent fiber lasers has been experimentally and theoretically demonstrated, for the first time to our knowledge, by using an intracavity fan-in element for the coupling. A typical coupling efficiency of 77 % has been obtained for three Nd^{3+} doped coupled fiber lasers. A dedicated linear theoretical model has been developed to analyze the basic properties of the coupled lasers, and to demonstrate the self adjustment of the mutual amplitudes and phases between the emitters, which are necessary for steady state

oscillation. This analysis was carried out by considering first the conditions for the laser threshold. The comparison with the eigensolutions of the open coupled resonators allowed to find the conditions for steady state oscillation. The analysis of the gain saturation showed that the coupling efficiency of the output power in the zero diffraction order was independent of the mutual pumping level in the individual lasers. This stability of the coupling efficiency has been experimentally confirmed. Theoretical and experimental investigations demonstrated the dynamic of the spectrum which is necessary for steady state oscillation. The effect of the dispersion of the fan-in on the spectrum has been theoretically and experimentally verified. The study of the transfer function of the coupled resonators has been carried out to demonstrate the effect of a phase mismatch on the cavity losses. The analysis of the transfer function is of a fundamental interest for a detailed analysis of the spectral properties of the coupled cavity laser.

The power properties of the coupled lasers have been theoretically analyzed by considering a approximate model for the output power of the individual emitters. This model was developed by adapting to a guided system the so called "Rigrod analysis" [4.8], which allows to calculate the power properties of bulk lasers with large output coupling. This model showed a very good agreement with the experimental results. This model demonstrates that the design of the active fiber is fundamental for an efficient laser. Optimum numerical aperture and fiber core radius have to be carefully chosen to achieve simultaneously the highest efficiency and an effective guiding of the laser light in the fibers [2.4]. Nevertheless, this simple model does not consider the saturation of the pump and the ground state depletion, which arise for high pumping levels.

Further improvements of these models would be to include the effects of the ground state depletion and of the pump saturation for a better description of very high power coupled cavity fiber lasers. A detailed analysis of the power spectrum of the coupled lasers could be performed by considering the spectral selectivity of the coupled resonators, which can be modeled by use of the transfer function of the coupled lasers. The interaction between the coupled resonators and the mixed homogeneously and inhomogeneously broadened gain medium could be then investigated for a better understanding of the spectrum.

The theoretical models which have been developed can be straightforwardly extended to any larger number N of resonators by using 2N x 2N matrices for the description of the cavity elements. The conditions for steady-state oscillation and for the laser threshold will have the same structure as discussed in Sect. 4.3, for N = 3. This model can also be easily adapted to the analysis of coupled lasers with different input mirrors. Nevertheless this yields more complicated expressions for the steady state and for the threshold, which do not bring significantly new information.

The described intracavity coupling technique is well adapted to realize high power fiber lasers and for distributed active fiber sensors. Nevertheless, the main difficulty for the fabrication of an efficient high power coupled cavity fiber laser lies in the intracavity losses which result of the open cavity configuration. Typical single pass losses $\rho = 63$ % have been measured in our experimental system, which limit strongly the efficiency of the coupled lasers. This high single pass loss requires very high transmission (typically more than 90 %) of the output mirror to compensate for the best efficiency. The intracavity loss ρ can be efficiently minimized by a careful design of the open cavity. The Fresnel reflections can be strongly reduced by use of efficient anti-reflection coatings on each interface. The use of microoptics and of dedicated diffractive optical elements can be a good approach for the fabrication of a compact and stable coupled cavity fiber laser. A basic structure of a fiber laser bundle is shown in the figure below. This configuration could be of strong interest for medical applications, by embedding a fiber laser bundle into an endoscope. The use of multicore active fibers could be very attractive for this application.

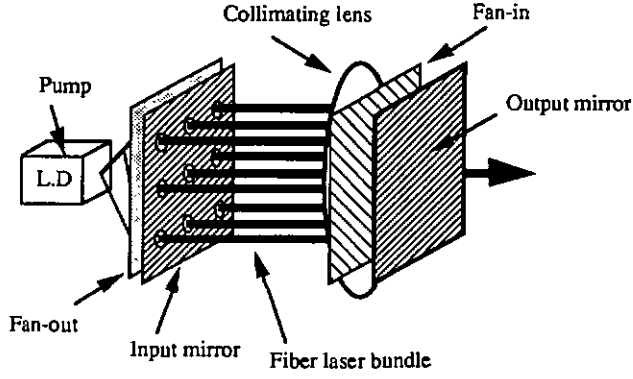

The analysis of the optical frequency change in the coupled lasers, when an external perturbation is applied, is an interesting approach for new active distributed fiber sensors, as it has been demonstrated for a single fiber laser sensor [4.9]. Nevertheless, single frequency individual emitters should be considered to avoid the complex mode competition which complicates the signal processing. This could be easily achieved by using selective Bragg gratings, which can be directly engraved into the fiber core of each emitter by U.V. lithography [4.10].

5. References

Introduction.

[I] C. J. Koester et al., "Amplification in a fiber laser", Appl. Opt., 3, 1182-1186, (1964).

Chapter 1.

[1.1] G.S. Ofelt, "Intensities of crystal spectra of rare-earth ions", J. of Chem. Phys., 37, 511-520, (1962).

[1.2] W. F. Krupke, "Induced-emission cross section in neodymium laser glasses", J. Quantum. El., QE10, 450-457, (1974).

[1.3] W. L. Barnes et al., "detailed characterization of Nd-doped SiO_2: GeO_2 glass fiber lasers", Opt. Commun., 82, 282-288, (1991).

[1.4] C. R. Giles and E. Desurvire, "Modeling erbium-doped fiber amplifiers", J. Lightwave Technol., 9, pp. 271-283 (1991).

[1.5] B. Dussardier et al., "Simultaneous measurements of lifetime, gain and emission cross section in a neodymium doped fiber", Photonics Technol. Lett., 4, 419-421, (1993).

[1.6] R. Wyatt, "Spectroscopy of rare-earth doped fibres", *Optical fibre lasers and amplifiers*, pp. 79-105, P. W. France, (Blackie, 1991).

[1.7] J. C. Wright, "Up-conversion and excited state energy transfer in rare-earth doped materials", Topics in Applied Physics, 15, 239-295 (1976).

[1.8] Kazuo Arai et al., "Aluminum or phosphorus co-doping effects on the fluorescence and structural properties of neodymium-doped silica glass", J. Appl. Phys., 59, 3430-3436, (1986).

[1.9] J. C. Wright, "Up-conversion and excited state energy transfer in rare-earth doped materials", Topics in Applied Physics, 15, 239-295, (1976).

[1.10] D.F. Eaton, "Recommended methods for fluorescence decay analysis", Pure & Appl. Chem., 62, 1631-1648, (1990).

[1.11] Th. Weber, et al."Cladding-pumped fiber laser"; submitted for publication.

[1.12] H. Po, E. Snitzer et al., "Double clad high brightness Nd fiber laser pumped by GaAlAs phased array", OFC conference, paper PD7, (1989).

[1.13] R. Ulrich et al., "Beam to fiber coupling with low standing wave ratio", Appl. Opt., 19, 2453-2456, (1980).

Chapter 2

[2.1] A. W. Snyder, J. D. Love, *Optical waveguide theory*, (Chapman and Hall, NY, 1983), p. 301-335.

[2.2] M. F. Digonnet, C. J. Gaeta, "Theoretical analysis of optical fiber laser amplifiers and oscillators", Appl. Opt. 24, 333-342, (1985).

[2.3] M. F. Digonnet, "Theory of superfluorescent fiber laser", J. Lightwave Technol., LT-4, 1631-1639, (1986).

[2.4] M. F. Digonnet, "Closed-form expressions for the gain in three and four level laser fibers", J. Quantum El., 26, 1788-1796, (1990).

[2.5] J. R. Armitage, "Three-level fiber laser amplifier: a theoretical model". Appl. Opt., 27, 4831-4836, (1988).

[2.6] M. F. Digonnet, "Theory of operation of three and four level fiber amplifiers and sources", SPIE Proc. 1702, *Fiber Laser Sources and Amplifiers*, 8-25, (1989).

[2.7] E. Desurvire et al., "Characterization and modeling of amplified spontaneous emission in unsaturated Erbium-doped fiber amplifiers", Photonics Technol. Lett., 3, 127-129, (1991).

[2.8] M. F. Digonnet, "Characterization and optimization of the gain in Nd doped single-mode fibers", J. Quantum. El., 26, 1105-1110, (1990).

[2.9] W. A. Clarkson et al., "Effects of transverse-mode profile on slope efficiency and relaxations in a longitudinally-pumped laser", J. of Mod. Optics, 36, 483-498, (1989).

Chapter 3

[3.1] H. K. Kim et al., "Polarimetric fiber laser sensors", Opt. Lett., 18, 317-319, (1993).

[3.2] P. R. Morkel, "Erbium-doped fiber superfluorescent source for the fiber gyroscope", *Springer Proc. Phys.*, OFS 89 (Paris), 44, 143-148, (1989).

[3.3] K. Ivatsuki, "Excess noise reduction in fiber gyroscope using broader spectrum linewidth Er -doped superfluorescent fiber laser", Photonics Technol. Lett., 3, 281-283, (1991).

[3.4] K. T. Grattan, A. W. Palmer, Y. N. Ning, "The use of low coherence light sources in fiber-optic interferometric systems", in Sensors vol. 6, eds. W. Göpel, J. Hesse, J. N. Zemel, (VCH Weinheim, 1992), p. 530-549.

[3.5] P. R. Morkel, "Wavelength stability of Nd^{3+} doped fiber fluorescent source", Electron. Lett., 26, 873-875, (1990).

[3.6] M. F. Digonnet, K. Liu, "Analysis of a 1060 nm Nd:SiO_2 Superfluorescent fiber laser", J. Lightwave Technol., 7, 1009-1015, (1989).

[3.7] I. M. Jauncey et al., "Efficient diode-pumped CW and Q-switched single-mode fibre laser", Electron. Lett., **22**, 198-199, (1986).

[3.8] J. Morel et al., "Fabrication and characterization of a Nd^{3+} doped monomode fiber laser", Helv. Phys. Acta., **63**, 813-814, (1990).

[3.9] B. S. Kawasaki, K. O. Hill et al., "Narrow-band Bragg reflectors in optical fibers", Opt. Lett., **3**, 66-68, (1978).

[3.10] L. Reekie et al., "Tunable single-mode fiber laser", J. Lightwave Technol., **LT-4**, 956-960, (1986).

[3.11] J. Morel et al., "Coherent coupling of an array of Nd^{3+}-doped single-mode fiber lasers by use of an intracavity phase grating", Opt. Lett., **18**, 1520-1522, (1993).

Chapter 4.

[4.1] P. Ehbets et al., "Beam shaping of high power laser diode arrays by continuous surface-relief elements", J. Mod. Opt., **40**, 637-645, (1993).

[4.2] H. P. Herzig et al., "Design and fabrication of highly efficient fan-out elements", Jpn. J. Appl. Phys. **27**, L1307-L1309 (1990).

[4.3] A. Yariv, *Optical Electronics*, third edition, (Holt Saunders, 1985), p. 188-196.

[4.4] W. A. Clarkson et al., "Effects of transverse-mode profile on slope efficiency and relaxation oscillations in a longitudinally-pumped laser", J. Mod. Opt., **36**, 483-498, (1989).

[4.5] Ken' ichi Kubodera et al., "Single-transverse-mode Li Nd P_4 O_{12} slab waveguide laser", J. Appl. Phys., **50**, 653-659, (1979).

[4.6] D. C. Hanna et al., "Measurement of fibre laser losses via relaxation oscillations", Opt. Comm., **68**, 128-132, (1988).

[4.7] J. T. Lin, P. R. Morkel et al., "Polarization effects in fibre lasers", ECOC Technical digest I, 109-111, (1987).

[4.8] A. E. Siegman, *Lasers*, (University Science Books, 1986).

[4.9] H. K. Kim et al., "Polarimetric fiber laser sensor", Optics Lett., **18**, 317-319 (1993).

[4.10] K. O. Hill et al., "Photosensitivity in optical fibers", Annu. Rev. Mater. Sci., **23**, 125-157, (1993).

Annex A.1

Components of the matrix S of the coupled lasers (See Sect. 4.3.2.5)

$S_{11} = 0$

$$S_{12} = -\frac{t_2}{t_1}(t_1^2 + r_1^2)\, m_{12}\, g_2 \exp i\phi_2$$

$$S_{13} = -\frac{t_2}{t_1}(t_1^2 + r_1^2)\, m_{13}\, g_3 \exp i\phi_3$$

$S_{14} = 0$

$$S_{15} = \frac{m_{12}\, t_2\, r_1\, g_2}{t_1} \exp\, i\phi_2$$

$$S_{16} = \frac{m_{13}\, t_2\, r_1\, g_3}{t_1} \exp\, i\phi_3$$

$$S_{21} = -\frac{1}{g_1 t_1 t_2}\,(g_1^2\, m_{21}\,[t_1^2 t_2^2 + t_2^2\, r_1^2 + r_2^2\, t_1^2 + r_2^2\, r_1^2] \exp i\phi_1 - r_1\, r_2\, m_{54} - i\ \phi_1)$$

$$S_{22} = -\frac{1}{g_2 t_1 t_2}\,(g_2^2\, m_{22}\,[t_1^2 t_2^2 + t_2^2\, r_1^2 + r_2^2\, t_1^2 + r_2^2\, r_1^2] \exp i\phi_2 - r_1\, r_2\, m_{55} - i\ \phi_2)$$

$$S_{23} = -\frac{1}{g_3 t_1 t_2}\,(g_3^2\, m_{23}\,[t_1^2 t_2^2 + t_2^2\, r_1^2 + r_2^2\, t_1^2 + r_2^2\, r_1^2] \exp i\phi_3 - r_1\, r_2\, m_{56} - i\ \phi_3)$$

$$S_{24} = \frac{m_{21}\, r_1\, g_1}{t_1\, t_2}(t_2^2 + r_2^2) \exp\, i\phi_1 - \frac{m_{54}\, r_2}{g_1\, t_1\, t_2} \exp\, -i\phi_1,$$

$$S_{25} = \frac{m_{22}\, r_1\, g_2}{t_1\, t_2}(t_2^2 + r_2^2) \exp\, i\phi_2 - \frac{m_{55}\, r_2}{g_2\, t_1\, t_2} \exp\, -i\phi_2$$

$$S_{26} = \frac{m_{23}\, r_1\, g_3}{t_1\, t_2}(t_2^2 + r_2^2) \exp\, i\phi_3 - \frac{m_{56}\, r_2}{g_3\, t_1\, t_2} \exp\, -i\phi_3$$

$$S_{31} = -\frac{t_2}{t_1}(t_1^2 + r_1^2)\, m_{31}\, g_1 \exp i\phi_1$$

$$S_{32} = -\frac{t_2}{t_1}(t_1^2 + r_1^2)\, m_{32}\, g_2 \exp i\phi_2$$

$S_{33} = 0$

$$S_{34} = \frac{m_{31}\, t_2\, r_1\, g_1}{t_1} \exp\, i\phi_1$$

$$S_{35} = \frac{m_{32}\, t_2\, r_1\, g_2}{t_1} \exp\, i\phi_2$$

$$S_{36} = 0$$

$$S_{41} = \frac{r_1}{t_1 t_2 g_1 m_{44}} \exp -i\phi_1$$

$$S_{42} = \frac{r_1}{t_1 t_2 g_2 m_{45}} \exp -i\phi_2$$

$$S_{43} = \frac{r_1}{t_1 t_2 g_3 m_{46}} \exp -i\phi_3$$

$$S_{44} = -\frac{m_{44}}{g_1\, t_1\, t_2} \exp\ -i\phi_1$$

$$S_{45} = -\frac{m_{45}}{g_2\, t_1\, t_2} \exp\ -i\phi_2$$

$$S_{46} = -\frac{m_{46}}{g_3\, t_1\, t_2} \exp\ -i\phi_3$$

$$S_{51} = -\frac{1}{g_1 t_1 t_2}\ (g_1^2\, m_{21}\, r_2\, [t_1^2 + r_1^2] \exp i\phi_1 - m_{54}\, r_1 \exp -i\phi_1)$$

$$S_{52} = -\frac{1}{g_2 t_1 t_2}\ (g_2^2\, m_{22}\, r_2\, [t_1^2 + r_1^2] \exp i\phi_2 - m_{55}\, r_1 \exp -i\phi_2)$$

$$S_{53} = -\frac{1}{g_3 t_1 t_2}\ (g_3^2\, m_{23}\, r_2\, [t_1^2 + r_1^2] \exp i\phi_3 - m_{56}\, r_1 \exp -i\phi_3)$$

$$S_{54} = \frac{m_{21}\, r_1\, r_2\, g_1}{t_1\, t_2} \exp\ i\phi_1 - \frac{m_{54}}{g_1\, t_1\, t_2} \exp\ -i\phi_1$$

$$S_{55} = \frac{m_{22}\, r_1\, r_2\, g_2}{t_1\, t_2} \exp\ i\phi_2 - \frac{m_{55}}{g_2\, t_1\, t_2} \exp\ -i\phi_2$$

$$S_{56} = \frac{m_{23}\, r_1\, r_2\, g_3}{t_1\, t_2} \exp\ i\phi_3 - \frac{m_{56}}{g_3\, t_1\, t_2} \exp\ -i\phi_3$$

$$S_{61} = \frac{r_1}{t_1 t_2 g_1\, m_{64}} \exp -i\phi_1$$

$$S_{62} = \frac{r_1}{t_1 t_2 g_2\, m_{65}} \exp -i\phi_2$$

$$S_{63} = \frac{r_1}{t_1 t_2 g_3\, m_{66}} \exp -i\phi_3$$

$$S_{64} = -\frac{m_{64}}{g_1\, t_1\, t_2} \exp\ -i\phi_1$$

$$S_{65} = -\frac{m_{65}}{g_2\, t_1\, t_2} \exp\ -i\phi_2$$

$$S_{66} = -\frac{m_{66}}{g_3\, t_1\, t_2} \exp\ -i\phi_3.$$

Annex A.2

Components of the matrix D of the open cavity fiber laser (See Sect. 4.3.4.1)

$d_{11} = 0$

$d_{12} = i\, t_2\, m_{12}\, g_2 \exp i\, \Phi_2$

$d_{13} = i\, t_2\, m_{13}\, g_3 \exp i\, \Phi_3$

$d_{14} = 0$

$d_{15} = 0$

$d_{16} = 0$

$d_{21} = \frac{g_1\, m_{21}}{t_2}\,(t_2^2 + r_2^2) \exp i\, \phi_1$

$d_{22} = \frac{g_2\, m_{22}}{t_2}\,(t_2^2 + r_2^2) \exp i\, \phi_2$

$d_{23} = \frac{g_3\, m_{23}}{t_2}\,(t_2^2 + r_2^2) \exp i\, \phi_3$

$d_{24} = -i\frac{r_2\, m_{54}}{t_2\, g_1} \exp -i\, \phi_1$

$d_{25} = -i\frac{r_2\, m_{55}}{t_2\, g_2} \exp -i\, \phi_2$

$d_{26} = -i\frac{r_2\, m_{56}}{t_2\, g_3} \exp -i\, \phi_3$

$d_{31} = i\, t_2\, m_{31}\, g_1 \exp i\, \Phi_1$

$d_{32} = i\, t_2\, m_{32}\, g_2 \exp i\, \Phi_2$

$d_{33} = 0$

$d_{34} = 0$

$d_{35} = 0$

$d_{36} = 0$

$d_{41} = 0$

$d_{42} = 0$

$d_{43} = 0$

$d_{44} = -i\frac{m_{44}}{g_1\, t_2} \exp -i\, \phi_1$

$d_{45} = -i\frac{m_{45}}{g_2\, t_2} \exp -i\, \phi_2$

$d_{46} = -i\frac{m_{46}}{g_2\, t_2} \exp -i\, \phi_3$

$d_{51} = i\frac{m_{21}\, r_2\, g_1}{t_2} \exp\, i\, \phi_1$

$d_{52} = i\frac{m_{22}\, r_2\, g_2}{t_2} \exp\, i\, \phi_2$

$d_{53} = i\frac{m_{23}\, r_2\, g_3}{t_2} \exp\, i\, \phi_3$

$d_{54} = -i\frac{m_{54}}{g_1\, t_2} \exp -i\, \phi_1$

$d_{55} = -i\frac{m_{55}}{g_2\, t_2} \exp -i\, \phi_2$

$d_{56} = -i\frac{m_{56}}{g_3\, t_2} \exp -i\, \phi_3$

$d_{61} = 0$

$d_{62} = 0$

$d_{63} = 0$

$d_{64} = -i\frac{m_{64}}{g_1\, t_2} \exp -i\, \phi_1$

$d_{65} = -i\frac{m_{65}}{g_2\, t_2} \exp -i\, \phi_2$

$d_{66} = -i\frac{m_{66}}{g_3\, t_2} \exp -i\, \phi_3.$

Annex A.3

Components of the matrix K of the transfer function (See Sect. 4.3.10.1)

$$N = S_{44}\,S_{55}\,S_{66} - S_{44}\,S_{56}\,S_{65} - S_{54}\,S_{45}\,S_{66} + S_{54}\,S_{46}\,S_{65} + S_{64}\,S_{45}\,S_{56} - S_{64}\,S_{46}\,S_{55}$$

$$K_{11} = -\frac{1}{N}\,(-S_{14}\,S_{55}\,S_{66} + S_{14}\,S_{56}\,S_{65} + S_{15}\,S_{54}\,S_{66} - S_{15}\,S_{56}\,S_{64} - S_{16}\,S_{54}\,S_{65} + S_{16}\,S_{55}\,S_{64})$$

$$K_{12} = -\frac{1}{N}\,(S_{14}\,S_{45}\,S_{66} - S_{14}\,S_{46}\,S_{65} - S_{15}\,S_{44}\,S_{66} + S_{15}\,S_{46}\,S_{64} + S_{16}\,S_{44}\,S_{65} - S_{16}\,S_{45}\,S_{64})$$

$$K_{13} = \frac{1}{N}\,(S_{14}\,S_{45}\,S_{56} - S_{14}\,S_{46}\,S_{55} - S_{15}\,S_{44}\,S_{56} + S_{15}\,S_{46}\,S_{54} + S_{16}\,S_{44}\,S_{55} - S_{16}\,S_{45}\,S_{54})$$

$$K_{21} = -\frac{1}{N}\,(-S_{24}\,S_{55}\,S_{66} + S_{24}\,S_{56}\,S_{65} + S_{25}\,S_{54}\,S_{66} - S_{25}\,S_{56}\,S_{64} - S_{26}\,S_{54}\,S_{65} + S_{26}\,S_{55}\,S_{64})$$

$$K_{22} = -\frac{1}{N}\,(S_{24}\,S_{45}\,S_{66} - S_{24}\,S_{46}\,S_{65} - S_{25}\,S_{44}\,S_{66} + S_{25}\,S_{46}\,S_{64} + S_{26}\,S_{44}\,S_{65} - S_{26}\,S_{45}\,S_{64})$$

$$K_{23} = \frac{1}{N}\,(S_{24}\,S_{45}\,S_{56} - S_{24}\,S_{46}\,S_{55} - S_{25}\,S_{44}\,S_{56} + S_{25}\,S_{46}\,S_{54} + S_{26}\,S_{44}\,S_{55} - S_{26}\,S_{45}\,S_{54})$$

$$K_{31} = -\frac{1}{N}\,(-S_{34}\,S_{55}\,S_{66} + S_{34}\,S_{56}\,S_{65} + S_{35}\,S_{54}\,S_{66} - S_{35}\,S_{56}\,S_{64} - S_{36}\,S_{54}\,S_{65} + S_{36}\,S_{55}\,S_{64})$$

$$K_{32} = -\frac{1}{N}\,(S_{34}\,S_{45}\,S_{66} - S_{34}\,S_{46}\,S_{65} - S_{35}\,S_{44}\,S_{66} + S_{35}\,S_{46}\,S_{64} + S_{36}\,S_{44}\,S_{65} - S_{36}\,S_{45}\,S_{64})$$

$$K_{33} = \frac{1}{N}\,(S_{34}\,S_{45}\,S_{56} - S_{34}\,S_{46}\,S_{55} - S_{35}\,S_{44}\,S_{56} + S_{35}\,S_{46}\,S_{54} + S_{36}\,S_{44}\,S_{55} - S_{36}\,S_{45}\,S_{54}).$$

Acknowledgments

I want to thank first my remarkable Parents for the privilege they offered me to carry out my studies and for their support of all the days without which nothing would have been possible.

I wish to express all my gratitude to the director of my thesis, Prof. R. Dändliker, for the invaluable help and for the confidence he always gave me during the six years I had the privilege to pass in his group. I want to thank him for all the priceless discussions and for the clever reviewing of this thesis.

My special thanks go to Prof. W. Lüthy for the fruitful collaboration we have developed in the frame of the projects which gave the basis for this work.

I want to thank the members of the jury, Prof. W. Lüthy, Prof. R. P. Salathé and Prof. F. Pellandini for their critical reviewing of my thesis.

I am also indebted to Drs. G. Kotrotsios, V. Neuman and H. Berthou (CSEM) for their invaluable work which resulted in the fabrication of efficient rare earth doped fibers. I also thank these persons for the friendly and efficient collaboration we have shared during these six years.

I want to thank all my colleagues for the help they gave me and for the pleasant atmosphere they brought at the IMT, which is so important for an efficient work. My special thanks go to E. Zimmermann and A. Woodtli who collaborated to the projects on active fibers, and to P. Ehbets and H.P. Herzig for the design of the fan-in element and for many fruitful discussions.

I would like to thank all the technicians of the mechanical and electronical workshops. Special thanks go to Marcel Groccia for his precious help in solving many problems in electronics. I am also grateful to all the secretarial staff for their kindness and for the efficient hard work they have always accomplished for me.

This work was partially supported by the "Fondation Suisse pour la Recherche en Microtechnique" (FSRM 88/15), and by the Swiss priority program "Optique".